MICROCOPY RESOLUTION TEST CHART
NATIONAL BUREAU OF STANDARDS-1963-A

RADC-TR-77-296
Final Technical Report
August 1977

MICROSTRIP REFLECTARRAY ANTENNA PROGRAM

Texas Instruments Incorporated
13500 North Central Expressway
Dallas, Texas 75222

August 1977

Final Report for Period 14 April 1976 to 14 April 1977

ROME AIR DEVELOPMENT CENTER ✓
AIR FORCE SYSTEMS COMMAND
GRIFFISS AIR FORCE BASE, NEW YORK 13441

DDC

JAN 5 1978

Title of Report: Microstrip Reflectarray Antenna Program

This Technical Report has been reviewed and approved for publication.

APPROVED:

Walter Rotman

WALTER ROTMAN, Chief
Antennas and RF Components Branch
Electromagnetic Sciences Division

APPROVED:

Allan C. Schell

ALLAN C. SCHELL, Acting Chief
Electromagnetic Sciences Division

FOR THE COMMANDER: *John P. Huss*

Plans Office

REPORT DOCUMENTATION PAGE	READ INSTRUCTIONS BEFORE COMPLETING FORM

1. REPORT NUMBER	2. GOVT ACCESSION NO.	3. RECIPIENT'S CATALOG NUMBER
RADC-TR-77-296	Final rept. 14 Apr 76 — 14 Apr 77	

4. TITLE (and Subtitle)	5. TYPE OF REPORT & PERIOD COVERED
MICROSTRIP REFLECTARRAY ANTENNA PROGRAM	Final Report 4/14/76 to 4/14/77
	6. PERFORMING ORG. REPORT NUMBER
	U1-726210-F

7. AUTHOR(s)	8. CONTRACT OR GRANT NUMBER(s)
Frank Opp James P. Montgomery	F30602-76-C-0226

9. PERFORMING ORGANIZATION NAME AND ADDRESS	10. PROGRAM ELEMENT, PROJECT, TASK AREA & WORK UNIT NUMBERS
Texas Instruments Incorporated 13500 North Central Expressway Dallas, Texas 75222	62702F 46001431

11. CONTROLLING OFFICE NAME AND ADDRESS	12. REPORT DATE
Deputy for Electronic Technology (RADC) Hanscom AFB, Massachusetts 01773 Monitor/H. Ehrenspeck/EEA	August 1977
	13. NUMBER OF PAGES
	72

14. MONITORING AGENCY NAME & ADDRESS(if different from Controlling Office)	15. SECURITY CLASS. (of this report)
76p.	UNCLASSIFIED
	15a. DECLASSIFICATION/DOWNGRADING SCHEDULE

16. DISTRIBUTION STATEMENT (of this Report)

Approved for public release; distribution unlimited

17. DISTRIBUTION STATEMENT (of the abstract entered in Block 20, if different from Report)

18. SUPPLEMENTARY NOTES

19. KEY WORDS (Continue on reverse side if necessary and identify by block number)

Microwave	Reflectarray
Microstrip	Phased Array
Antenna	Microwave Integrated Circuits

20. ABSTRACT (Continue on reverse side if necessary and identify by block number)

Results of a study to determine the feasibility and design limitations of a microstrip reflectarray antenna are presented. This antenna, which has been proposed as a means to provide potential low-cost corporate-fed phased arrays, utilizes microwave integrated circuit techniques to integrate the radiating element, phase-shifter components, dc distribution, and logic circuitry into a single structure. The report contains design and performance data on such an element operating at 3 GHz. The performance was measured using a waveguide test fixture to simulate the array. Fundamental element performance is in agreement with the results of supporting analysis.

DD FORM 1473 EDITION OF 1 NOV 65 IS OBSOLETE
1 JAN 73

347 650.

20.   ABSTRACT (Continued)

    The usefulness of the element in an array is severely restricted by very narrow bandwidths and relatively high losses. However, supporting theoretical analysis showed the element's loss and operating bandwidth are a strong function of the element spacing in an array environment. Results indicate reduced loss and increased bandwidth with decreased spacing, thereby suggesting that the present performance deficiencies could be overcome.

EVALUATION REPORT

This report is the Final Report of Contract No. F30602-76-C-0226. It covers first, a study of a microstrip antenna element and second, describes the development of a microstrip reflectarray with microstrip elements used throughout the array.

In the first part of the report the influence of various parameters on the bandwidth characteristics of the microstrip element, such as dielectric constant of the substrate, shape and dimensions of the metal disk, and its height above the groundplane are discussed.

In the second part of the report several microstrip reflectarrays are described with diode switches integrated into the array elements. The fabrication techniques developed for these arrays represent a simple, potentially low-cost approach to other similar applications.

In addition, an analysis of the scattering by an infinite array of microstrip disks has been made. This analysis is used to get insight into the operation of a reflectarray with diodes integrated into the elements to achieve phaseshift for circular polarized fields.

Hermann Ehrenspeck

HERMANN EHRENSPECK
Contract Monitor
Antennas and RF Components Branch
Electromagnetic Sciences Division

ACCESSION for

NTIS	White Section	X
BDC	Buff Section	☐
UNANNOUNCED		☐
JUSTIFICATION		

BY
DISTRIBUTION/AVAILABILITY CODES

| Dist. | AVAIL. and/or SPECIAL |
| A | |

TABLE OF CONTENTS

LIST OF ILLUSTRATIONS

SECTION I

INTRODUCTION

This document is the final report for the Microstrip Reflectarray Antenna Program, Contract Number F30602-76-C-0226. The work was initially under the direction of Mr. Carman Malagisi, Rome Air Development Center (RADC), Griffiss Air Force Base, New York. Later, the monitorship was transferred to Mr. Hermann Ehrenspeck, RADC, Hanscom Air Force Base, Massachusetts.

There has been a constant need to reduce the cost of phased arrays for tactical radars and communication systems. The bulk of the cost and RF losses in phased arrays are in transmission lines and phase shifters. The use of reflectarrays is one method of reducing the costs of transmission lines. However, the phase shifters on each element still remain costly. If the phase shifters could be incorporated into the element to reduce the overall costs in reflectarray mode, then reflectarrays could become a more competitive antenna system where phased array performance is required.

The microstrip antenna as described by R.E. Munson and J.Q. Howell is a means of providing low-cost corporate-fed phased arrays. The problems of phase shifters still exist. Mr. C. Malagisi of RADC utilized the technology described by Munson and Howell and applied it to a microstrip reflectarray technique.

The purpose of this program was to determine the feasibility and design limitation of such an antenna element; that is, a microstrip reflectarray antenna where microwave integrated circuit techniques are used to integrate the radiating element, phase shifters, dc distribution and logic circuitry into a single structure

The approach to this study is indicated by the program's major milestones (Figure 1). The initial program phase consisted of studies to better understand element operation and the method of test. The second phase consisted of the design and evaluation of a 3 GHz reflectarray element with 3-bit phase shifter capability. This effort was paralleled with an original investigation into the microstrip element fundamental theory of operation. The third phase consisted of a short effort to evaluate element performance near 15 GHz.

The primary objective of this program is to verify the element operation as envisioned by Mr. Malagisi. That is, if diodes are placed along a circumference of the disk at an arbitrary distance from its center and biased accordingly to cause short or open circuit, the element will reradiate a circular polarized signal with the same sense but shifted in phase equal to twice the angular spacing of the short locations. Other results are that a 3-bit reflection phase shifter can be realized with only eight diodes.

The usefulness of the element in an array is severely restricted by very narrow bandwidths and relatively high loss.

However, the supporting theoretical analysis showed the element's loss and operating bandwidth are a strong function of the element spacing in an array environment. The results indicate reduced loss and increased bandwidth with decreased spacing, thereby suggesting that the present performance deficiencies could be overcome.

1
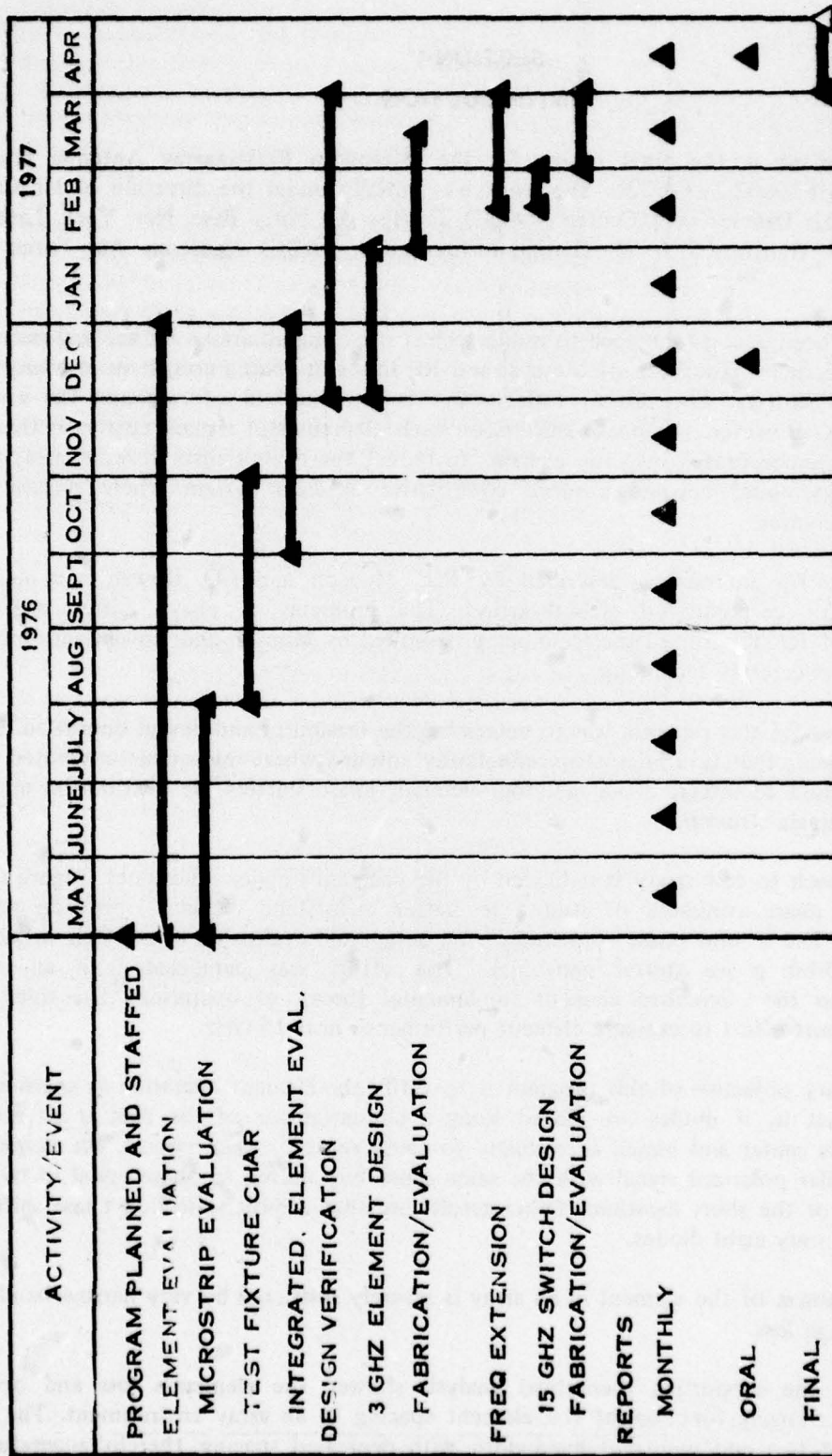
Figure 1. Program Major Milestones

ACTIVITY/EVENT	1976								1977			
	MAY	JUNE	JULY	AUG	SEPT	OCT	NOV	DEC	JAN	FEB	MAR	APR
PROGRAM PLANNED AND STAFFED												
ELEMENT EVALUATION												
MICROSTRIP EVALUATION												
TEST FIXTURE CHAR												
INTEGRATED, ELEMENT EVAL.												
DESIGN VERIFICATION												
3 GHZ ELEMENT DESIGN												
FABRICATION/EVALUATION												
FREQ EXTENSION												
15 GHZ SWITCH DESIGN												
FABRICATION/EVALUATION												
REPORTS												
MONTHLY												
ORAL												
FINAL												

208914

SECTION II
REFLECTARRAY DESCRIPTION AND ANALYSIS

A. INTRODUCTION

In many applications, microstrip antennas are an attractive alternative to more conventional radiators. Microstrip antennas exhibit a low profile, can easily conform to planar, cylindrical and conical surfaces, and are small in size and weight. These elements are generally etched on copper clad dielectric material. As a consequence, production cost is low while good mechanical tolerances are maintained.

Two recent papers by Howell[1] and Munson[2] have been directed to the design of these elements. Both papers discuss the resonant properties of the microstrip elements and give experimental results.

Recently, Phelan[3,4,5] has described integration of diodes into spirals and dipoles as a means of achieving a low-cost integrated element and phase shifter. This subsection analyzes a circular microstrip element in a reflectarray configuration. The characteristics of the element in an array are examined using the numerical solution of an integral equation for the microstrip current.

To assess the validity of the solution we consider the following: (1) the convergence of the numerical solution, (2) the solution of the geometry without a ground plane and dielectric for which theoretical and experimental results are given by Chen[6] and Eggimann and Collin;[7] and (3) a comparison of the theoretical results for a microstrip element with experimental results obtained using waveguide simulation techniques.

Data is then given illustrating the effect of polarization, incidence angle, substrate loss and thickness, and array grid spacing. It is shown that these parameters have a significant effect on bandwidth, loss, and resonant frequency of the element.

B. THEORY

A circular microstrip element may be used as a reflectarray element by mounting diodes at a fixed radius from the center as shown in Figure 2. (Additional details of diode mounting techniques and performance data can be found in later sections.) We note that this radius is larger than the feedpoint mounts used by Phelan[3,4,5] for spiral and dipole elements. The basic principle of operation is the same as that described by Phelan.[3] The phase of the circularly polarized wave is controlled by shorting diodes at varying angular locations. In the plane of the shorted diode, the element is approximately a short. The orthogonal linear polarization couples into the resonant element and approximately sees an open circuit.

An analysis of the element with the diodes present would be very complicated. For many elements the diodes minimally affect the resonant frequency and element loss. Hence, we examine the geometry without any diodes or a center shorting pin. This model predicts the essential parameters of loss and bandwidth. The exact resonant frequency depends on the diode loading but can also be predicted with this model within a few percent.

3

DIODES
(IF REFLECTARRAY)

DIODES
(IF REFLECTARRAY)

d_2

d_1

z

ϵ

d

GROUND PLANE

$2a$

d_2

d_1
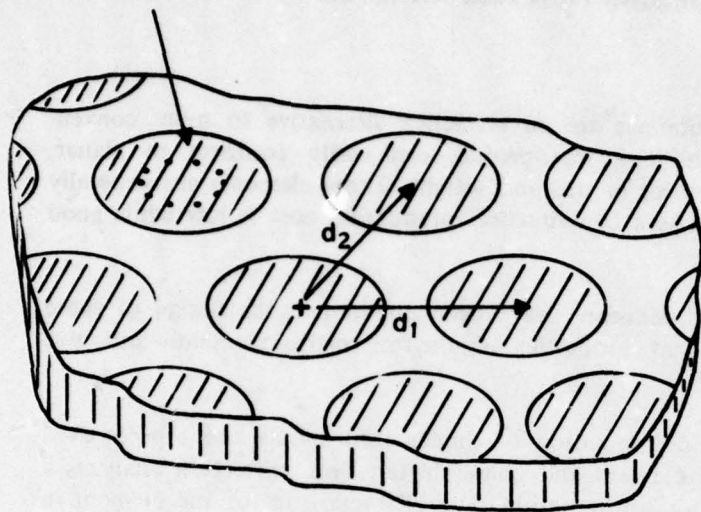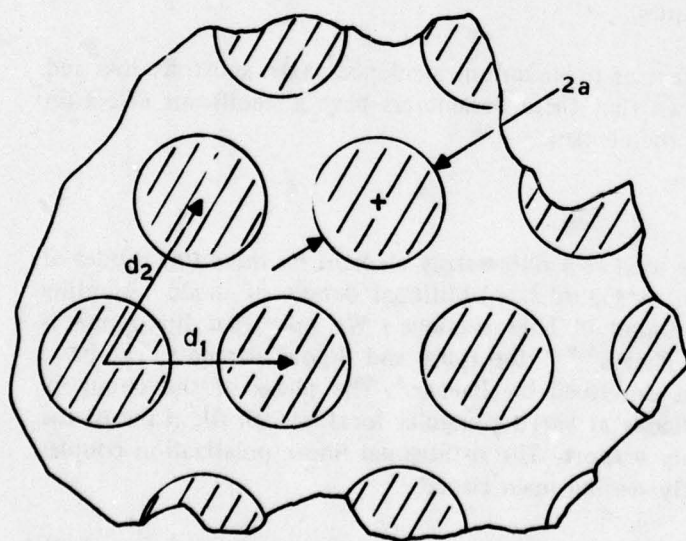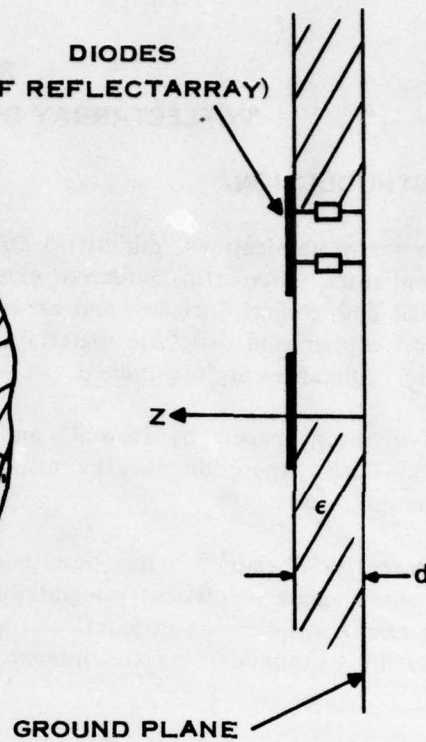
MICROSTRIP ELEMENT ARRAY

Figure 2. Geometry of Microstrip Element

4

The problem thus reduces to the analysis of the scattering from a periodic array of disks on a dielectric substrate above a ground plane. We will only analyze the specular reflection. In an actual reflectarray configuration, we note that an additional phase gradient is induced by the phase shift element allowing one to scan the reflected wave. This could be approximately analyzed by introducing the desired phase gradient into the scattered component of the field but is not done in this report.

The analysis of this geometry proceeds in a similar manner to that used by Montgomery[8] in analyzing polarizer problems. For completeness, we outline the solution, using similar notation.

We first consider the field in the absence of the microstrip scatterer. In the region $z \geq d$, we expand the field:

$$\underline{E}_T^{inc}(\underline{r}) = \sum_{m=1}^{2} a_m^{inc} [\exp(j\gamma z) + R_m \exp(-j\gamma z)] \exp(-j \underline{k}_{TOO} \cdot \underline{r}_T) \underline{\kappa}_{moo} \qquad (1)$$

$$\underline{H}_T^{inc}(\underline{r}) = -\sum_{m=1}^{2} a_m^{inc} \eta_{moo} [\exp(j\gamma z) - R_m \exp(-j\gamma z)] \exp(-j\underline{k}_{TOO} \cdot \underline{r}_T) \underline{e}_z \times \underline{\kappa}_{moo} \qquad (2)$$

and for $0 \leq z \leq d$

$$\underline{E}_T^{inc}(\underline{r}) = \sum_{m=1}^{2} b_m^{inc} \sin \Gamma z \exp(-j\underline{k}_{TOO} \cdot \underline{r}_T) \underline{\kappa}_{moo} \qquad (3)$$

$$\underline{H}_T^{inc}(\underline{r}) = j \sum_{m=1}^{2} b_m^{inc} \xi_{moo} \cos \Gamma z \exp(-j\underline{k}_{TOO} \cdot \underline{r}_T) \underline{e}_z \times \underline{\kappa}_{moo} \qquad (4)$$

where

$$\underline{k}_{Tpq} = \underline{k}_T + p\underline{k}_1 + q\underline{k}_2$$

$$\underline{k}_T = k_o \sin\theta \cos\phi \, \underline{e}_x + k_o \sin\theta \sin\phi \, \underline{e}_y$$

$$\underline{k}_1 = -2\pi/A \, \underline{e}_z \times \underline{d}_2, \quad \underline{k}_2 = 2\pi/A \, \underline{e}_z \times \underline{d}_1$$

$$\gamma = (k_o^2 - \underline{k}_{Tpq} \cdot \underline{k}_{Tpq})^{1/2}$$

$$\Gamma = (k^2 - \underline{k}_{Tpq} \cdot \underline{k}_{Tpq})^{1/2}$$

k_o = propagation constant of media, $z \geq d$

k = propagation constant of media, $0 \leq z \leq d$

θ, ϕ = standard spherical coordinates of incident wave

$\underline{r}_T = x \, \underline{e}_x + y \, \underline{e}_y$

$A = |\underline{d}_1 \times \underline{d}_2|$, periodic cell area
  $\underline{d}_1, \underline{d}_2$ lattice vectors (reference Figure 2)

$$\underline{\kappa}_{1pq} = \underline{k}_{Tpq} / |\underline{k}_{Tpq}|, \text{ TM modes}$$
$$\underline{\kappa}_{2pq} = \underline{e}_z \times \underline{\kappa}_{1pq}, \text{ TE modes}$$
$$\eta_{1pq} = k_o \eta_o / \gamma, \quad \eta_{2pq} = \gamma \eta_o / k_o$$
$$\xi_{1pq} = k \eta / \Gamma, \quad \xi_{2pq} = \Gamma \eta / k$$
$$\eta_o = \sqrt{\epsilon_o / \mu_o}, \quad \eta = \sqrt{\epsilon / \mu}$$

Matching the field Equations (1) through (4) at $z = d$, we easily find

$$R_m = \exp(j2\gamma d) \frac{\eta_{moo} + j\xi_{moo} \cot \Gamma d}{\eta_{moo} - j\xi_{moo} \cot \Gamma d} \tag{5}$$

and

$$I_m{}^{inc} = a_m{}^{inc} \csc \Gamma d \, [\exp(j\gamma d) + R_m \exp(-j\gamma d)] \tag{6}$$

We note that when the d electric substrate is lossless, $|R_m| = 1$.

Now consider the field due to the scattered current density on the microstrip. For $z \geqslant d$

$$\underline{E}_T^s (\underline{r}) = \sum_p \sum_q \sum_m d_{mpq} \exp(-j\gamma z) \exp(-j\underline{k}_{Tpq} \cdot \underline{r}_T) \, \underline{\kappa}_{mpq} \tag{7}$$

$$\underline{H}_T^s (\underline{r}) = \sum_p \sum_q \sum_m \eta_{mpq} \, d_{mpq} \exp(-j\gamma z) \exp(-j\underline{k}_{Tpq} \cdot \underline{r}_T) \, \underline{e}_z \times \underline{\kappa}_{mpq} \tag{8}$$

and for $0 \leqslant z \leqslant d$

$$\underline{E}_T^s (\underline{r}) = \sum_p \sum_q \sum_m c_{mpq} \sin \Gamma z \exp(-j\underline{k}_{Tpq} \cdot \underline{r}_T) \, \underline{\kappa}_{mpq} \tag{9}$$

$$\underline{H}_T^s (\underline{r}) = j \sum_p \sum_q \sum_m \eta_{mpq} \, c_{mpq} \cos \Gamma z \exp(-j\underline{k}_{Tpq} \cdot \underline{r}_T) \, \underline{e}_z \times \underline{\kappa}_{mpq} \tag{10}$$

Matching the tangential electric field yields

$$d_{mpq} \exp(-j\gamma d) = c_{mpq} \sin \Gamma d \tag{11}$$

The tangential magnetic field is discontinuous as determined by the current on the microstrip.

$$\underline{e}_z \times [\underline{H}_T{}^s (z = d^+) - \underline{H}_T{}^s (z = d^-)] = \underline{J} (\underline{r}_T) \tag{12}$$

6

when $r_T \in$ microstrip element. Using Equations (8), (10), (11) and the orthogonality of the Floquent modes, we easily find

$$d_{mpq} = -[\eta'_m]^{-1} \frac{\exp(j\gamma d)}{A} \int_{\underline{r}_T \in A'} \underline{\kappa}_{mpq} \cdot \underline{J} (\underline{r}_T) \exp(jk_{Tpq} \cdot \underline{r}_T) d\underline{r}_T \qquad (13)$$

where

$$\eta'_m = \eta_{mpq} - j\xi_{mpq} \cot \Gamma d$$

The total electric field is a superposition of the incident field Equations (1), (3) and the scattered field Equations (7), (9) [using Equations (11) and (13)]. For $z \geq d$ we have

$$\underline{E}_T (\underline{r}) = \sum_{m=1} a_m^{inc} |\exp(j\gamma z) + R_m \exp(-j\gamma z)] \exp(-j\underline{k}_{T00} \cdot \underline{r}_T) \underline{\kappa}_{moo}$$

$$-\sum_p \sum_q \sum_m [\eta'_m]^{-1} \frac{\exp(j\gamma d)}{A} \int_{\underline{r}_T \in A'} \underline{\kappa}_{mpq} \cdot \underline{J}(\underline{r}'_T) \exp(jk_{Tpq} \cdot \underline{r}'_T) d\underline{r}'_T$$

$$\cdot \exp(-j\gamma z) \exp \underline{r}_T \in A' (-jk_{Tpq} \cdot \underline{r}_T) \underline{\kappa}_{mpq} \qquad (14)$$

All boundary conditions have been satisfied now except we must still force the tangential electric field to vanish on the surface of the microstrip elements. Equating Equation (14) to zero at $z = d$ over the element surface yields the desired integral equation for the current density. A Galerkin solution is used to solve the integral equation. We expand the current in the series

$$\underline{J} (\underline{r}_T) = \sum_{n=1}^{N} g_n \underline{h}_n (\underline{r}_T) \qquad (15)$$

where $\underline{h}_n (\underline{r}_T)$ is a convenient basis. Substitution of Equation (15) into the integral equation and the subsequent inner product with $\underline{h}_\varrho(\underline{r}_T)$ yields the matrix equation

$$\sum_{m=1}^{2} a_m^{inc} [\exp(j\gamma d) + R_m \exp(-j\gamma d)] \underline{\kappa}_{moo} \cdot \widetilde{\underline{h}}_\varrho^* (\underline{k}_{T00})$$

$$= \sum_{n=1}^{N} g_n \left\{ \frac{1}{A} \sum_p \sum_q \sum_m [\eta'_m]^{-1} \underline{\kappa}_{mpq} \cdot \widetilde{\underline{h}}_\varrho^* (\underline{k}_{Tpq}) \underline{\kappa}_{mpq} \cdot \widetilde{\underline{h}}_n (\underline{k}_{Tpq}) \right\} \qquad (16)$$

7

where

$$\widetilde{h}_n \ (k_{Tpq}) = \int\limits_{r_T \epsilon A'} h(r_T) \exp(jk_{Tpq} \cdot r_T) \ dr_T \tag{17}$$

and the asterisk superscript is complex conjugation.

The basis need only be chosen such that as $N \rightarrow \infty$ the representation is complete. It is convenient to choose the basis to be the dual of the waveguide orthonormal basis $\underline{e}_n(r_T)$ or $\underline{h}_n(r_T) = \underline{e}_z \times \underline{e}_n(r_T)$. Thus, the current component normal to the element edge vanishes since the tangential component of the electric field vanishes. We note that the form of the Equation (16) implies that nonorthogonal basis functions can also be used as long as we can evaluate the Fourier transform Equation (17). Thus, basis functions which satisfy the edge condition can also be used.

Although Equation (16) is arbitrary in the shape of the microstrip element, we will only consider circular microstrip elements in this paper. The Fourier transform of circular waveguide model functions is easily found in cylindrical coordinates. Borgiotti[9] and Amitay, Galindo and Wu[10] have given the desired results.

We note that Equation (16) is very similar in form to the equations encountered in phased array analysis.[10] In fact, existing phased array computer programs can easily be modified for our purpose.

C. POLARIZATION AND SCATTERING CHARACTERISTICS

The equations in the previous subsection were based on expansions in terms of waves TM and TE to z. For $z \geqslant d$, only the propagating modes contribute and we can define a scattering matrix by using Equation (14). For single mode propagation, we define the scattering matrix notation

$$b_1 = S_{11} \ a_1 + S_{12} \ a_2 \tag{18a}$$

$$b_2 = S_{21} \ a_1 + S_{22} \ a_2 \tag{18b}$$

where $a_1 (a_2)$ is the magnitude of the TM(TE) incident field and $b_1 (b_2)$ is the magnitude of the TM(TE) reflected field.

Since the contemplated use is with circularly polarized fields, it is desirable to relate the TM-TE scattering matrix to the circularly polarized scattering matrix.

$$b_r = S_{rr} \ a_r + S_{r\varrho} \ a_\varrho \tag{19a}$$

$$b_\varrho = S_{\varrho r} \ a_r + S_{\varrho\varrho} \ a_\varrho \tag{19b}$$

where the subscripts r and ℓ are short for right and left handed circular polarization.

To relate Equations (18) and (19), we consider the following. For the reflected fields, we can define right- and left-handed basis vectors[11]

$$e_r = \frac{1}{\sqrt{2}} [e_\theta - j e_\phi], \; e = \frac{1}{\sqrt{2}} [e_\theta + j e_\phi] \tag{20}$$

For the incident fields, the basis vectors are the complex conjugate of those in Equation (20). The theta and phi components of the complete spectrum (i.e., transverse and axial components) are easily found to be

$$\underline{e}_\theta \cdot \underline{b} = b_1/\cos \theta, \; \underline{e}_\phi \cdot \underline{b} = b_2 \tag{21}$$

where $\underline{b}$ is the complete spectrum and $\gamma = k_o \cos \theta$. For the reflected fields we use Equations (20) and (21) and find

$$b_r = \underline{e}_r{}^* \cdot \underline{b} = \frac{1}{\sqrt{2}} [b_1/\cos \theta + j b_2] \tag{22a}$$

$$\underline{b}_\ell = \underline{e}_\ell{}^* \cdot \underline{b} = \frac{1}{\sqrt{2}} [b_1/\cos \theta - j b_2] \tag{22b}$$

Similar relations hold for the incident fields. Using these relationships we find:

$$S_{ir} = \frac{1}{2} [(S_{11} - S_{22}) + j (\cos \theta \, S_{21} + S_{12}/\cos \theta)] \tag{23a}$$

$$S_r = \frac{1}{2} [(S_{11} + S_{22}) + j (\cos \theta \, S_{21} - S_{12}/\cos \theta)] \tag{23b}$$

$$S_{\ell r} = \frac{1}{2} [(S_{11} + S_{22}) - j (\cos \theta \, S_{21} - S_{12}/\cos \theta)] \tag{23c}$$

$$S_{\ell\ell} = \frac{1}{2} [(S_{11} - S_{22}) - j (\cos \theta \, S_{21} + S_{12}/\cos \theta)] \tag{23d}$$

The axial ratio of the reflected wave is given by

$$\rho = \frac{\big| |b_r| - |b_\ell| \big|}{|b_r| + |b_\ell|} \tag{24}$$

Other parameters of interest such as polarization loss are similarly found.

As a simple example of the principle of the reflectarray, we consider scattering by two orthogonal elements as shown in Figure 3. We can easily reason that

$$S_{11} = -\cos 2\alpha \qquad S_{21} = -\sin 2\alpha$$

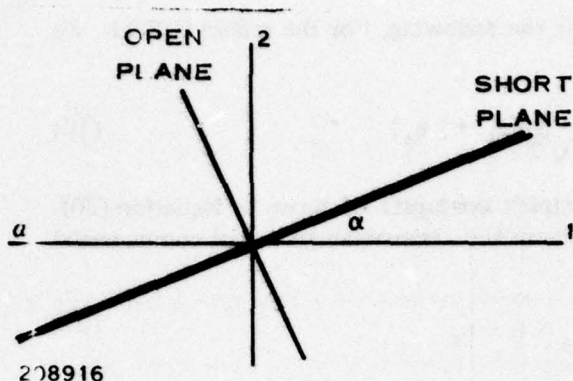$$S_{12} = -\sin 2\alpha \qquad S_{22} = \cos 2\alpha$$

9

Figure 3. Geometry of Idealized Element

Using Equation (23) we find at $\theta = 0$ degree that

$$b_r = \exp(j\,2\alpha)\,a_r$$

$$b_\varrho = -\exp(-j\,2\alpha)\,a_\varrho$$

Thus, the phase shift is equal to twice the rotation angle.

D. NUMERICAL ASSESSMENT

This subsection presents the results which illustrate the convergence of the solution, comparison with other theoretical and experimental data, and compares the theory with new experimental results obtained using a microstrip element in a waveguide simulator.

The necessary check of conservation of energy was applied to lossless structures and agreement obtained to the precision accuracy of the IBM 370 system in the single precision mode. Perhaps the most interesting data was obtained in a short study of the selection of disk modes. Chen[12] has referenced the work of Mittra[13] and Lee[14] as a foundation of convergence theory. The relative convergence phenomenon requires proper selection of the ratio of the number of modes on the disk and the number of Floquet modes. Mittra[13] and Lee[14] have studied geometries defined by constant Cartesian coordinate values. Mastermann[15] has studied cylindrical geometries as well. In general, the modes must be chosen so that the modal coefficients have the proper edge condition. Mittra and Lee[16] have shown that the current at the edges of the disk must behave as

$$J_r(\underline{r}_T) = 0\,[(a-r)^{\frac{1}{2}}] \quad r \to a \tag{25a}$$

$$J_\phi(\underline{r}_T) = 0\,[(a-r)^{-\frac{1}{2}}] \quad r \to a \tag{25b}$$

We may relate these conditions to the asymptotic value of the coefficients, g_n. For a constant angular index, we examine the cylindrical modal functions for large radial indices and find that in order for the series to sum to the singular values in Equation (25) we must have

$$g_m = \begin{cases} 0\,(m^{-1/2}), & m \to \infty, \quad \text{TM modes} \\[2mm] 0\,(m^{-3/2}), & m \to \infty, \quad \text{TE modes} \end{cases} \tag{26}$$

where m is the radial index for a constant angular index.

Before using Equation (26), we consider plotting the data similarly to previous authors;[13,14,15] i.e., vary the number of disk modes for a fixed number of Floquet modes. Figure 4 illustrates the susceptance of two disks in a waveguide as a function of the maximum radial index, m_{max}. For the case of a maximum Floquet index of $p_{max} = 4$ (i.e., 81 Floquet modes since $p_{max} = q_{max}$), there is an abrupt discontinuity at $m_{max} = 3$. This is the value indicated by the equation

10
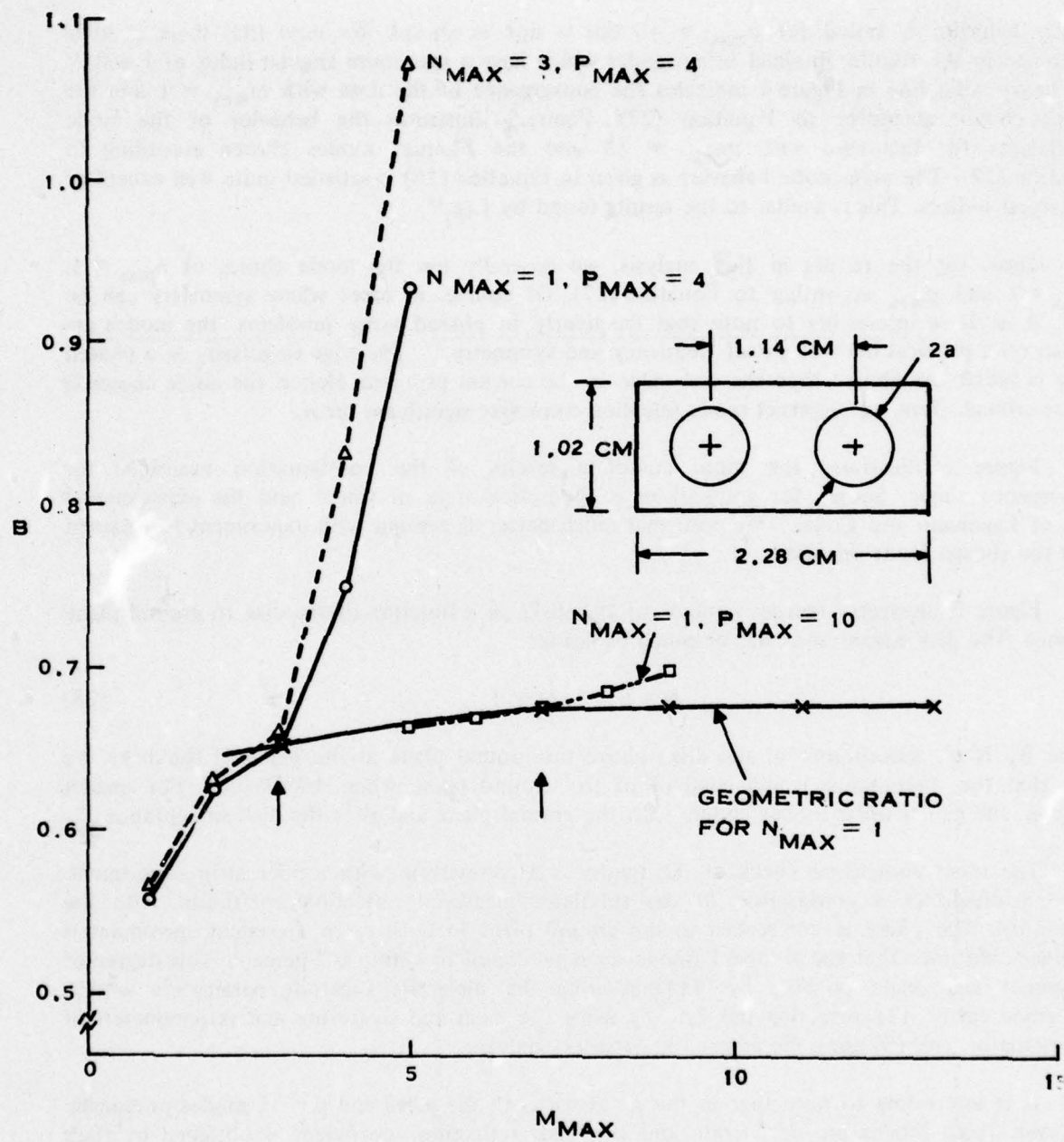
Figure 4. Convergence of Susceptance of Circular Disks in a
Waveguide (2a = 0.381 cm, f = 9 GHz)

208917

11

$$p_{max} = \left[\frac{d_{1x}}{2a} m_{max} \right] \tag{27}$$

Similar behavior is noted for $p_{max} = 10$ but is not as abrupt. We note that there is little difference in the results obtained using modes which have a maximum angular index of 1 and 3. The heavy solid line in Figure 4 indicates the convergence of the data with $m_{max} = 1$ and the modes chosen according to Equation (27). Figure 5 illustrates the behavior of the mode coefficients for this case with $m_{max} = 13$ and the Floquet modes chosen according to Equation (27). The asymptotic behavior as given in Equation (26) is satisfied quite well except at the largest indices. This is similar to the results found by Lee.[14]

Thus, for the results in this analysis, we generally use the mode choice of $n_{max} = 1$, $m_{max} = 7$ and p_{max} according to Equation (27). Of course, in cases where symmetry can be used, it is. It is interesting to note that frequently in phased array problems, the modes are chosen on a physical basis of cutoff frequency and symmetry.[17] The edge singularity in a phased array is much less abrupt than the disk edge in the current problem. Hence, the mode choice is not as critical. Here, an incorrect mode selection can cause significant error.

Figure 6 illustrates the more complete results of the configuration examined for convergence above. Shown for comparison is theoretical data of Chen[6] and the experimental data of Eggimann and Collin.[7] We note that much better agreement with experiment is obtained with the chosen mode selection.

Figure 7 illustrates the susceptance of the disks as a function of the disk to ground plane distance. The disk susceptance was obtained by using

$$B = B_T + \cot \gamma d \tag{28}$$

where B_T is the susceptance of the disks above the ground plane at the plane of the disks. We note that the susceptance is independent of the ground plane when $d/\lambda g \geq 0.05$. For smaller spacings, the higher order modes couple with the ground plane and alter the disk susceptance.

The most convincing check of the theory is a comparison with a microstrip experiment. Figure 8 illustrates a comparison of the simulator measured reflection coefficient with the theoretical. The phase is referenced to the ground plane in both cases. Excellent agreement is obtained. We note that the resonant frequency is predicted to within 0.2 percent. This degree of agreement was made possible by: (1) measuring the dielectric substrate parameters with a waveguide cavity, (2) correcting the data by using the measured scattering matrix parameters of the simulator, and (3) using the automatic network analyzer.

It is interesting to note that in the simulator both the $p = 0$ and $p = -1$ modes propagate. However, these modes are degenerate and the total reflection coefficient is obtained by their superposition.

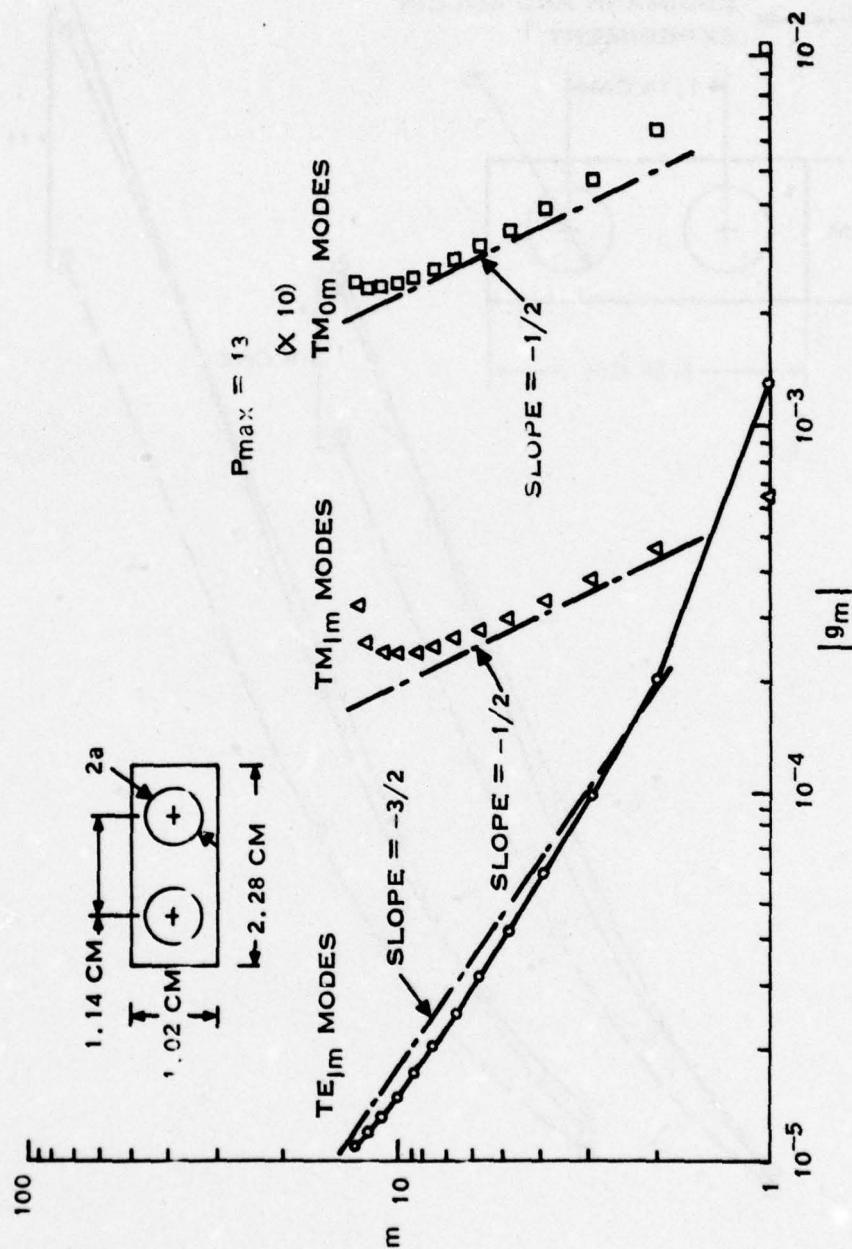Figure 5. Modal Coefficients of Circular Disks in a Waveguide (2a = 0.381 cm, f = 9 GHz)

208918

13
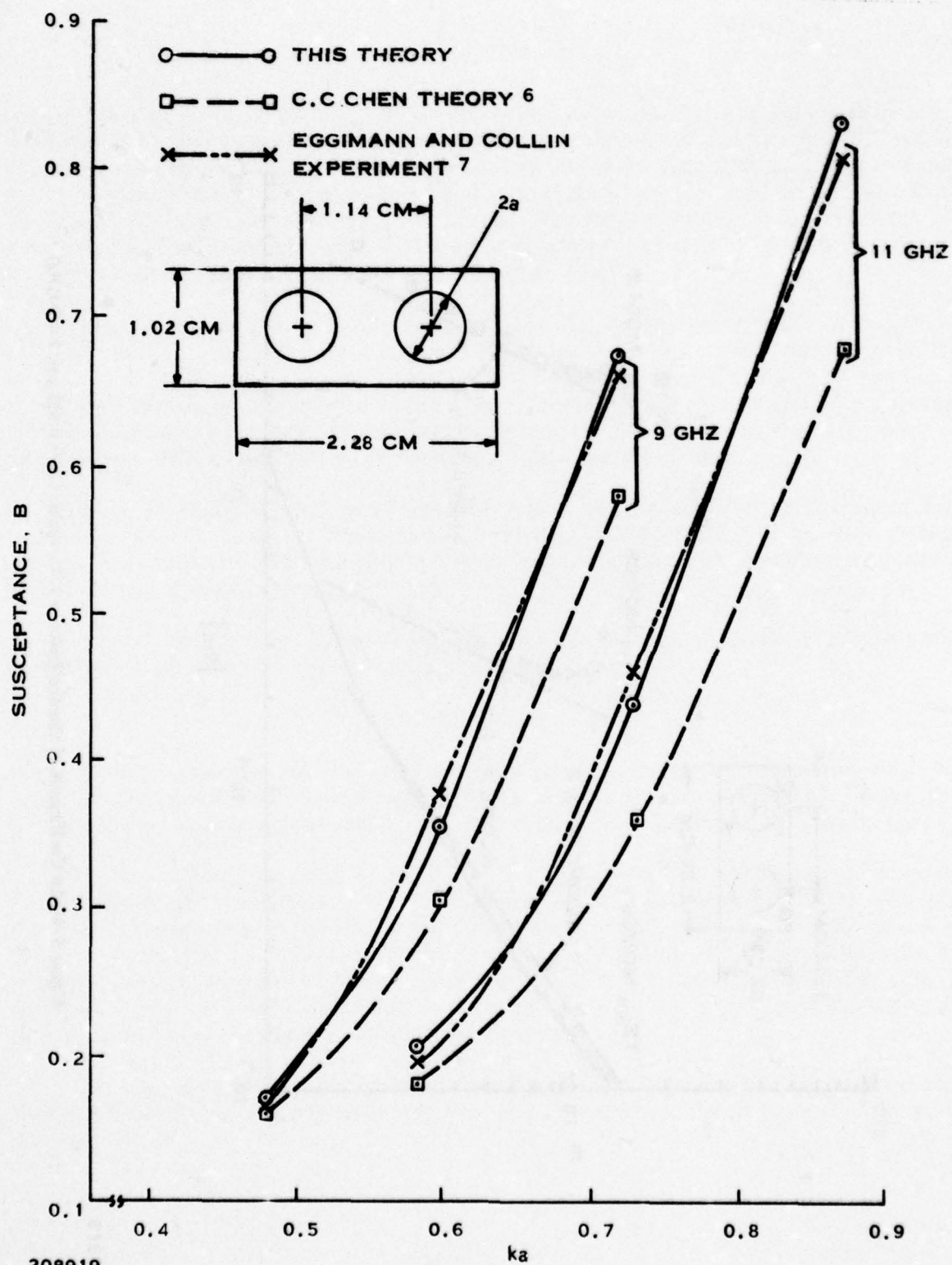
Figure 6. Susceptance of Circular Disks in a Waveguide

208919

14

PERFECT CONDUCTOR

2a

1.14 CM

2.28 CM

1.02 CM

d

B

2.0

1.0

0

0.1　0.2　0.3
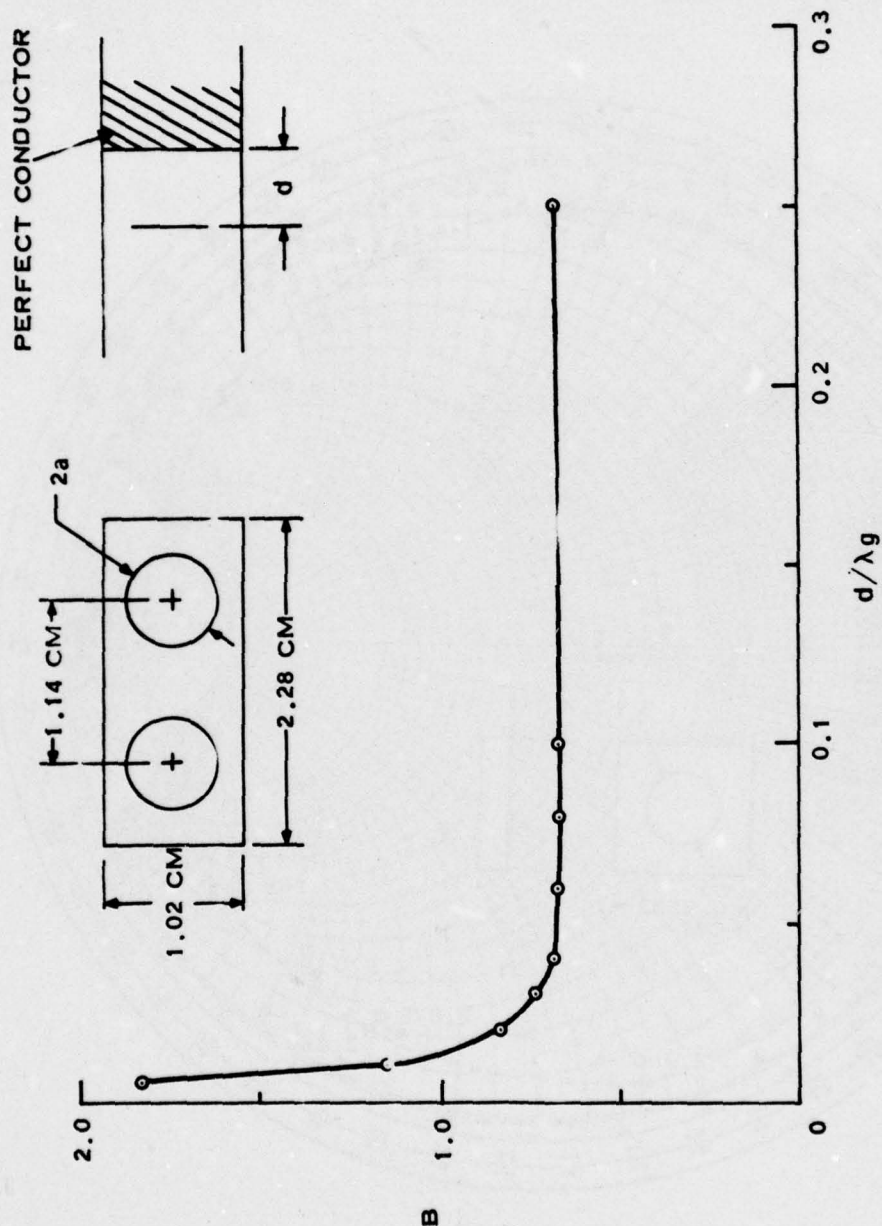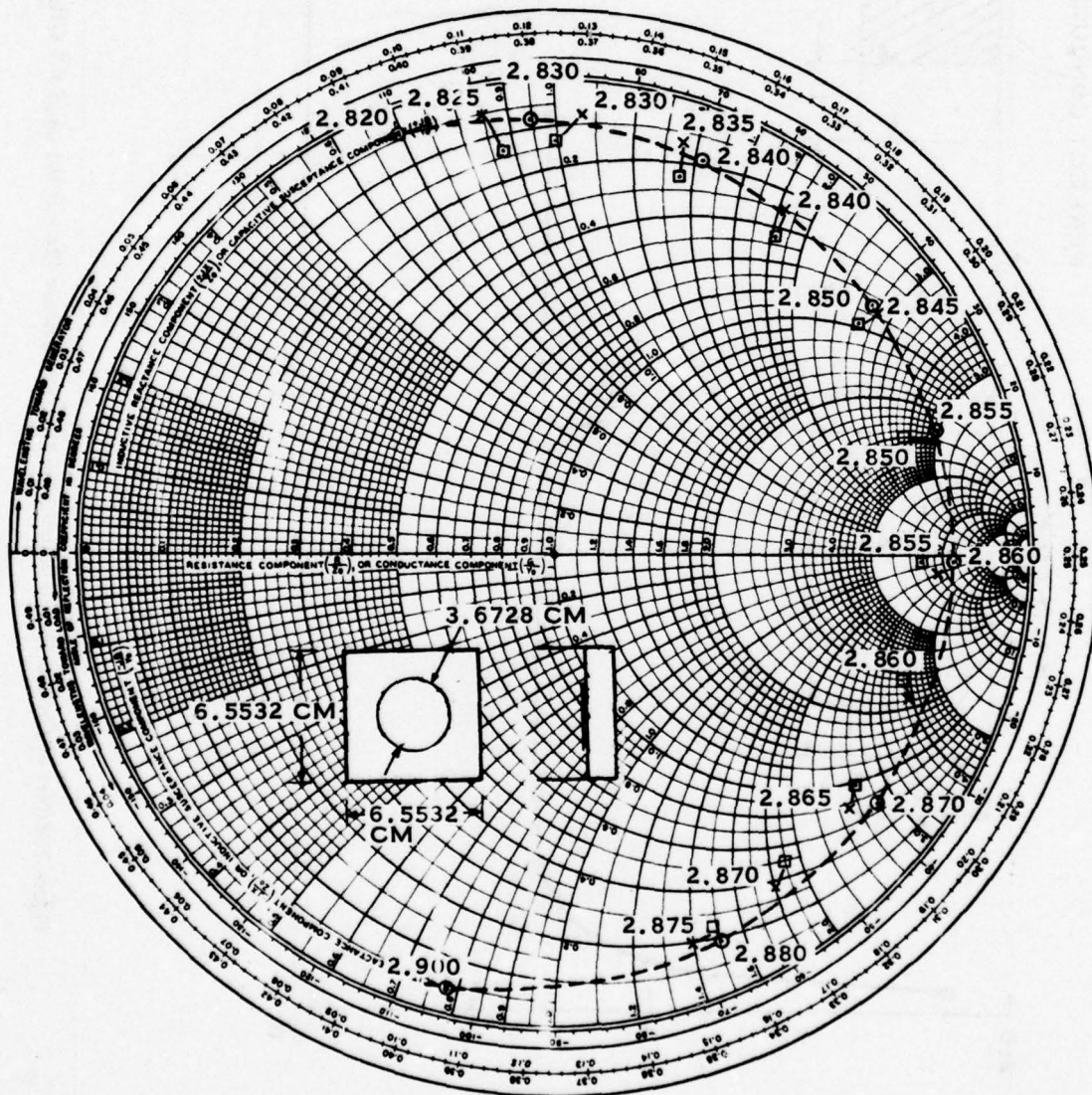
d/λg

Figure 7. Effect of Ground Plane Proximity on Disk Susceptance (2a = 0.381 cm, f = 9 GHz)

208920

15

Figure 8. Comparison of Microstrip Element Theory and Experiment

E.   THEORETICAL RESULTS

The experimental data illustrates that the return loss at resonance is about −1.4 dB. Similar data was observed with the diodes mounted in the element. In fact, this theoretical study was initiated to find the source of this loss and possible techniques for reducing it. As is clear from the data, the loss is due to the dielectric. It is well known that microstrip losses depend strongly on the substrate thickness.[18] Figure 9 illustrates the reflection coefficient in the simulator environment for an 0.3048-cm substrate. We note that the resonant frequency has been lowered and the return loss decreased to about −0.7 dB.

Figure 10 illustrates the effect of decreasing the element spacing. The loss at resonance has decreased to about −0.4 dB. We note that this data also illustrates the effect of the loss tangent on the results. The loss tangent effects the reflection coefficient phase minimally. The dielectric loss primarily changes the magnitude of the reflection coefficient. This data is calculated for the case of 0-degree incidence angle. As a comparison, Figure 11 illustrates the 0-degree incidence case for the geometry examined in the simulator. The incidence angle variation primarily effects the resonant frequency. The loss characteristics are essentially unchanged with scan angle. In comparing the results of Figures 10 and 11, we note that the grid selection has lowered the resonant frequency by about 3 percent. It is interesting that we can calculate the resonant frequency of the isolated disk using Itoh's[19] theory as given in Coen and Gladwell.[20] For the current parameters we find (using the gate function) that $f_o = 2.832$ GHz when $d = 0.15022$ cm and $f_o = 2.707$ GHz when $d = 0.3048$ cm.

Figure 12 illustrates the combined effect of an increase in substrate height and decrease of grid spacing. The resonant frequency has decreased further and the return loss at resonance is now less than   0.2 dB.

The above data has shown that it is clearly possible to dramatically change resonant frequency and loss by the selection of substrate thickness and grid spacing. All the data was for TE incident polarization either in a simulator or at 0-degree incidence. Figure 13 illustrates the effect of polarization and incidence angle variation at a single frequency. The results are somewhat indistinguishable between TE or TM polarization out to $\theta = 40$ degrees. However, the phase of the reflection coefficient (and hence the resonant frequency) is a strong function of the incidence angle. The magnitude of the reflection coefficient changes little with incidence angle.

Implicit in the data presented thus far has been the bandwidth. However, we must be careful in defining the bandwidth.

If we consider the array to be a resonator, the 3-dB bandwidth is determined from the frequencies where the reflection coefficient has the magnitude[21]

$$|R|^2 = (|R_0|^2 + |R'|^2)/2 \tag{28}$$

where R_0 is the reflection coefficient at resonance and R' is the reflection coefficient far away from resonance. If $|R_0| = 0$ and $|R'| = 1$, we have the well known result that $R = \frac{1}{2}$. For example, the bandwidth of the element with the data in Figure 8 is approximately 70 to 80 MHz (or about 2.6 percent). The bandwidth of the compact grid example in Figure 10 is approximately 180 MHz (6.5 percent). The low loss example in Figure 12 has a bandwidth of approximately

360 MHz (14.1 percent). Hence, all efforts to decrease the loss have also increased the bandwidth.

However, for the reflectarray mode of operation the half power bandwidth may not be the desired measure of bandwidth. A more meaningful bandwidth measure can be derived by considering the polarization characteristics of the array. In particular, the limiting factor is easily seen to be the depolarization of the reflected field. As an example, we consider that the short circuit reflection coefficient is perfect and equal to -1. The open circuit reflection coefficient is assumed to have only a phase error and to be equal to $\exp(j\theta)$. We can easily find that the cross polarization of the reflect field is:

$$\text{cross polarization} = \sqrt{\frac{1 - \cos\theta}{1 + \cos\theta}}$$

A phase error of 35.1 degrees causes the cross polarization to be -10 dB, while an 11.4-degree error causes a cross polarization level of -20 dB. Thus, we see that the cross polarization bandwidth is as much as an order of magnitude smaller than the half power bandwidth.

$(\epsilon_r = 2.5577,\ \text{TAN}\ \delta = 0.002,\ D = 0.3048\ \text{CM})$
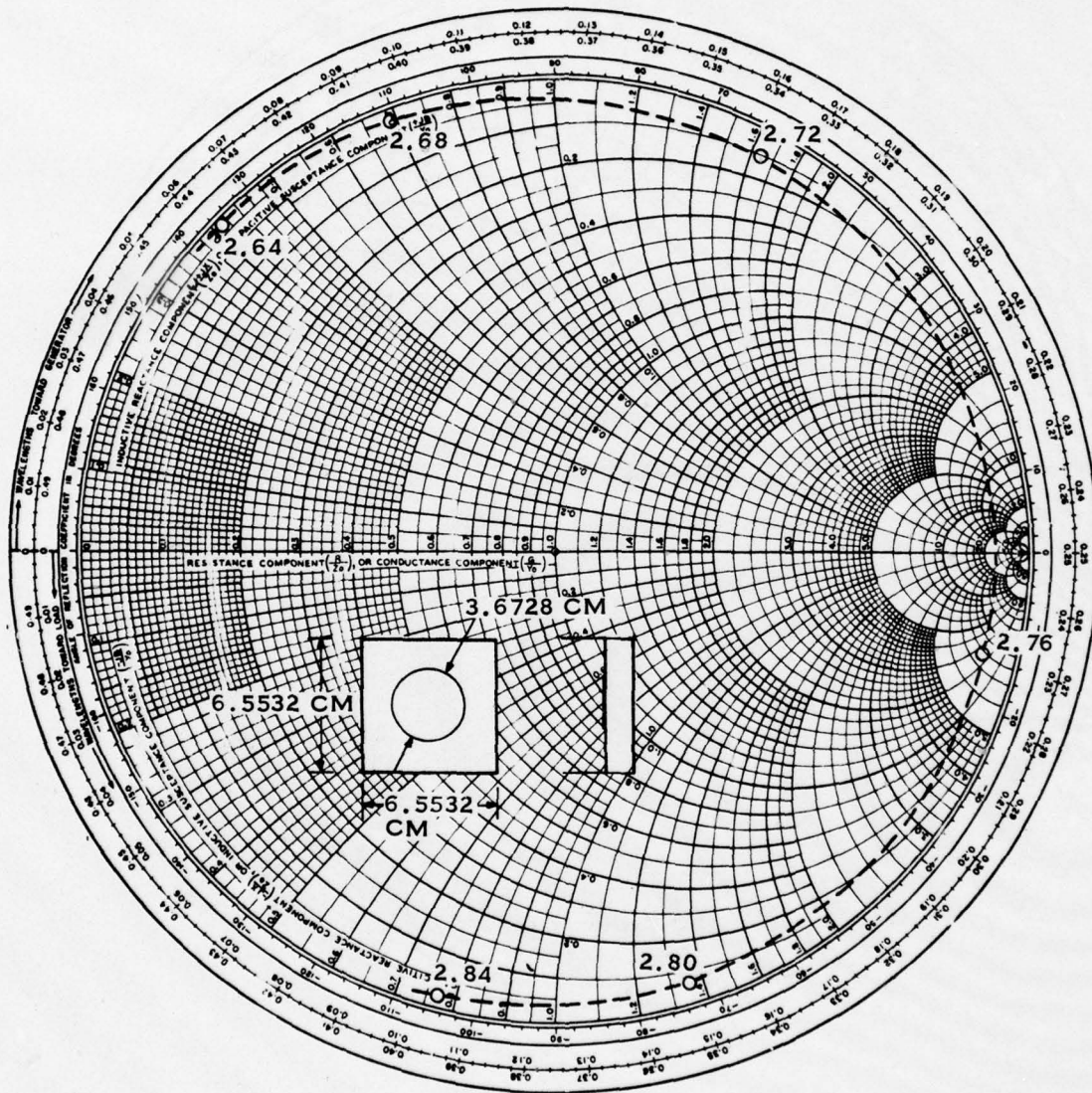
208922

Figure 9. Effect of Substrate Thickness

19

$(\epsilon_r = 2.5577, \text{ TAN } \delta = \text{VARIABLE}, \text{ D} = 0.15022 \text{ CM},$
$\text{D}_X = \text{D}_{2Y} = 3.7592 \text{ CM}, \text{ D}_{1Y} = \text{D}_{2X} = 0, \quad \theta = 0°)$
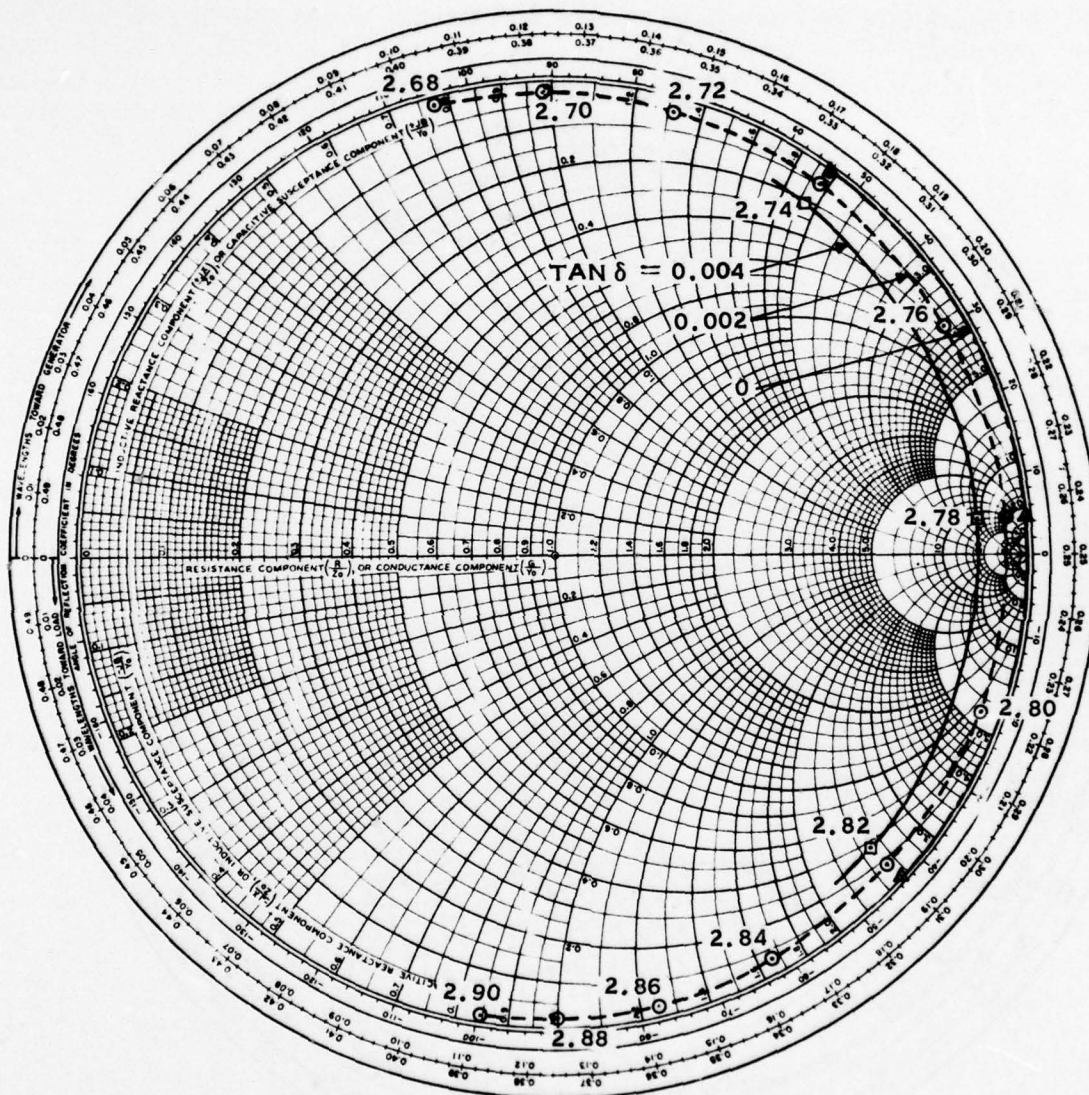
Figure 10. Effect of Grid Spacing

20

$(\epsilon_r = 2.5577, \ \text{TAN} \ \delta = 0.002, \ D = 0.15022 \ \text{CM},$

$D_{1X} = D_{2Y} = 6.5532 \ \text{CM}, \ D_{1Y} = D_{2X} = 0, \ \theta = 0°)$
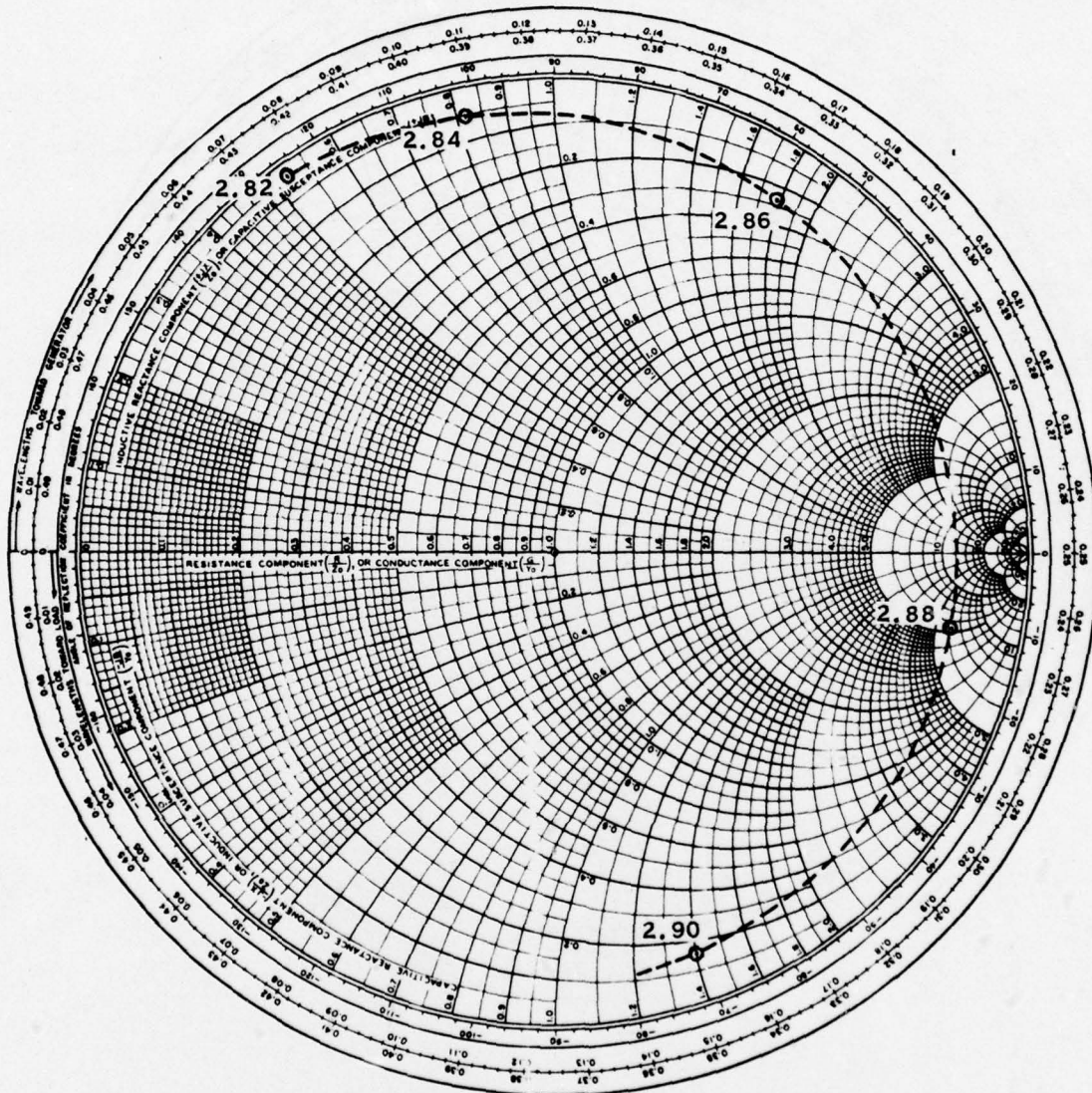
Figure 11. Simulator Geometry at 0° Incidence Angle

21

$(\epsilon_r = 2.5577,\ \text{TAN}\,\delta = 0.002,\ D = 0.3048\ \text{CM},$

$D_{1X} = D_{2Y} = 3.7592\ \text{CM},\ D_{1Y} = D_{2X} = 0,\ \theta = 0°)$

Figure 12. Combined Effect of Increasing Substrate Thickness and
Decreasing Element Spacing

2)8925

22

$(\epsilon_r = 2.5577,\ \text{TAN}\ \delta = 0.002,\ D = 0.15022\ \text{CM},\ D_{1X} = D_{2Y} = 3.7592\ \text{CM},$
$D_{1Y} = D_{2Y} = 0;\ \circ\!\!-\!\!-\!\!-\!\!-\!\!-\!\!\circ\ \text{TE POLARIZATION},$
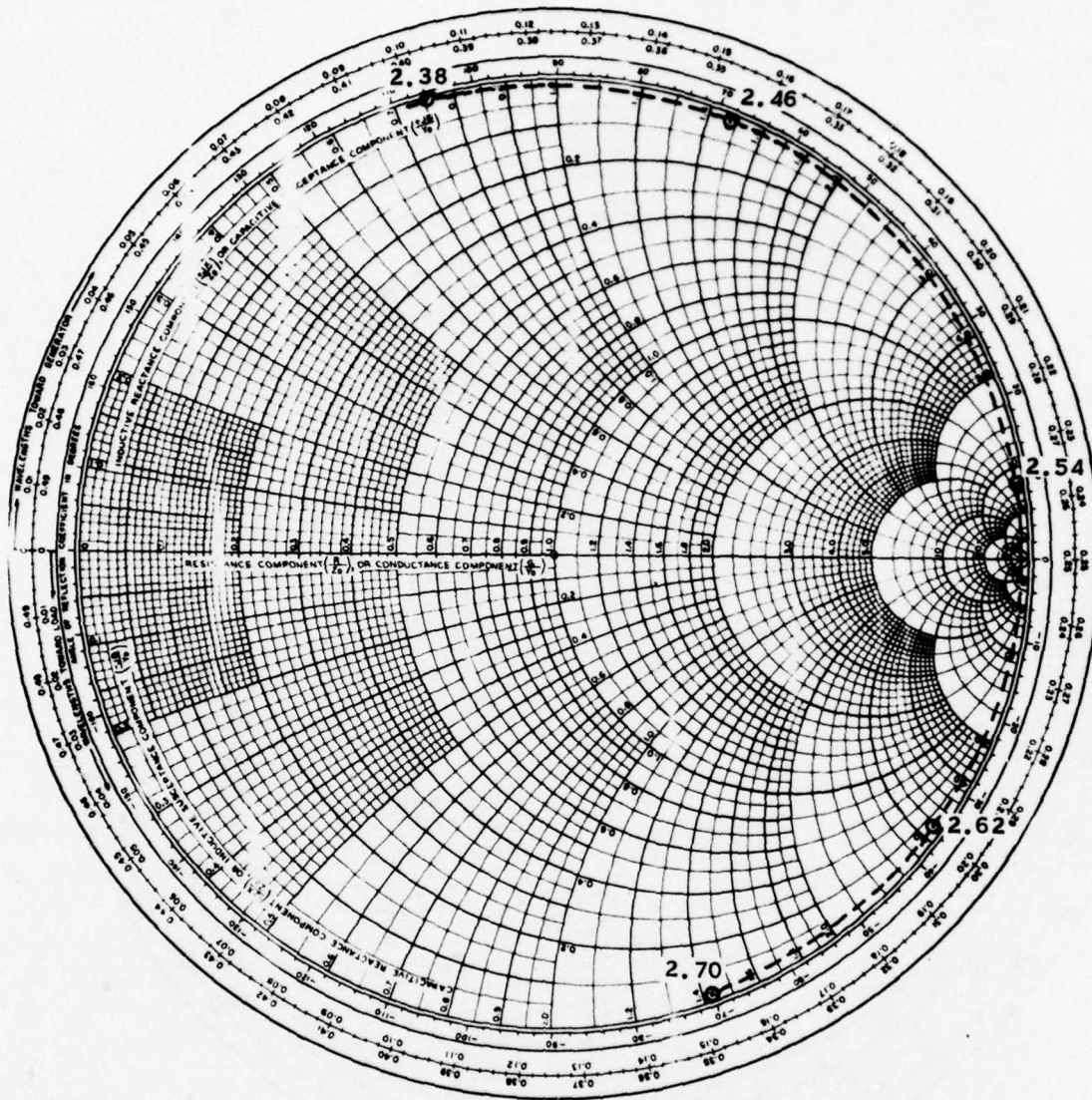$\square\!-\!-\!-\!-\!\square\ \text{TM POLARIZATION},\ \theta = \text{VARIABLE},\ \phi = 0°)$
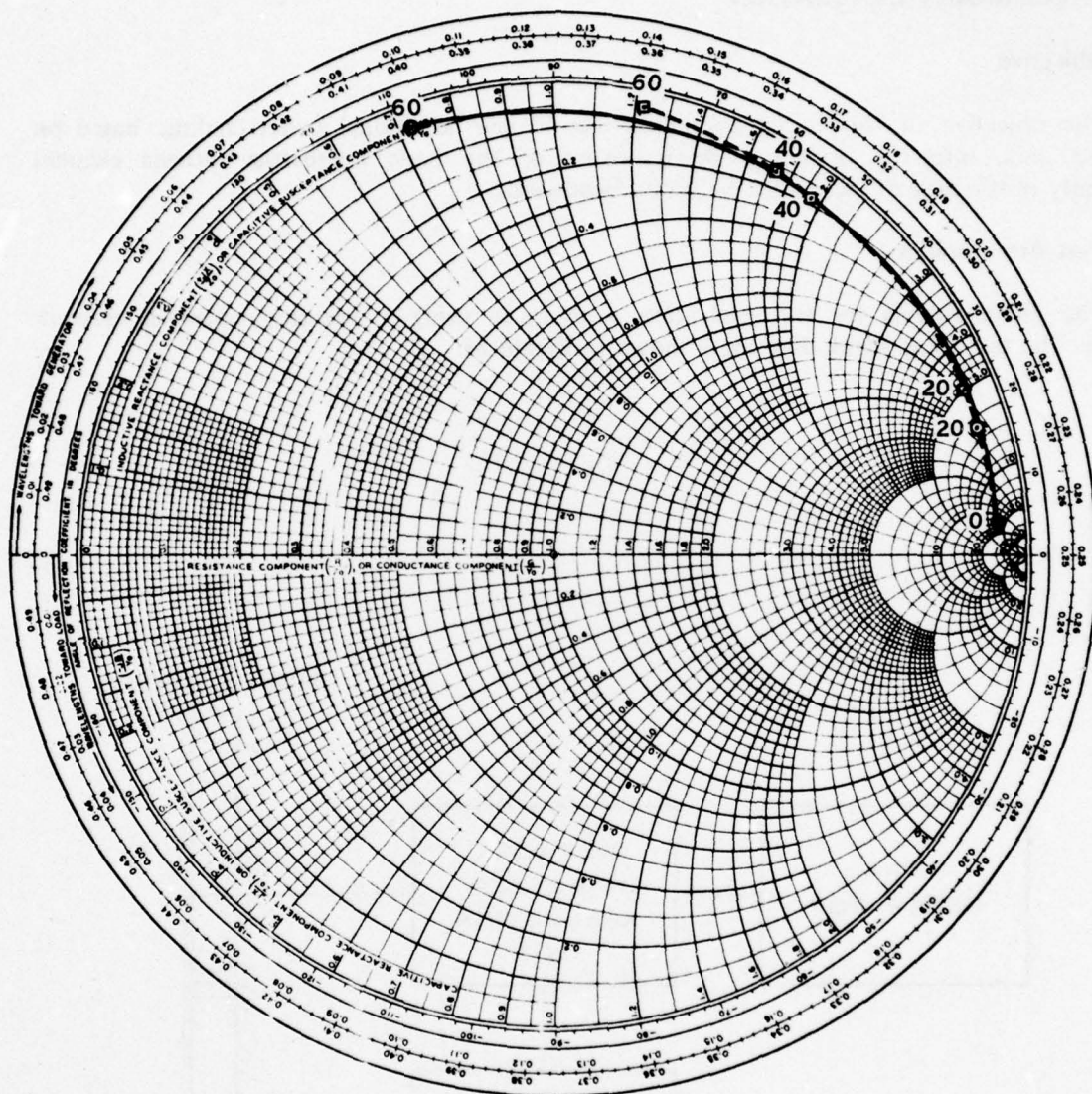
208926

Figure 13. Effect of Scan Angle and Polarization on Reflection Coefficient

23

SECTION III

EVALUATION RESULTS

\. PRELIMINARY EVALUATION

1 Objective

The objective of this initial evaluation was to gain additional understanding, based on measured data, into the operating characteristics of the basic microstrip antenna element particularly in the area of increasing the useful bandwidth.

2. Test Arrangement

The measurements for this evaluation were made using a manually operated network analyzer. The test setup block diagram is shown in Figure 14.
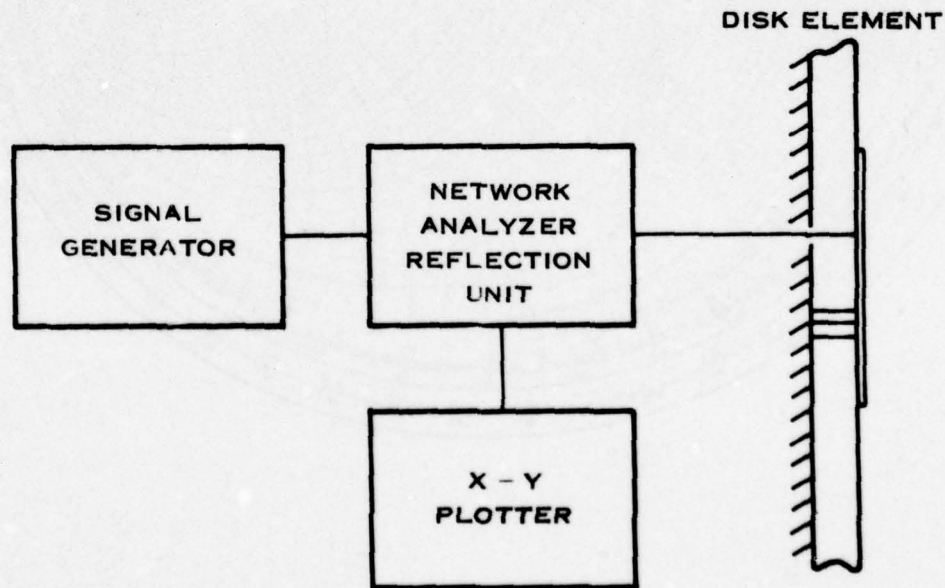
208927

Figure 14. Preliminary Evaluation Test Setup

24

3. Test Procedure

The preliminary evaluation consisted of two series of measurements. The first measurement series were made on an air dielectric element excited at the coaxial ports and operating in the transmission mode. The voltage reflection coefficient looking into the coaxial port was measured as a function of frequency and the element's height above the ground plane while radiating into free space. The distance, b, between the coaxial port and the element's center was held constant. The second measurement series were basically the same as one except these elements were built on 0.06-inch-thick Teflon-fiberglass material. In this instance, the input reflection coefficient was measured as a function of frequency and element geometry.

4. Measured Data

The element under consideration is the center-shorted circular disk element shown in Figure 15. When operating as a transmissive element, this device is fed by an offset electric field probe at a point within the perimeter of the element. The resonant impedance of the element is determined by the height of the element, the dielectric constant, and the distance from the center at which the probe is located. The resonant frequency of the element is determined primarily by the diameter of the element when the cavity formed by the disk and an (assumed) magnetic conducting wall joining the upper and lower conducting surfaces around the periphery will operate in the H_{01} mode. The resonant frequency is approximately given by

$$f_o \cong 1.841c/2\,\pi\,a\sqrt{\epsilon r} \qquad (29)$$

where the multiplicative constant is the first zero of the derivative of the first order Bessel function, c is the free-space speed of light, a is the radius of the disk, and ϵ_r is the dielectric constant of the substrate.

Figure 16 shows the radius of the disk element over the frequency range from 1 to 35 GHz for various dielectric substrates. In the order of increasing dielectric constant, these represent designs for air, Teflon-fiberglass, alumina, and silicon, respectively. The choice of dielectric material will depend on the relative density of elements required by the scan volume and to some extent, on the technique chosen for fabrication of the element.

Figure 17 shows the summarized results of the measurement on the air dielectric model. The element radius, a, was equal to 2.31 inches. The ground plane radius was greater than 10a. Plotted as a function of the ratio of the element's radius to distance above the ground plane, d/a, are the measured resonant resistance, R_s normalized to 50 ohms, the resonant frequency plotted as a percentage difference from the calculated value and the bandwidth expressed as a percentage of the resonant frequency, f_o, in which the input VSWR is less than 2:1.

The search for bandwidth improvement by modifying the element's shape was not successful. Element geometries evaluated included the one suggested in the proposal in addition to other shapes consisting of a disk surrounded by one or more concentric rings. The disk radius was maintained at 0.723 inch. The rings were typically spaced at 0.020 to 0.030 inch and their width varied between 0.050 to 0.100 inch.

No bandwidth improvement was observed.

25

SHORTING PIN

FEED PROBE

COPPER

DIELECTRIC

COPPER

SECTION A–A

COAXIAL PORT
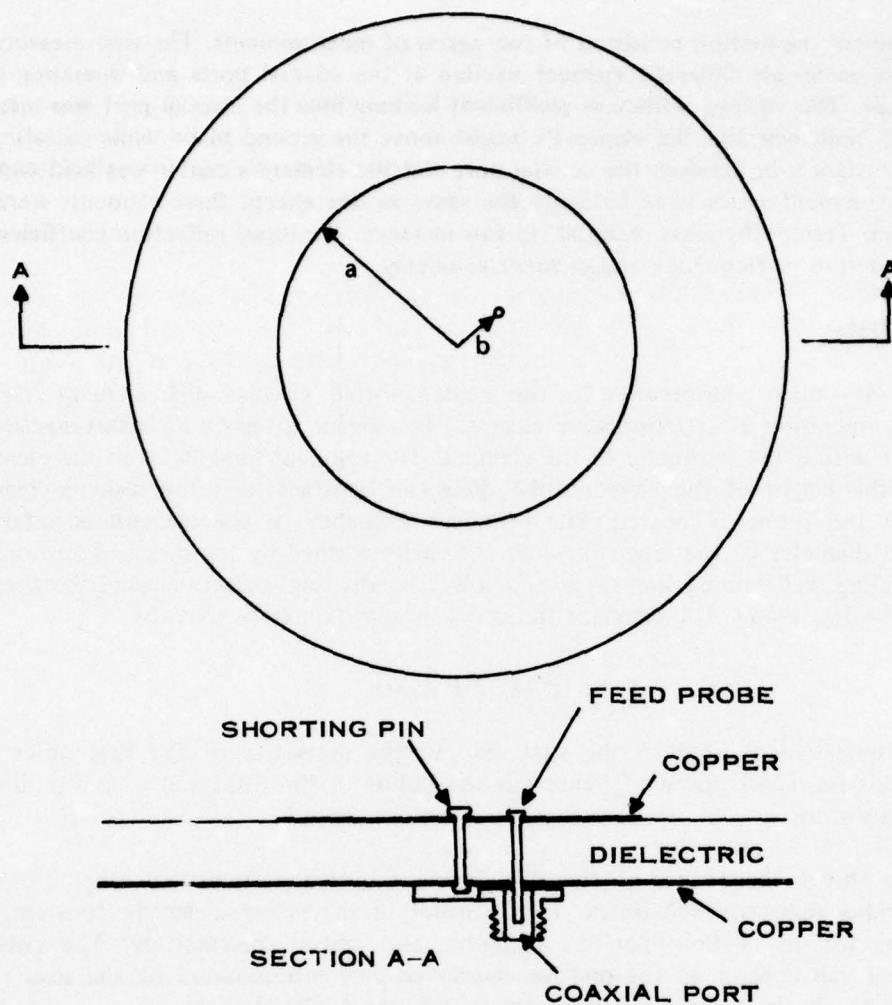
208928

Figure 15. Center-Shorted Circular Disk Element

B. PRIMARY EVALUATION

### 1. Objective

The objective of his evaluation is to determine the feasibility, performance, and design limitations of a diode-loaded microstrip antenna operating in the reflection mode.

2. Test Arrangement

The test setup used for this evaluation is shown in Figure 18. All measurements were made using the Hewlett-Packard Automatic Network Analyzer to ensure the accurate documentation of

26
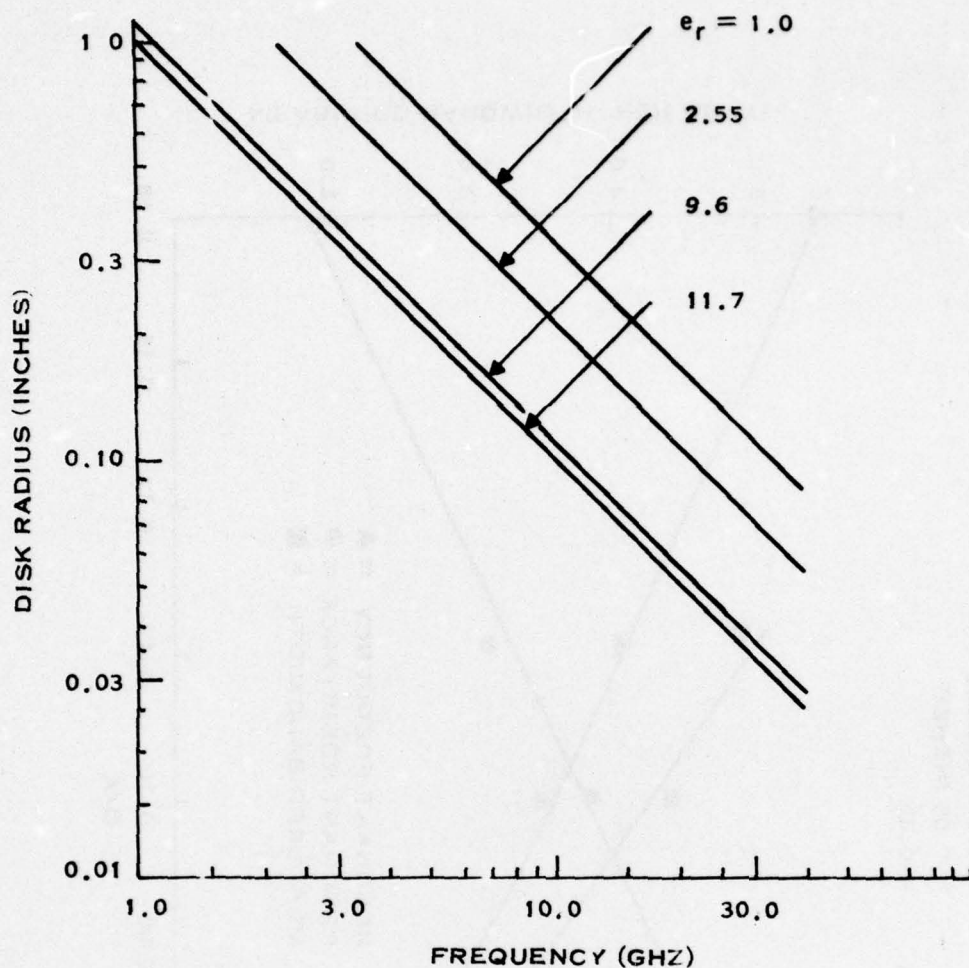
208929

**Figure 16. Radius of Disk Element Versus Frequency With
Dielectric Constant as a Parameter**

both amplitude and phase at known frequencies. The test fixture was a waveguide dual-mode transducer, Figure 19. Since each port excites the TE_{10} and TE_{01} modes with equal amplitudes, the resultant fields are diagonally polarized modes.

Consider the similar geometry and the diode placement as shown in Figure 20. The microstrip element will in general couple the TE_{10} and TE_{01} modes. The exceptions are when $a = 0$, $\pi/2$, π, and $3\pi/2$. Only at these angles will the simulator give valid array simulation. As an example, consider that only the TE_{10} mode is incident. This mode simulates an H-plane incidence (TE polarization). In the simulator, if the orthogonal mode is excited it also propagates in the orthogonal plane with TE polarization. However, when a plane wave excites an array, this

27

Figure 17. Isolated Microstrip Element Characteristics

$F_{CALC.}$ = 1.5 GHZ
ϵ_r = 1
A = 2.307 INCHES
W = 0.06 INCHES
B/A = 0.35

RESONANT FREQUENCY = ▲
RESONANT RESISTANCE = ●
MEASURED BANDWIDTH = ■

MEASURED BANDWIDTH (PER CENT)

RESONANT RESISTANCE (RS/50)
RESONANT FREQUENCY (PER CENT)

D/A

208930

28

AUTOMATIC
NETWORK
ANALYZER

TEST
FIXTURE

ELEMENT
UNDER
TEST

MEASUREMENT
PLANE

PERFORMANCE
PLANE
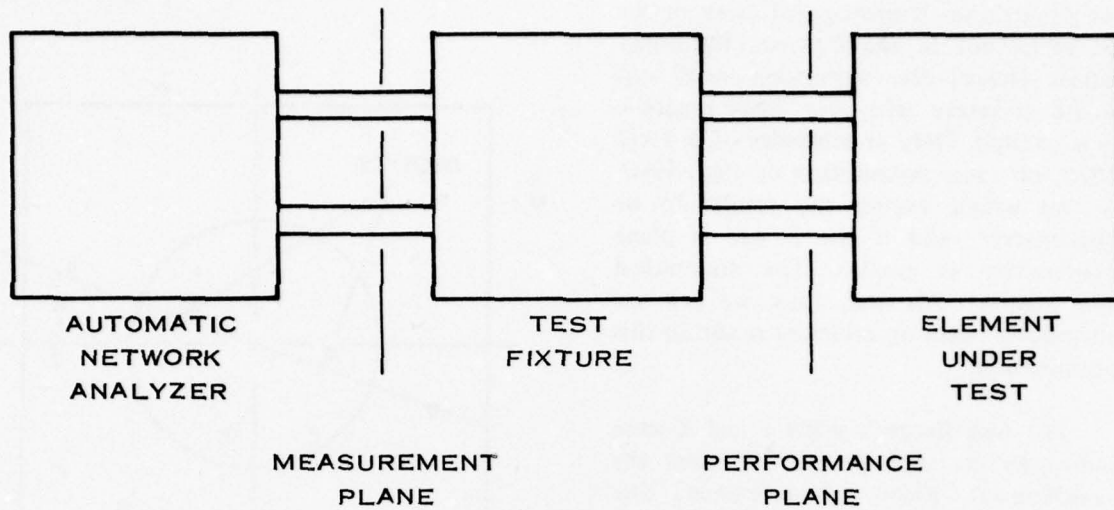
208931

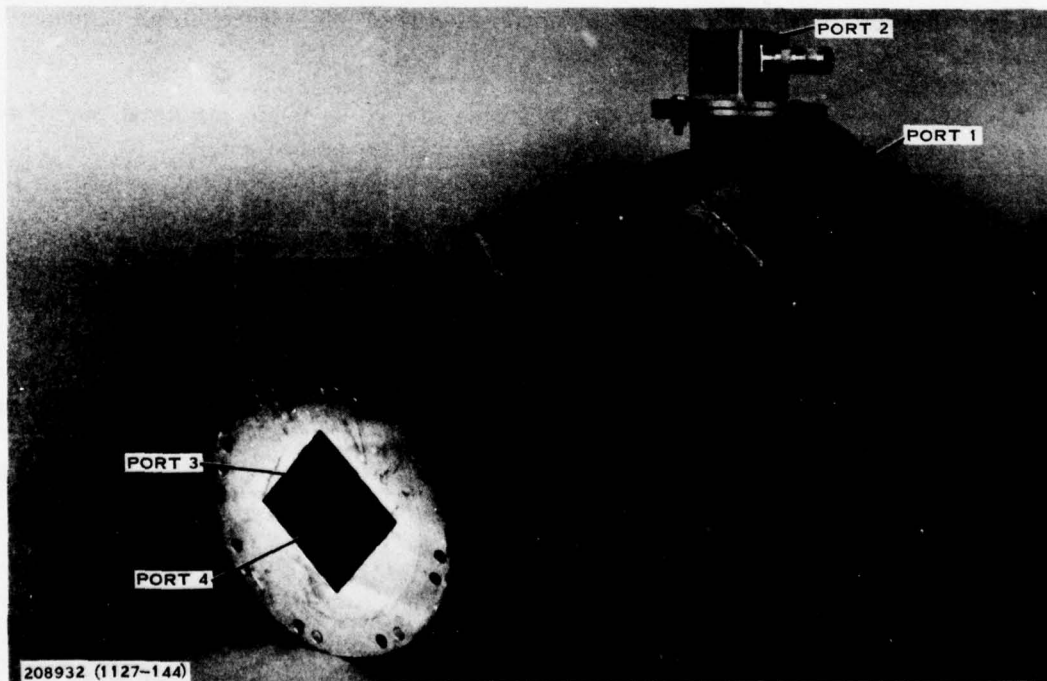Figure 18. Reflectarray Microstrip Element Test Description

Figure 19. Test Fixture

29

cross polarization is propagated away in the same plane but in the E-plane (TM polarization). Hence, the waveguide does not simulate an array whenever cross polarization is excited. Only at multiples of $a = \pi/2$ is there no cross polarization excited. However, we would expect the results to be approximately valid if the E and H plane performance is similar. The theoretical results support this and, thus, we can use the simulator with an arbitrary α within this approximation.

The test fixture's ports 1 and 2 were attached to the analyzer and represent the measurement plane of reference. The element under test was attached to the square waveguide end of the fixture, ports 3 and 4. The performance plane or the plane of reference at which the element's performance is specified is represented by its front surface.

208933

Figure 20. Diode Placement in Simulator

3.   Test Procedure

The test procedure followed to characterize the reflectarray elements consisted of first determining the test fixture's transfer parameters between the planes of measurement and performance.

The test fixture is modeled by the following matrix to relate measured port 1 and 2 reflection and transfer parameters to the element parameters at ports 3 and 4.

$$
\begin{bmatrix} b_1 \\ b_2 \\ b_3 \\ b_4 \end{bmatrix} = \begin{bmatrix} s_{11} & 0 & s_{13} & s_{14} \\ 0 & s_{22} & s_{23} & s_{24} \\ s_{31} & s_{32} & s_{33} & 0 \\ s_{41} & s_{42} & 0 & s_{44} \end{bmatrix} \begin{bmatrix} a_1 \\ a_2 \\ a_3 \\ a_4 \end{bmatrix}
\tag{30}
$$

where s_{12}, s_{21}, s_{34}, and s_{43} were measured to be of the order of -50 dB and were measured to be zero. Then, by definition

$$
b_3 = R_3 a_3
\tag{31}
$$

and

$$
b_4 = R_4 a_4
\tag{32}
$$

30

where R_3 and R_4 are the reflection coefficient of ports 3 and 4. Then taking into account the guide impedance and reciprocity the following equations were written:

$$\frac{S_{13}}{Z_R} = \frac{S_{31}}{Z_S} \tag{33}$$

$$\frac{S_{14}}{Z_R} = \frac{S_{41}}{Z_S} \tag{34}$$

$$\frac{S_{24}}{Z_R} = \frac{S_{42}}{Z_S} \tag{35}$$

and

$$\frac{Z_{23}}{Z_R} = \frac{Z_{32}}{Z_S} \tag{36}$$

where Z_R is the rectangular guide impedance and Z_S is the square guide impedance. Combining Equations (30) through (32) the following equations resulted:

$$S_{11}' = \frac{b_1}{a_1} \bigg|\ a_2 = 0 \ = S_{11} + \frac{S_{13} \cdot S_{31} \cdot R_3}{(1 - S_{33} \cdot R_3)} + \frac{S_{14} \cdot S_{41} \cdot R_4}{(1 - S_{44} \cdot R_4)} \tag{37}$$

$$S_{22}' = \frac{b_2}{a_2} \bigg|\ a_1 = 0 \ = S_{22} + \frac{S_{23} \cdot S_{32} \cdot R_3}{(1 - S_{33} \cdot R_3)} + \frac{S_{24} \cdot S_{42} \cdot R_4}{(1 - S_{44} \cdot R_4)} \tag{38}$$

$$S_{21}' = \frac{b_2}{a_1} \bigg|\ a_2 = 0 \ = \frac{S_{23} \cdot S_{31} \cdot R_3}{(1 - S_{33} \cdot R_3)} + \frac{S_{24} \cdot S_{41} \cdot R_4}{(1 - S_{44} \cdot R_4)} \tag{39}$$

and

$$S_{12}' = \frac{b_1}{a_2} \bigg|\ a_1 = 0 \ = \frac{S_{13} \cdot S_{32} \cdot R_3}{(1 - S_{33} \cdot R_3)} + \frac{S_{14} \cdot S_{42} \cdot R_4}{(1 - S_{44} \cdot R_4)} \tag{40}$$

Then ports 3 and 4 were loaded so that S_{11} and S_{22} were determined from Equations (37) and (38). Hence:

$$S_{11}' = S_{11} ; R_3 = R_4 = 0 \tag{41}$$

$$S_{22}' = S_{22} ; R_3 = R_4 = 0 \tag{42}$$

By using a sliding short at port 3 and a load at port 4, and reversing the ports, the following equations resulted:

$$S_{33} = \frac{R_3 B(S_{11}' A_3 - S_{11}) - R_3 A(S_{11}' B_3 - S_{11})}{R_3 A \cdot R_3 B \cdot (S_{11}' - A_3 - S_{11}' B_4)} ; R_4 = 0 \tag{43}$$

31

and

$$S_{44} = \frac{R_4 B(S_{11}' A_4 - S_{11}) - R_4 A(S_{11}' B_4 - S_{11})}{R_4 A \cdot R_4 B \cdot (S_{11}' A_4 - S_{11}' B_4)} \quad ; R_3 = 0 \tag{44}$$

where $R_3 A$ and $R_3 B$ represents a zero short and a 1-inch offset short, respectively, at port 3. Then the following equations were derived using Equations (37) and (38):

$$S_{14} S_{41} = \frac{(1 - S_{44} \cdot R_4 A)(S_{11}' A_4 - S_{11})}{R_4 A} \quad ; R_3 = 0 \tag{45}$$

$$S_{13} S_{31} = \frac{(1 - S_{33} \cdot R_3 A)(S_{11}' A_3 - S_{11})}{R_3 A} \quad ; R_4 = 0 \tag{46}$$

$$S_{23} S_{32} = \frac{(S_{22}' A_3 - S_{22})(1 - S_{33} R_3 A)}{R_3 A} \quad ; R_4 = 0 \tag{47}$$

and

$$S_{24} S_{42} = \frac{(S_{22} A_4 - S_{22})(1 - S_{44} R_4 A)}{R_4 A} \quad ; R_3 = 0 \tag{48}$$

Equations (33) through (37) were used to resolve the above products. The following equations resulted:

$$S_{41} = \sqrt{\frac{Z_S \cdot S_{14} \cdot S_{41}}{Z_R}} \tag{49}$$

$$S_{31} = \sqrt{\frac{Z_S \cdot S_{13} S_{31}}{Z_R}} \tag{50}$$

$$S_{32} = \sqrt{\frac{Z_S \cdot S_{23} S_{32}}{Z_R}} \tag{51}$$

and

$$S_{42} = \sqrt{\frac{Z_S \cdot S_{24} S_{42}}{Z_R}} \tag{52}$$

Where the sign of the above radicals were determined by substitution into Equations (39) and (40) and comparing with measured data. The test fixture was characterized on the automatic network analyses (ANA) using GPM-1. To accomplish the characterization, the ANA was calibrated in rectangular waveguide (WR284). A standard calibration kit (sliding load, termination, zero short, offset short, two waveguide to APC7 adapters) was used to accomplish this task. The measurement plane was established at the surface of the waveguide flange (Figure 18). Ports 1 and 2 of the test fixture were connected to the ANA (Figure 19). A terminated square waveguide was attached to ports 3 and 4, and measurements were made. Then, a sheet of polarization grid paper was placed in front of the square waveguide termination. Measurements were made with the grid aligned with each of the principle planes of the square

32

waveguide. Next, ai extension (2.460 inches long) was placed between the polarization grid and ports 3 and 4, and measurements were made. The terminations were assumed to be perfect loads or shorts.

The following relations along with the test fixture characterizations relate the element performance at the plane of measurement to the element performance at the plane of performance.

$$\begin{bmatrix} a_3 \\ a_4 \end{bmatrix} = \Gamma \begin{bmatrix} b_3 \\ b_4 \end{bmatrix} \tag{53}$$

$$\Gamma = \begin{bmatrix} R_{33} & R_{34} \\ R_{43} & R_{44} \end{bmatrix} \tag{54}$$

and

$$\begin{bmatrix} b_0 \\ b_1 \end{bmatrix} = \begin{bmatrix} (S_{00}) & (S_{01}) \\ (S_{10}) & (S_{11}) \end{bmatrix} \begin{bmatrix} a_0 \\ a_1 \end{bmatrix} \tag{55}$$

By partitioning the test fixture matrix as shown above and using matrix algebra, the following equations were derived:

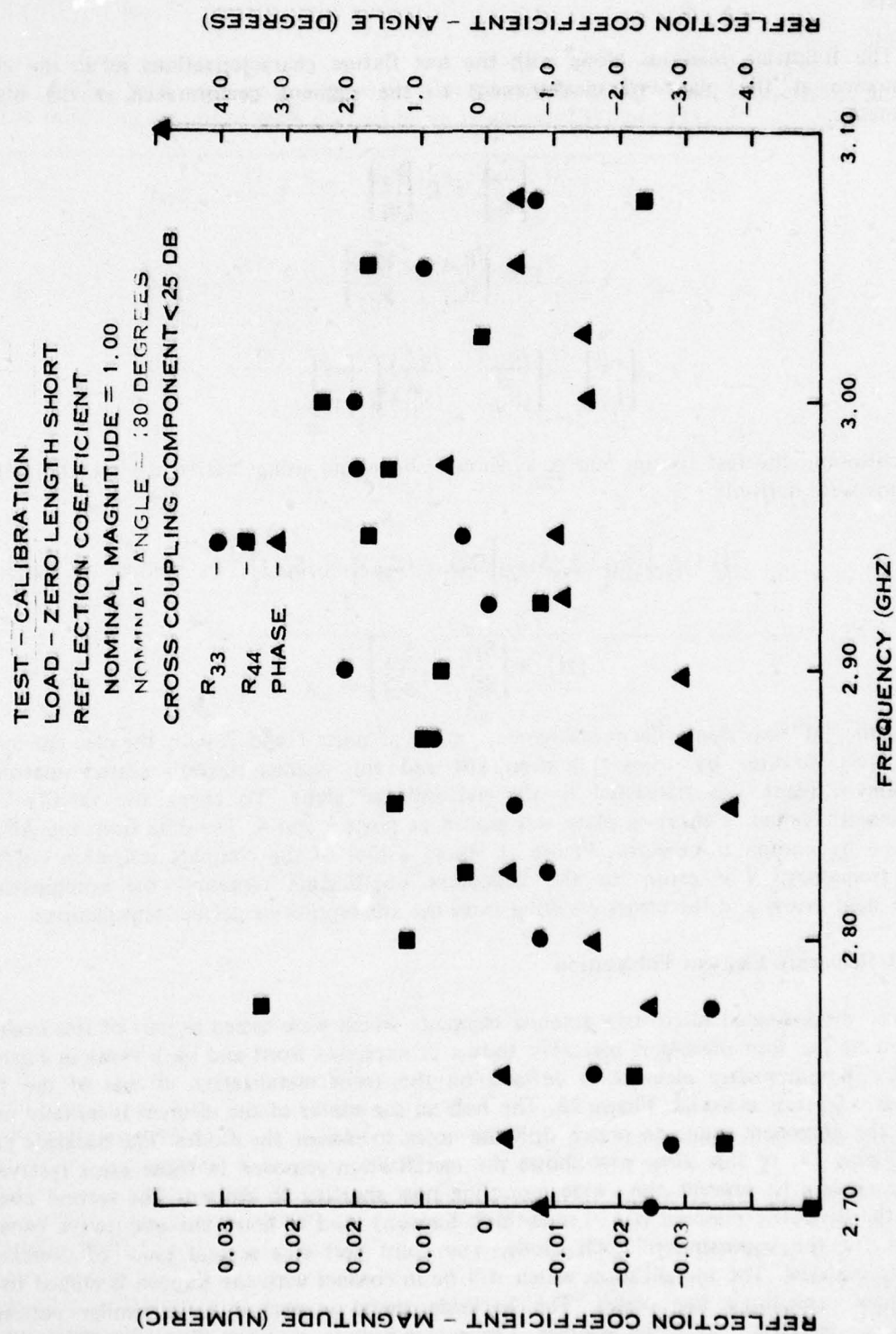$$[\Gamma] = \left[(S_{11}) + (S_{10}) \left[(M) - (S_{00}) \right]^{-1} (S_{01}) \right]^{-1} \tag{56}$$

where

$$[M] = \begin{bmatrix} S_{11}' & S_{12}' \\ S_{21}' & S_{22}' \end{bmatrix} \tag{57}$$

The matrix "M" represents the measurements made at ports 1 and 2 with the element installed in the test fixture. By using Equation (56) and the characterization scatter matrix, the measurement plane was translated to the performance plane. To check the validity of the measurement system, a shorting plate was placed at ports 3 and 4. The data from the ANA was translated by computer program. Figure 21 shows a plot of the complex reflection coefficient versus frequency. The errors in the reflection coefficients represent the combination of measurement errors and the errors resulting from the assumption of perfect terminations.

4. Reflectarray Element Fabrication

The diode-loaded microstrip antenna elements which were tested as part of this evaluation consisted of the four piece-part assembly shown in exploded front and back views in Figures 22 and 23. The microstrip element is defined on the front metalization of one of the Teflon fiberglass 0.06-inch material, Figure 22. The hole in the center of the element is initially used as part of the alignment guide to match drill the holes to mount the diodes. The backside ground plane, Figure 23, of this piece part shows the metalization removed in those areas reserved for diode mounting to prevent the diode mounting post shorting to ground. The second assembly part is the dielectric material (0.001-inch-thick Kapton) used to form the microwave capacitors required for the bypassing of each diode. The third part is a second piece of double-sided dielectric material. The metalization which will be in contact with the Kapton is etched to form the bypass capacitor's top plates. The backside metal is etched to a similar pattern for convenience and serve as a bias contact. The center hole is used for alignment. The remaining

REFLECTION COEFFICIENT — ANGLE (DEGREES)

TEST — CALIBRATION
LOAD — ZERO LENGTH SHORT
REFLECTION COEFFICIENT
NOMINAL MAGNITUDE = 1.00
NOMINAL ANGLE = 180 DEGREES
CROSS COUPLING COMPONENT < 25 DB

R₃₃ —
R₄₄ —
PHASE —

FREQUENCY (GHZ)

REFLECTION COEFFICIENT — MAGNITUDE (NUMERIC)

208934

Figure 21. Reflectarray Antenna Element Test Fixture

34
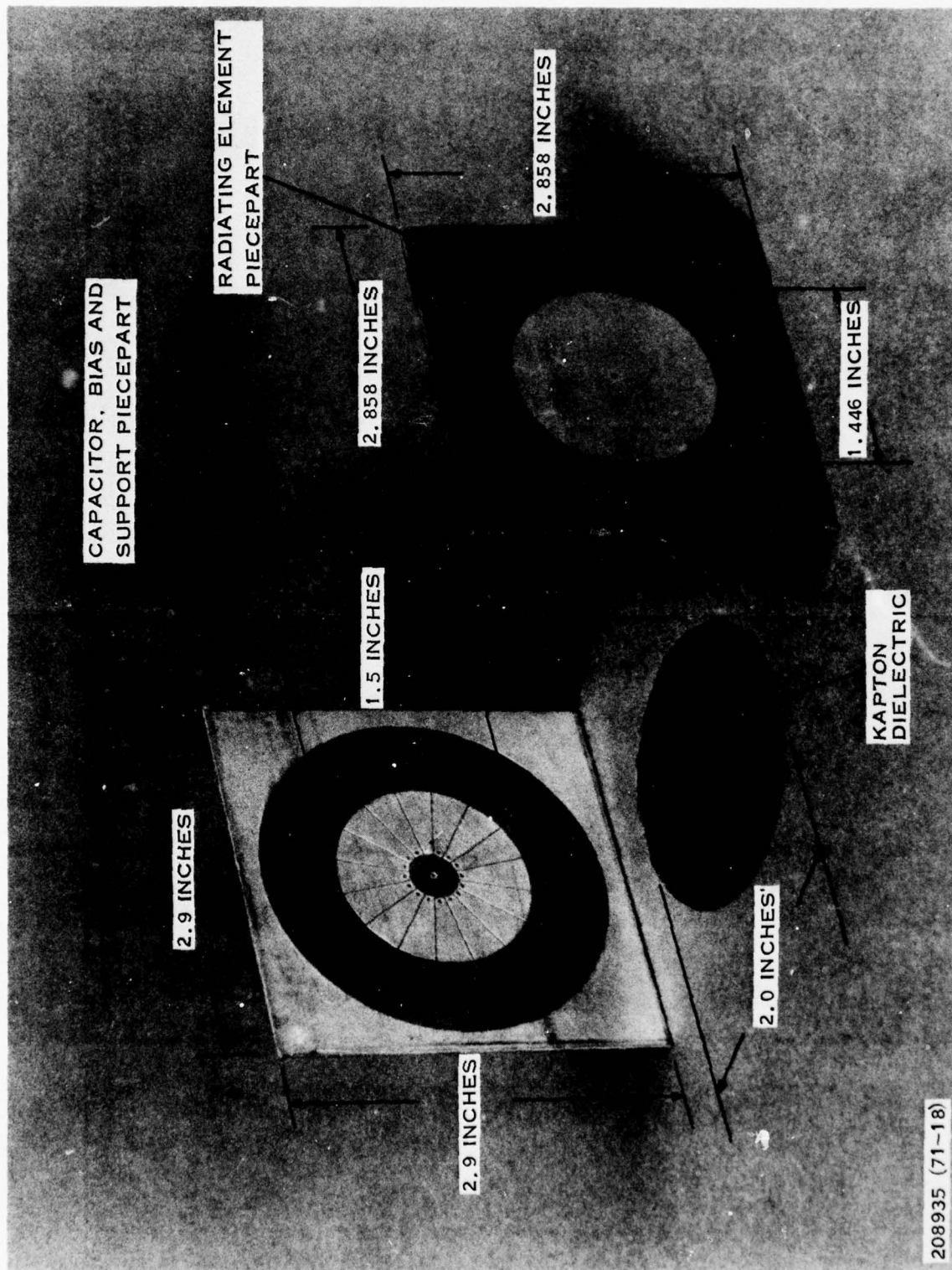
Figure 22. Reflectarray Microstrip Element Exploded View—Front Side

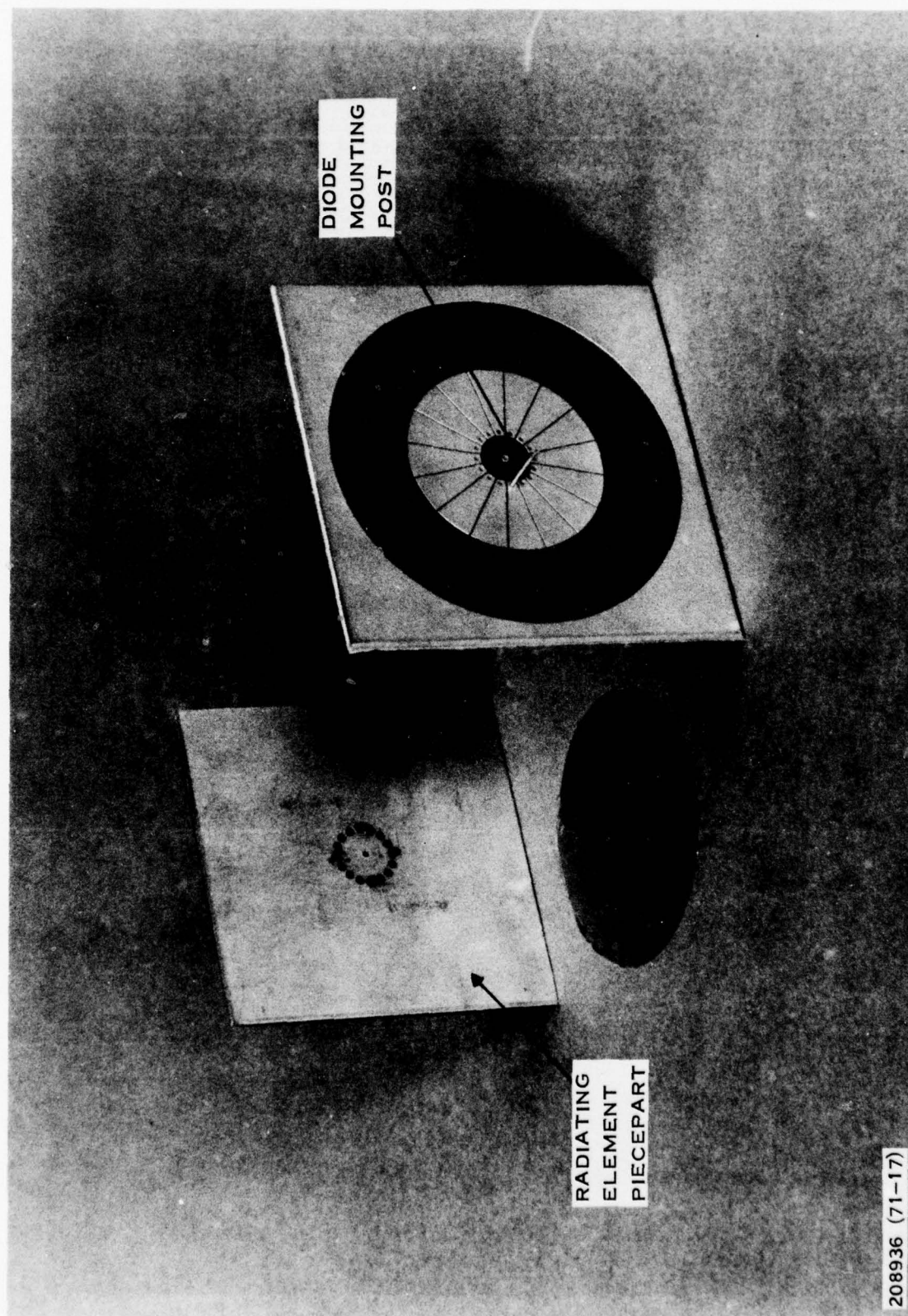CAPACITOR, BIAS AND SUPPORT PIECEPART

RADIATING ELEMENT PIECEPART

2.858 INCHES

2.858 INCHES

1.446 INCHES

1.5 INCHES

2.9 INCHES

2.9 INCHES

2.0 INCHES

KAPTON DIELECTRIC

208935 (71-18)

35

DIODE MOUNTING POST

RADIATING ELEMENT PIECEPART

Figure 23. Reflectarray Microstrip Element Exploded View—Back Side

208936 (71–17)

36

FLYING LEAD – GOLD RIBBON
(0.0005 BY 0.005 NOMINAL)

DIODE CHIP (TI–MD871)
0.015 BY 0.015 (MAX)

0.2 (MIN)

0.5 (MIN)

GOLD PLATED BRASS ROD
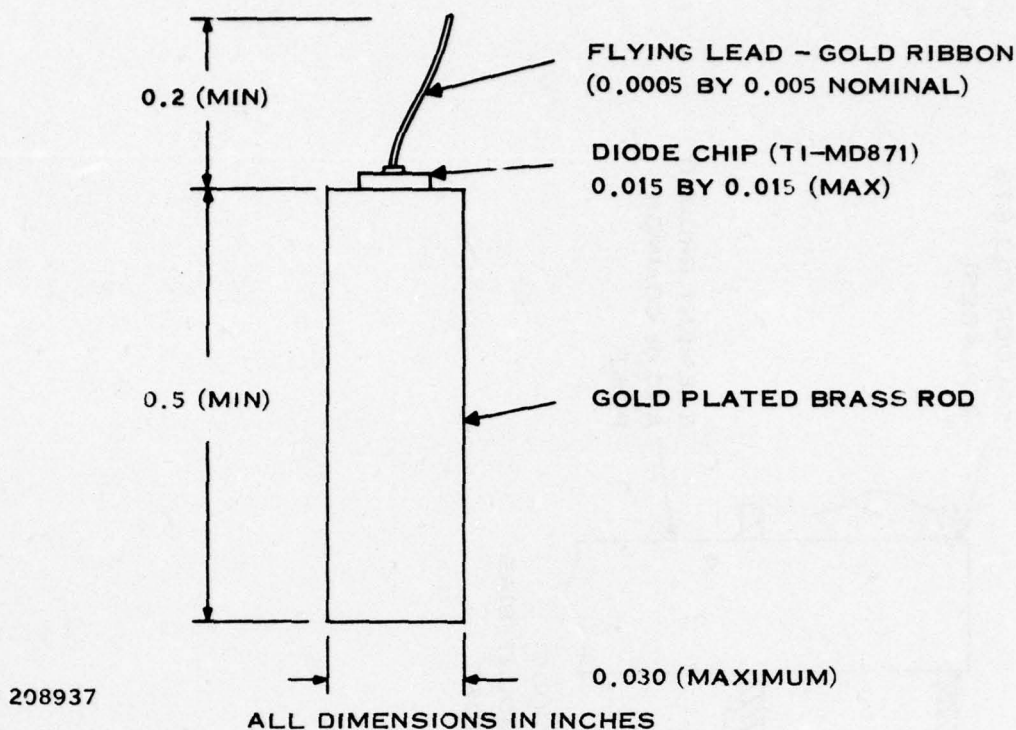
0.030 (MAXIMUM)

208937

ALL DIMENSIONS IN INCHES

Figure 24. Reflectarray Diode Assembly

holes are plated-through to allow contact between the diode mounting post, the capacitor top plate, and the bias pad. The fourth piece part is the diode subassembly which consists of the diode (TI-MD871), the diode mount/bias post, and the "flying lead" contacting the top diode metalization. This subassembly was a purchased part. The diode's reversed biased capacitance was less than 0.15 pF and its series resistance is less than 2 ohms. A drawing, Figure 24, shows further description.

The etch patterns were defined using standard photolithographic techniques. This process was necessary due to the tight tolerancing and close metalization/component spacing. The element shown in Figures 22 and 23 allows up to 16 diodes to be positioned at 22.5 degrees spacing, 0.215 inch from the element's center. Other elements were fabricated for evaluation which had provisions for two, four, or eight diodes.

The assembly procedure in all cases first consisted of placing the two etched boards together and properly aligning using the center guide hole. The diode mounting holes were then matched drilled through both pieces using an 0.031-inch drill. After hole deburring and cleaning, these pieces were soldered together along their outer edge with the Kapton dielectric sandwiched in the center. Alignment pins were used during this step to ensure that all parts were in their proper place. The diode subassembly was then inserted in the previously drilled holes, puncturing the Kapton in the process to a position where the diode was approximately 0.020 inch from the element's surfaces. The diode mounting post was then soldered to the plated-through hole metalization and the diode's flying lead was bonded to the top metal. Figure 25 shows a cross-sectional view of the diode mounting. The final assembly step was to expose the element's ground plane near the center from the back so that the element could be ground at this point and a wire attached to serve as the common lead for dc biasing the diodes.

37
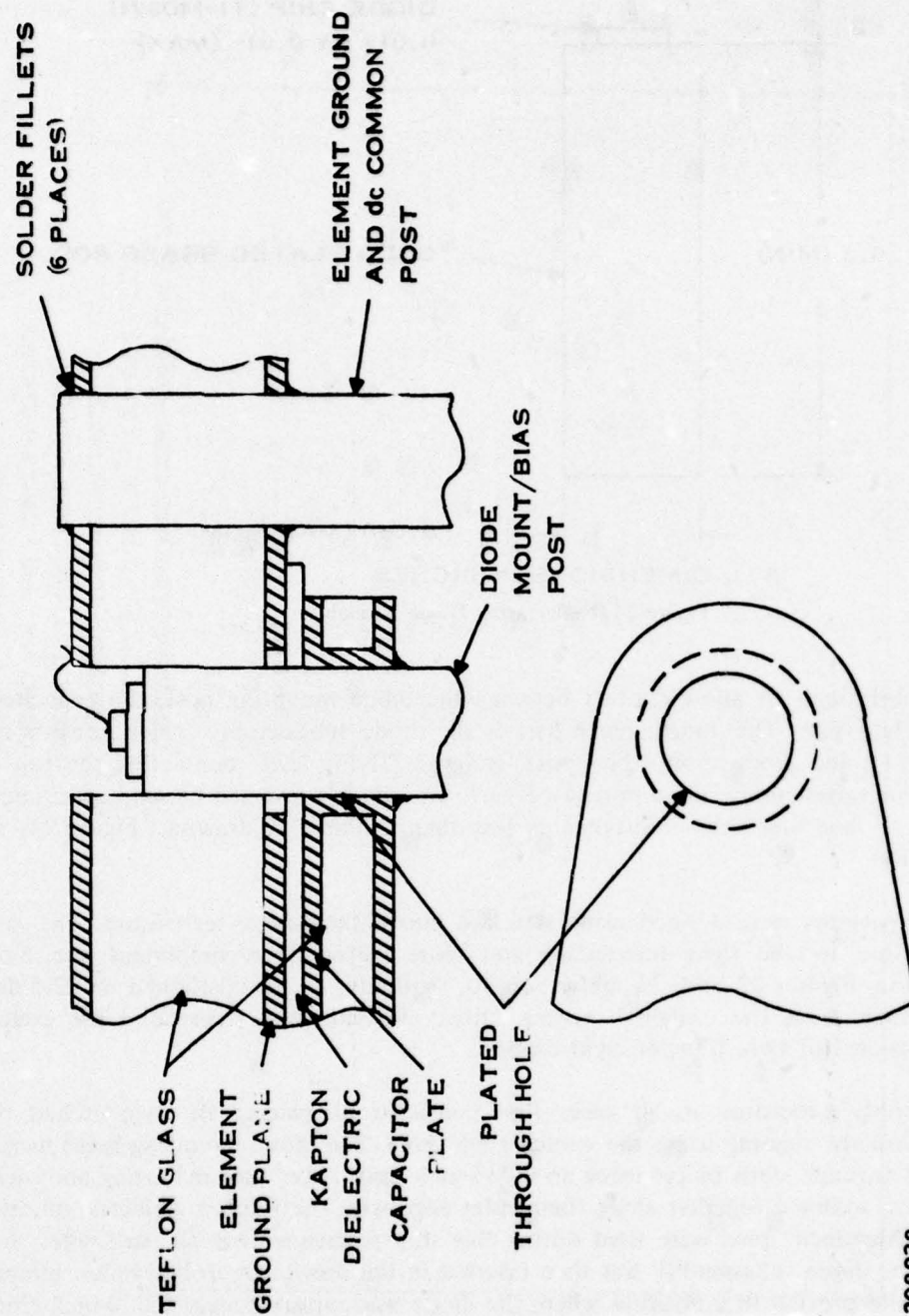
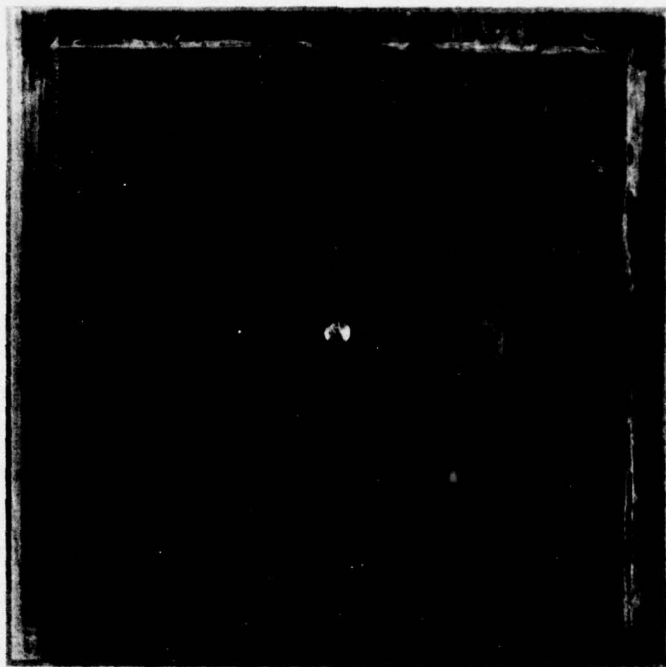**Figure 25. Diode Mount/Bypass Configuration**

208938

208939 (71–20)

Figure 26. Reflectarray Microstrip Element: 16 Diodes—Front View

The completed assembly is shown in Figures 26 and 27. The back board is made larger so that its metalization which is soldered to the element's ground plane can provide the necessary grounding to the test fixture's waveguide flange. The diodes can be independently biased by connecting a dc supply between the common lead and any given diode mounting post.

5. Measured Results

The results of the primary microstrip antenna evaluation are presented in this subsection to demonstrate its performance with diode loading. All performance is referenced to the element's front surface. The design and fabrication of all elements to be described is exactly the same, the only difference is the number of loading diodes.

The first performance presented is the 4-diode element, Figure 28. Figures 29, 30, and 31 show R33, R44 and the cross-coupling parameter R34/R43 as a function of frequency near resonance. The forward/reverse bias diode state is described by 1010 (plane 44′ diodes on, plane 33′ diodes off) and 0101 (plane 33′ diodes on, plane 44′ diodes off). In the plane of the forward biased diodes, the magnitude and phase of the element's reflection coefficient (i.e., R44 in Figure 29 and R33 in Figure 30) are seen insensitive to frequency. On the other hand, in the plane of the reverse biased diodes, the reflection coefficient is seen to vary in a manner similar to the element without diode loading. The difference in performance for the two diode states can be seen more clearly when the data from Figures 29 and 30 is plotted as shown in Figure 32. R44 (1010) and R33 (0101) data points are so close together only the lowest and highest frequency points are plotted. Also plotted are the calculated forward and reverse bias diode

39
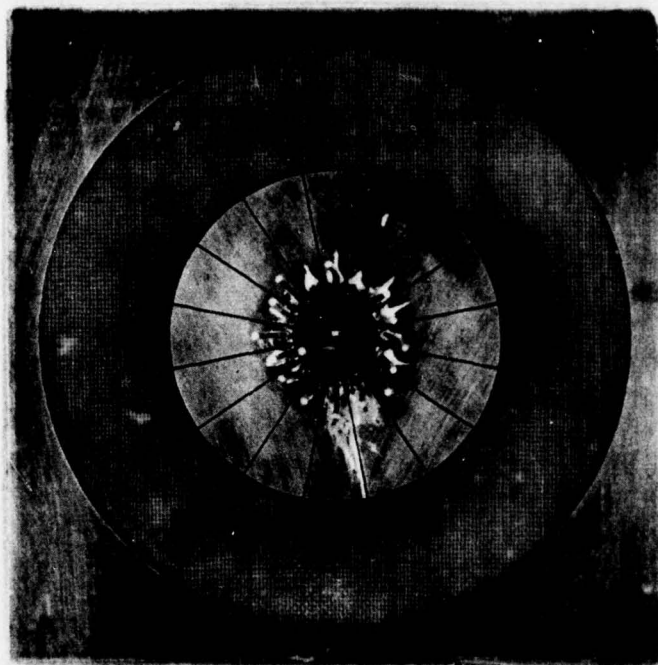
208940 (71-21)

Figure 27. Reflectarray Microstrip Elements: 16 Diodes—Back View

PORT 3

PORT 4'   PORT 4

PORT 3'
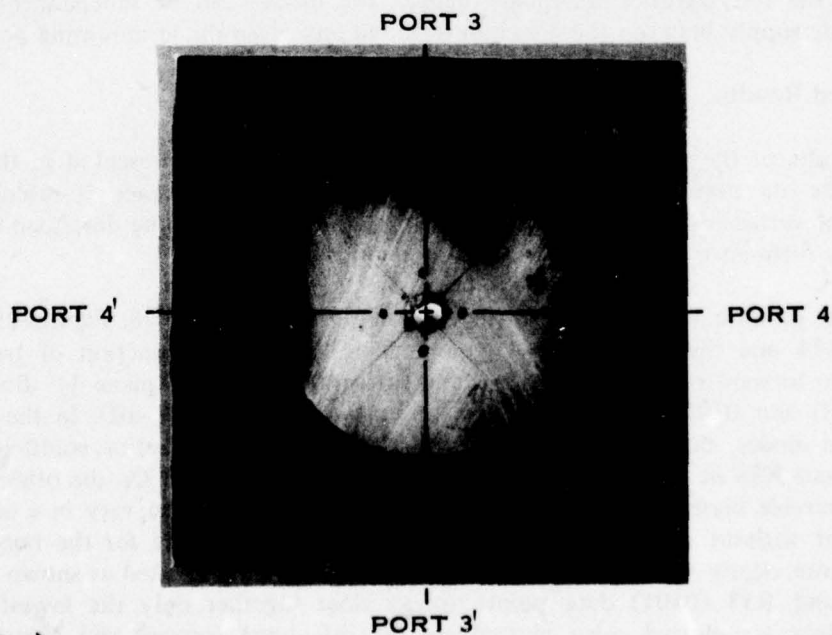
208941 (71-4)

Figure 28. Reflectarray Microstrip Antenna: 4 Diodes/90-Degree Spacing

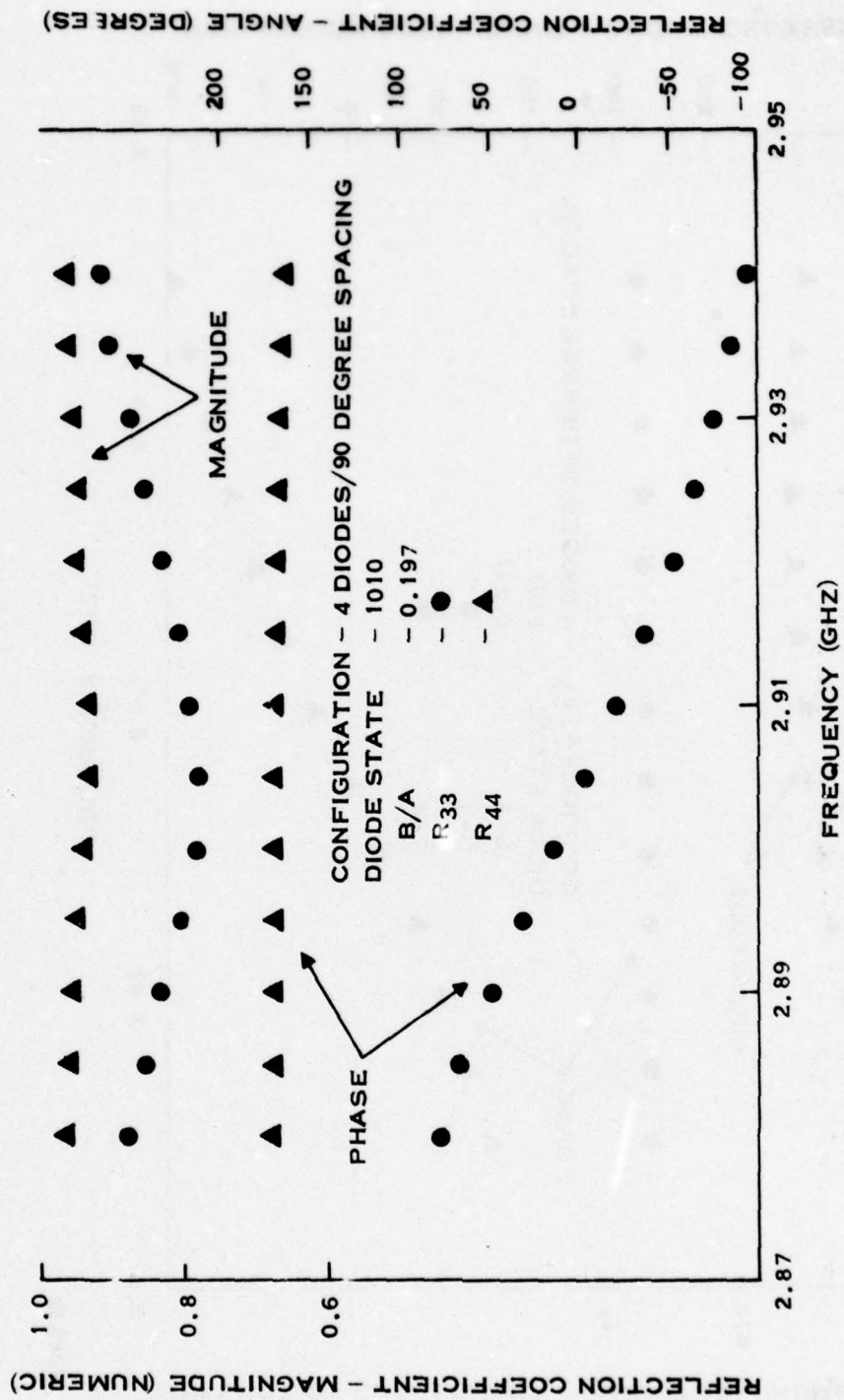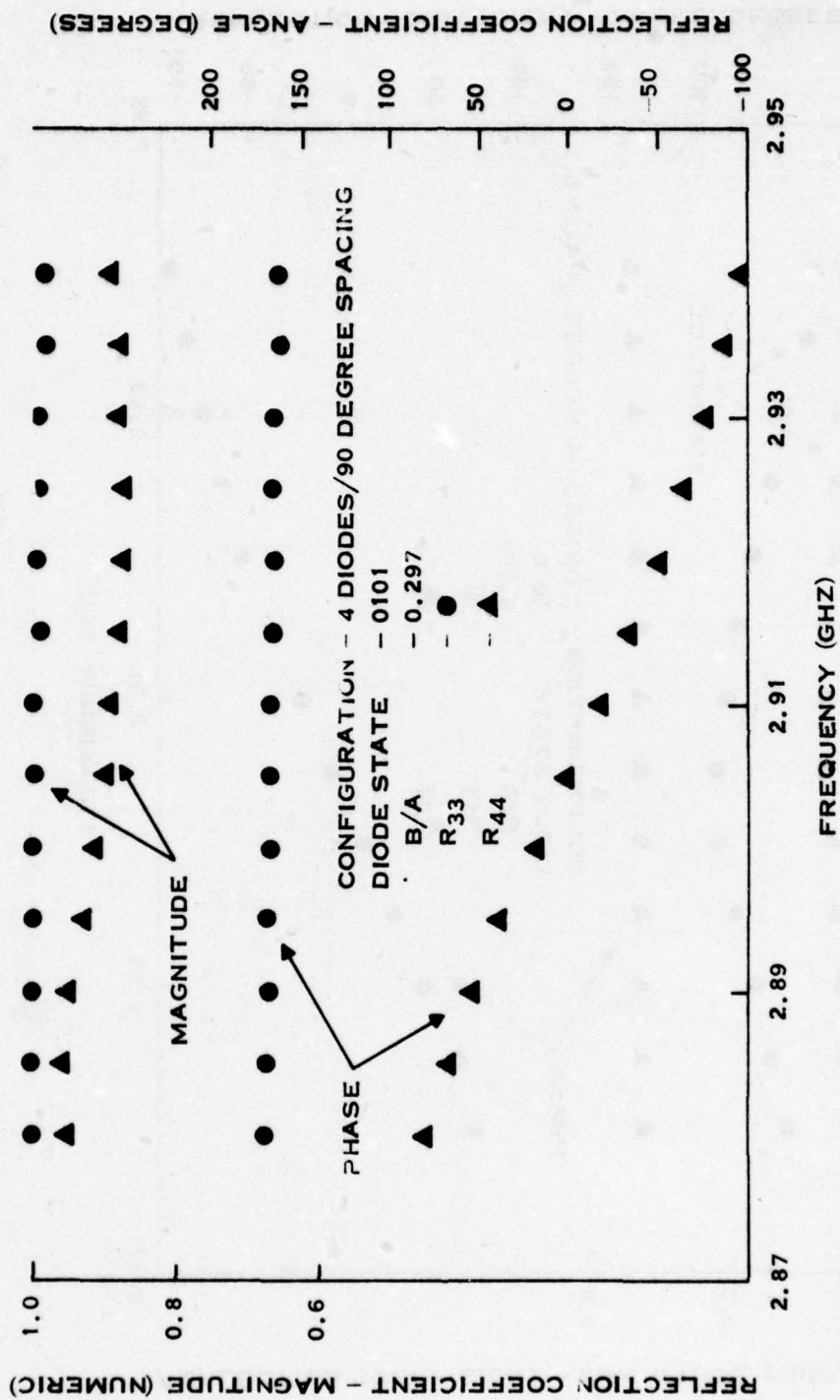Figure 29. Reflectarray Microstrip Antenna Element Performance
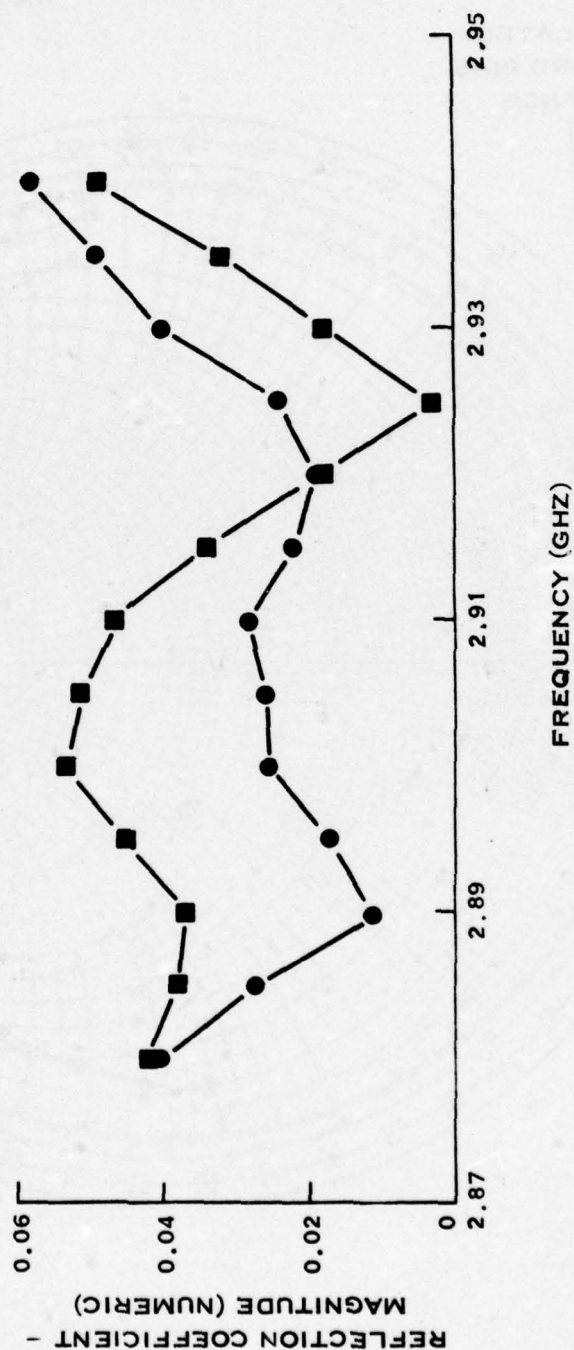
208942

41

Figure 30. Reflectarray Microstrip Antenna Element Performance

208943

42

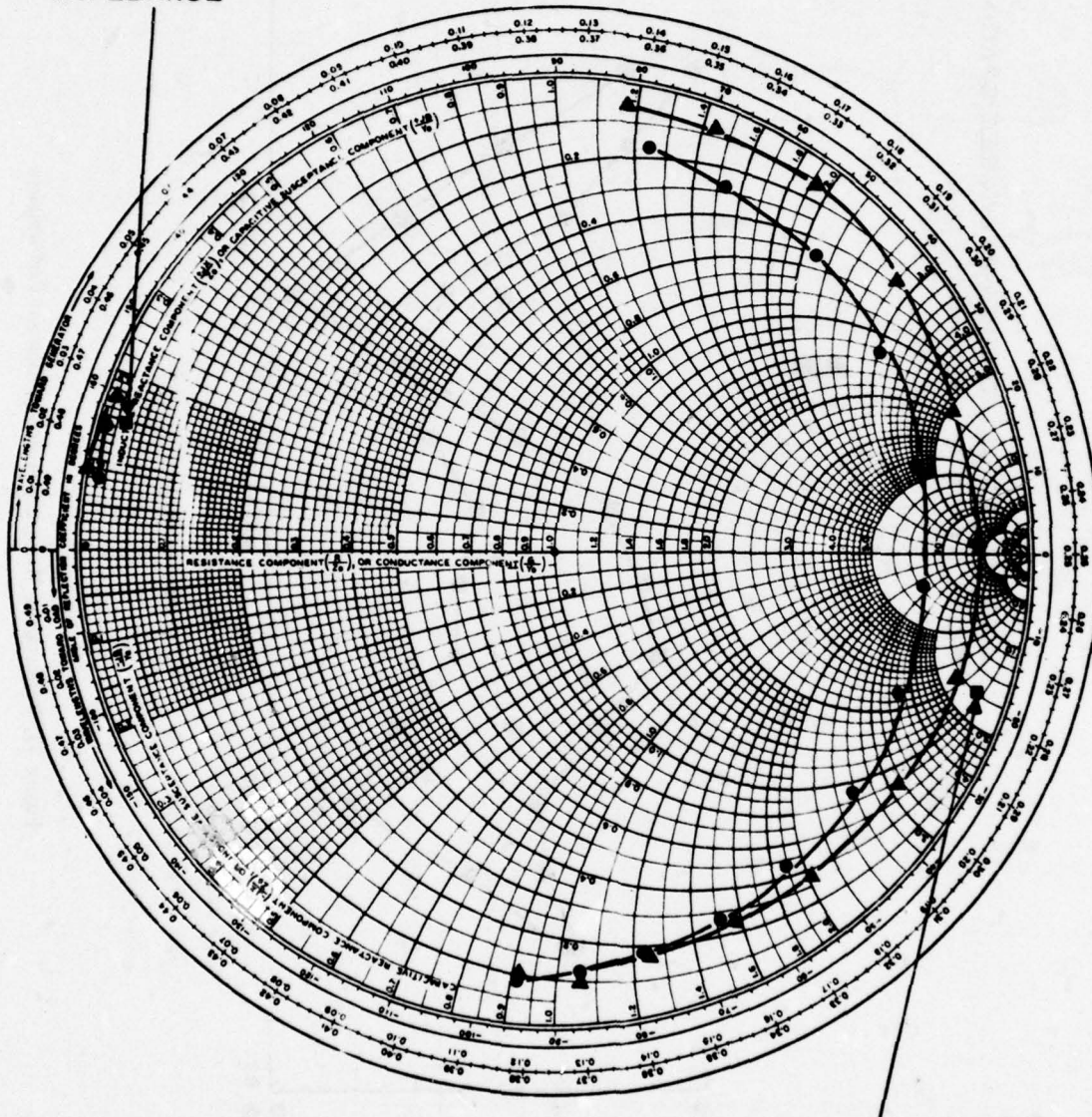Figure 31. Reflectarray Microstrip Antenna Element Performance

43

CONFIGURATION – 4 DIODES
                     WITH 90
                     DEGREE
                     SPACING
DIODE STATE   – 1010/0101

CALCULATED
FORWARD BIAS
IMPEDANCE

CALCULATED
REVERSE BIAS
DIODE IMPEDANCE

208945

Figure 32. Reflectarray Microstrip Antenna Element Performance

44

impedance. Good agreement exists between the frequency at which the element has its best performance and the frequency at which the diode's reflection coefficient has a 180-degree phase differential.

Figure 31 shows the element's cross-coupling performance for the two diode states.

Figures 33 and 34 show the effect on the reflection coefficient in the plane of the forward-biased diodes between both diodes on, or one on and one off.

Assuming the legitimacy of combining the elements reflection coefficients into a resultant reflected E-field vector, by simple vector addition, element performance can be expressed in phase shifter parameters. For example, Figure 35 presents the differential phase error between diode states and Figure 36 shows the resultant E-field amplitude for the same diode states. The reflection loss in the vicinity of 2.91 GHz is approximately 1.6 ±0.3 dB.

Figure 37 shows a 3-bit phase shift realization using eight diodes. The diodes are spaced at 22.5 degrees. The numbers by the diodes indicate the phase state with state 1 being used as the reference. Figures 38 through 49 present the element's performance for each phase state.

Figures 38 and 39 show R33 and R44 plotted versus frequency about the element's center frequency for diode one or five forward-biased. Figure 40 shows the same data plotted on a Smith chart. Figure 41 shows the cross-coupling performance for diodes states 1 and 5. Also shown is the state where all diodes are reverse-biased. Figures 42 through 47 show R33 and R44 performance for diode states 2, 3, 4, 6, 7 and 8. Figures 48 and 49 are plots showing the 8-diode element similar to the 4-diode performance of Figures 35 and 36.

C. ANALYSIS

The variation of the parameters shown in figure 17 can be related to the relationship between the disk fringing capacitance and its capacitance with the fringing capacitance ignored (direct capacitance). This ratio is directly proportional to the d/a ratio. For example, as d/a increases, the percentage of the fringing is increased relative to the direct capacitance. If the capacitance ratio is near zero, equivalent to d/a approaching zero, the cavity which is assumed formed by the upper and lower conducting surfaces would have a diameter equal to the disk diameter. For nonzero capacitance ratios, the element can be viewed as a cavity with an effective radius greater than the actual disk radius. Therefore, the difference between the measured and the calculated resonant frequency approaches zero as d/a approaches zero.

For a fixed coaxial port position, the b/a ratio varies inversely as d/a with a corresponding decrease in the measured driving resistance. The element bandwidth can be viewed as determined by the loading of the generator impedance at the coax input and the loading effect of free space (i.e., the disk radiation efficiency). At small d/a or, equivalently, d/λ_o ratios, radiation approaches zero, the generator loadings approach a constant, allowing the bandwidth to become a constant. As d/a increases, the bandwidth should increase. The parameter variation over the indicated d/a range shows these trends.

The bandwidth improvement evaluation produced no noticeable bandwidth increase for the chosen element topographics. The criterion for this evaluation was the coaxial port reflection coefficient versus frequency.
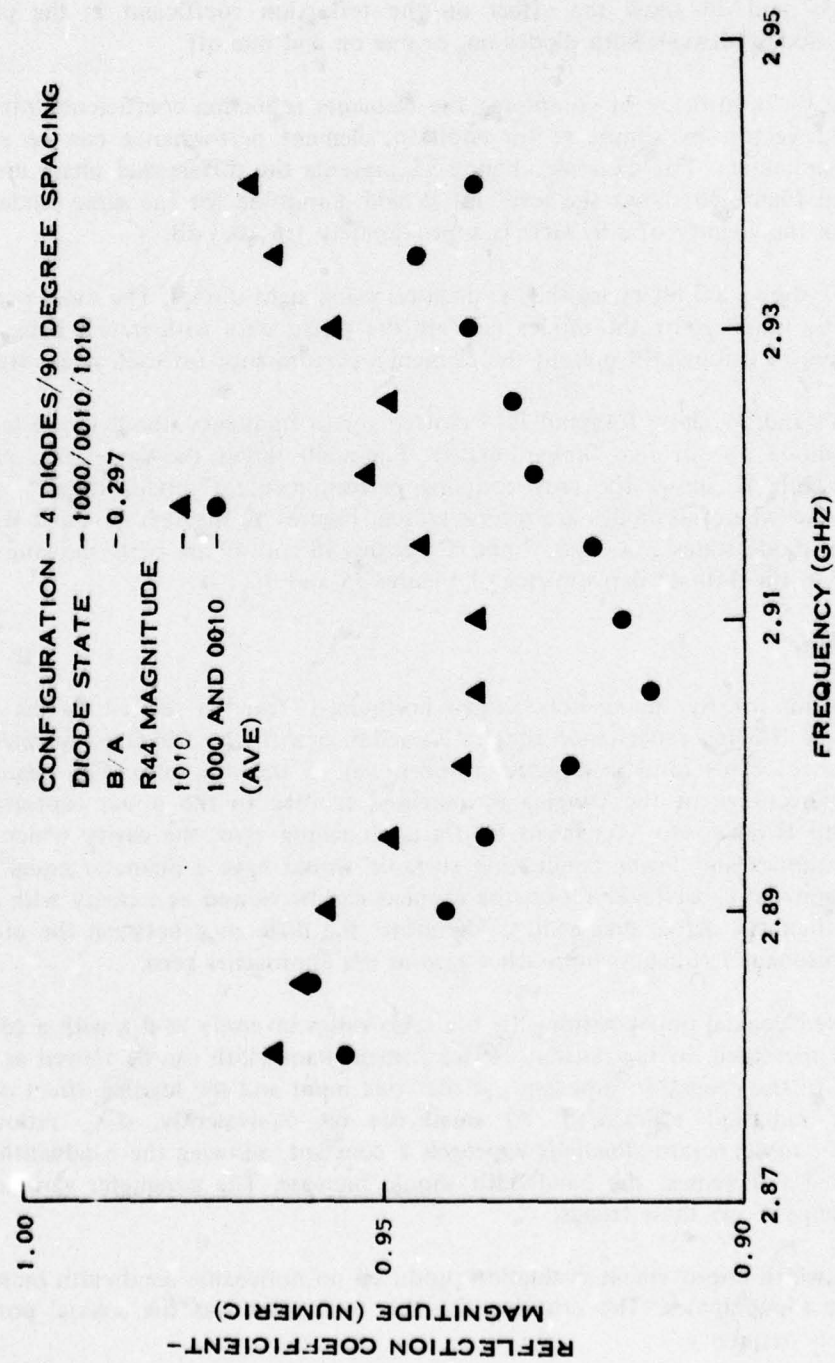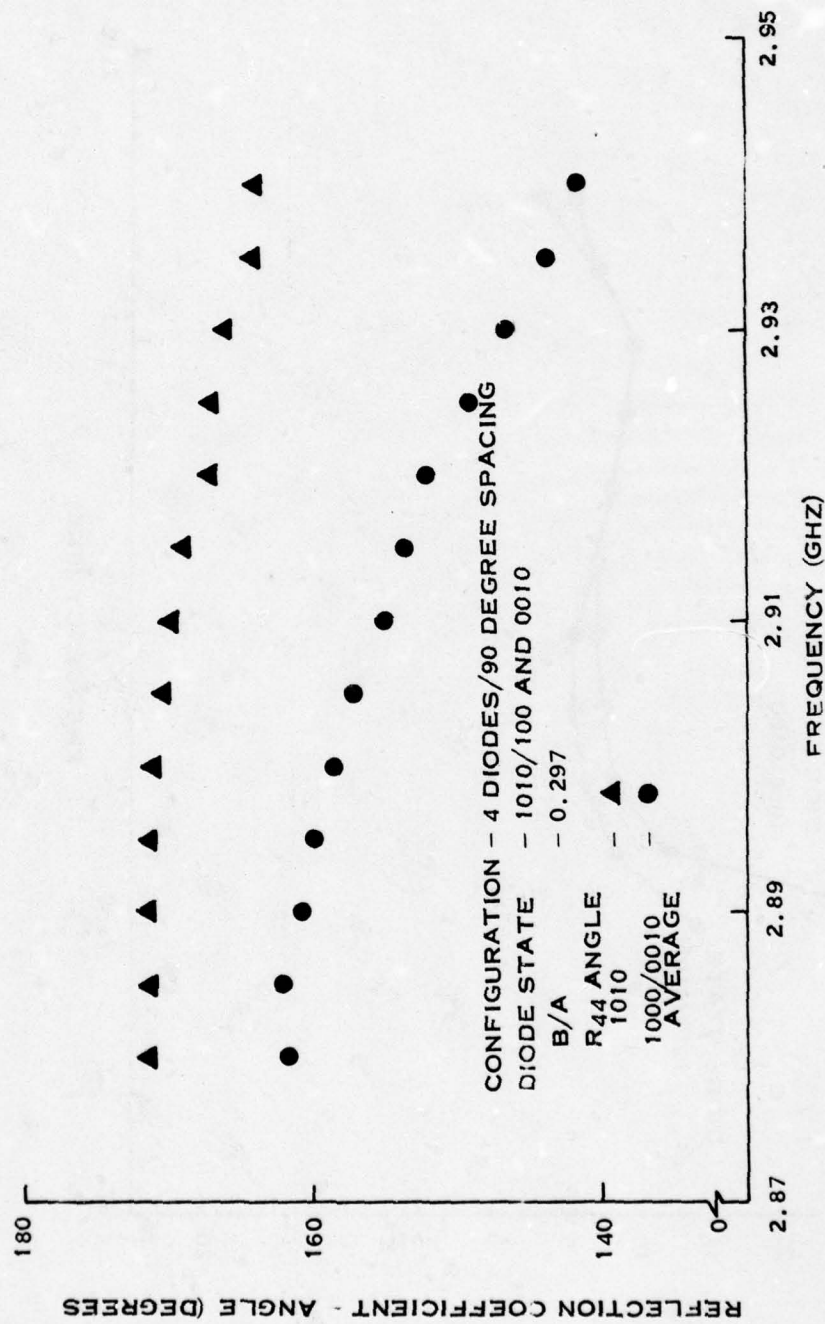
45

Figure 33. Reflectarray Microstrip Antenna Element Performance

46

208946

Figure 34. Reflectarray Microstrip Antenna Element Performance
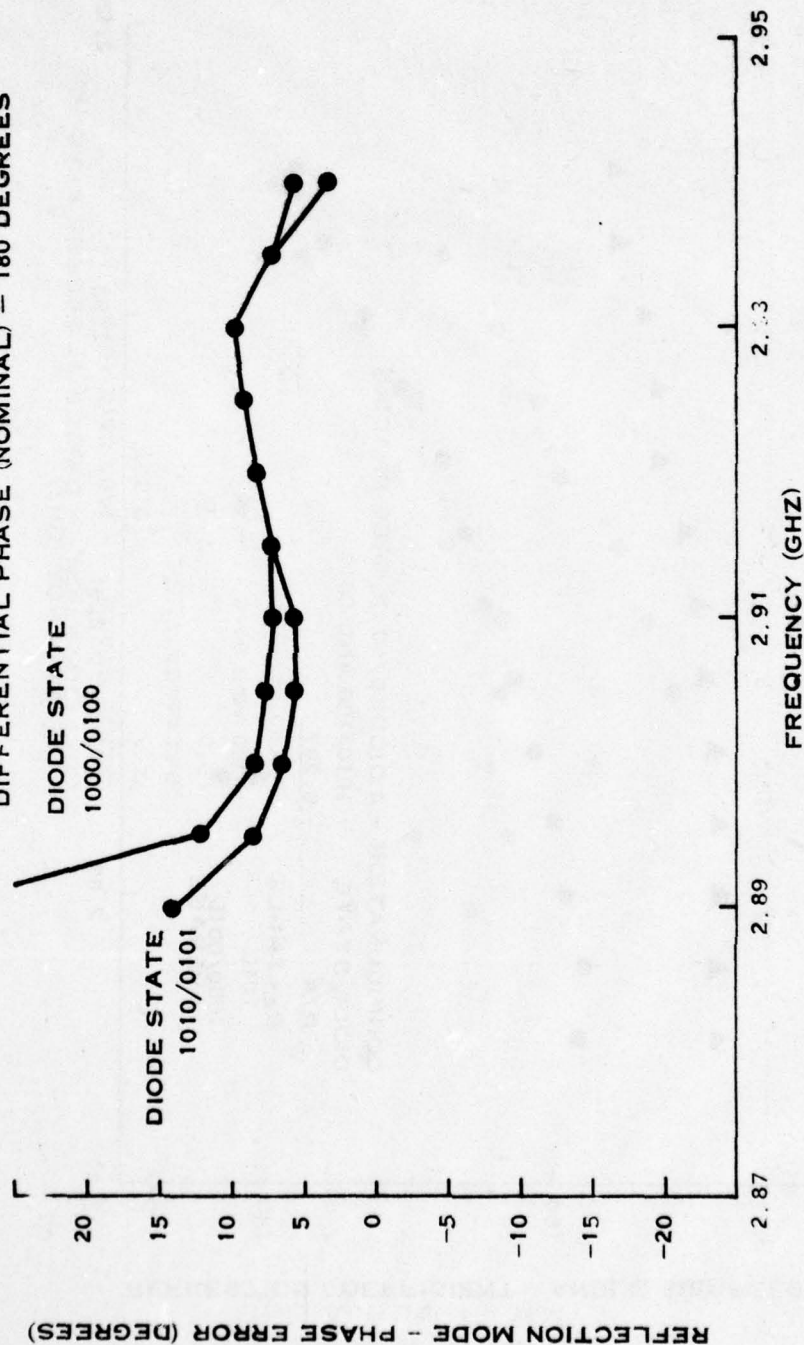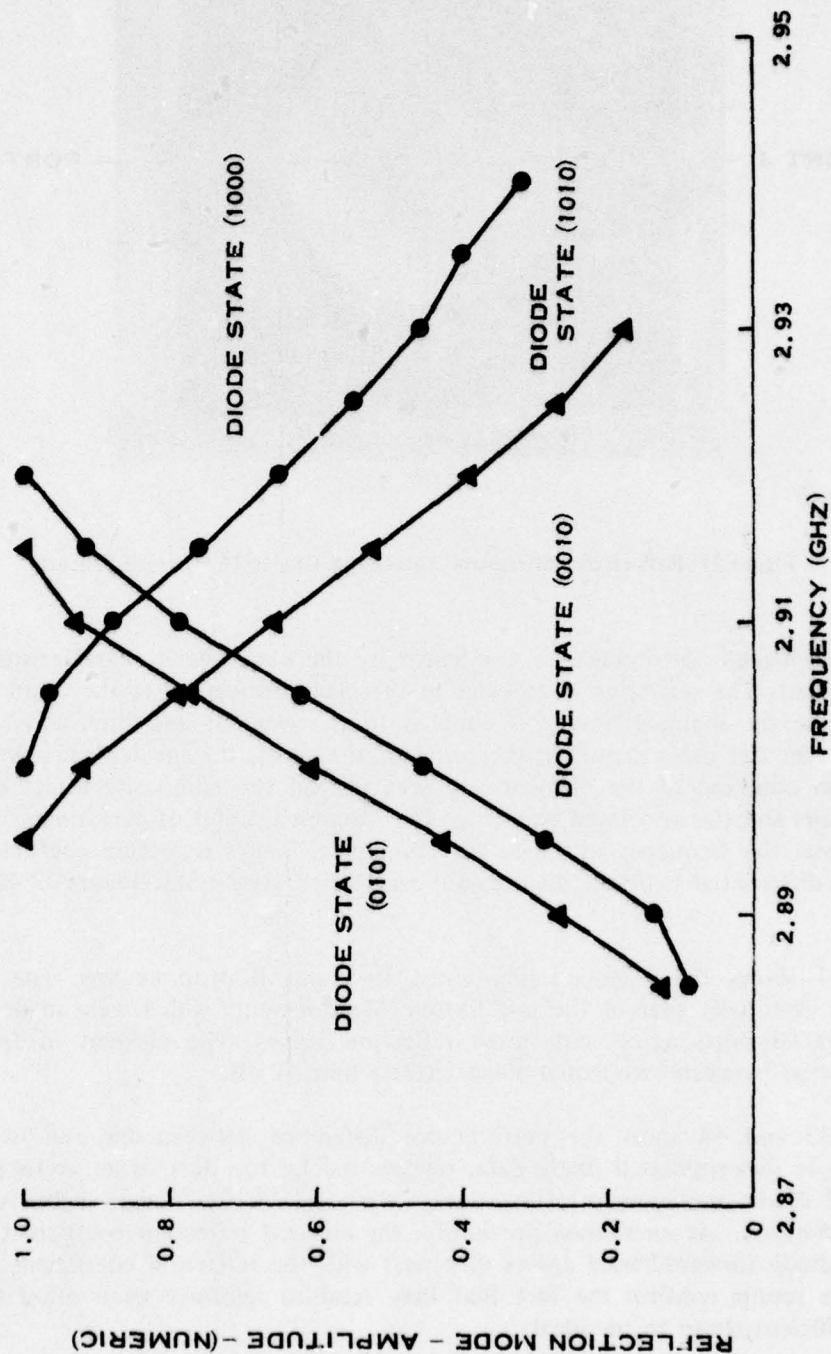
208947

47

Figure 35. Reflectarray Microstrip Antenna Element Performance

208948

48

CONFIGURATION – 4 DIODES/90 DEGREE SPACING

DIODE STATE – 1010/0101/1000/0010

DIODE STATE (1000)

DIODE STATE (1010)

DIODE STATE (0010)

DIODE STATE (0101)

REFLECTION MODE – AMPLITUDE –(NUMERIC)

FREQUENCY (GHZ)

Figure 36. Reflectarray Microstrip Antenna Element Performance

208949

49

PORT 3

PORT 4' — — PORT 4

PORT 3'
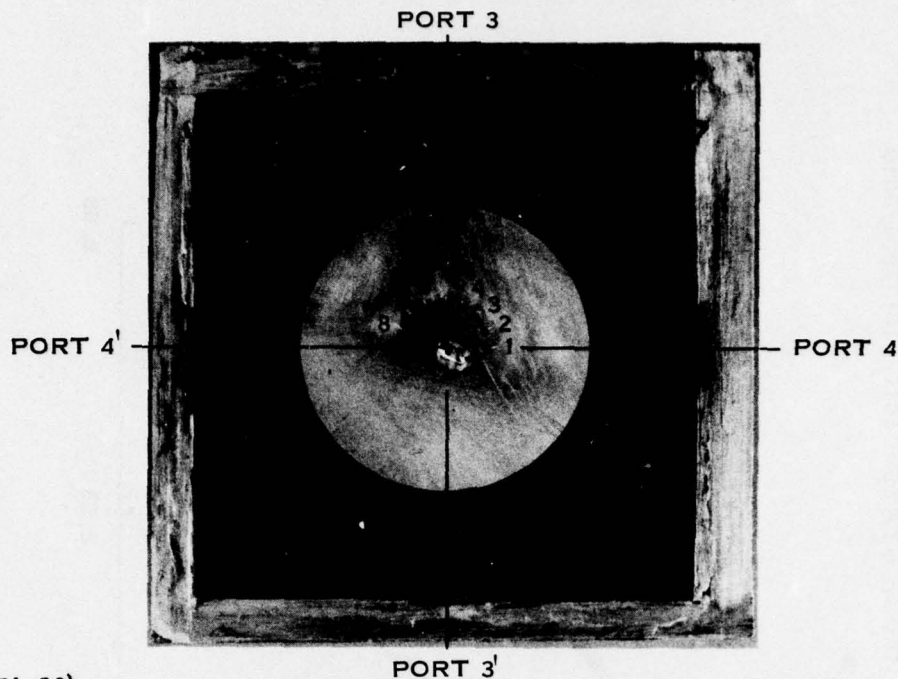
208950 (71–20)

Figure 37. Reflectarray Microstrip Antenna: 8 Diodes/22.5-Degree Spacing

The diode-loaded performance is dominated by the narrowband characteristic of the basic microstrip element. The reflection coefficient in the plane orthogonal to the shorted plane has a variation because the incident energy is coupled to the element and then acted upon by its self-resonance. On the other hand, in the plane of the short, the incident energy is essentially prevented from coupling to the element and sees instead the composite effect of the diode, bypass capacitors and the associated parasitics. The element's center of performance is seen to be located very near the frequency at which the composite diode's reflection coefficient angle has an 180-degree differential between the forward and biased conditions. Figure 32 shows this fact most clearly.

Figure 31 shows the cross-coupling terms R43 and R34 to be low. The characteristic shown here is essentially that of the test fixture. Measurements which were made looking into orthogonal coaxial ports agree with these reflection values. The element in free space has measured isolation between orthogonal planes greater than 40 dB.

Figures 33 and 44 show the performance difference between one and two diodes per plane. The single forward-biased diode data, represented by the dots, is an average value of the two individual diode measurements (i.e., states 1000 and 0010). The triangles represent both diodes forward-biased. As mentioned previously, the element reflection coefficient in the plane with a single diode forward-biased agrees very well with the reflection coefficient of the diode. The two-diode results confirm the fact that they tend to reinforce each other to produce a reflection coefficient closer to the ideal.

50

REFLECTION COEFFICIENT – MAGNITUDE (NUMERIC)

150 100 50 0 -50

CONFIGURATION – 8 DIODES/22.5 DEGREE SPACING

DIODE STATE   B/A
R_{33} $= 0$ $= 0.297$
R_{44} $-$ $-$
                         $-$ $-$

MAGNITUDE

PHASE

1.0   0.8   0.6

2.79   2.81   2.83   2.85

FREQUENCY (GHZ)

Figure 38. Reflectarray Microstrip Antenna: Element Performance

208951

51

CALCULATED
FORWARD BIAS
DIODE IMPEDANCE

CALCULATED
REVERSE BIAS
DIODE IMPEDANCE

208952

Figure 39. Reflectarray Microstrip Antenna: Element Performance

52

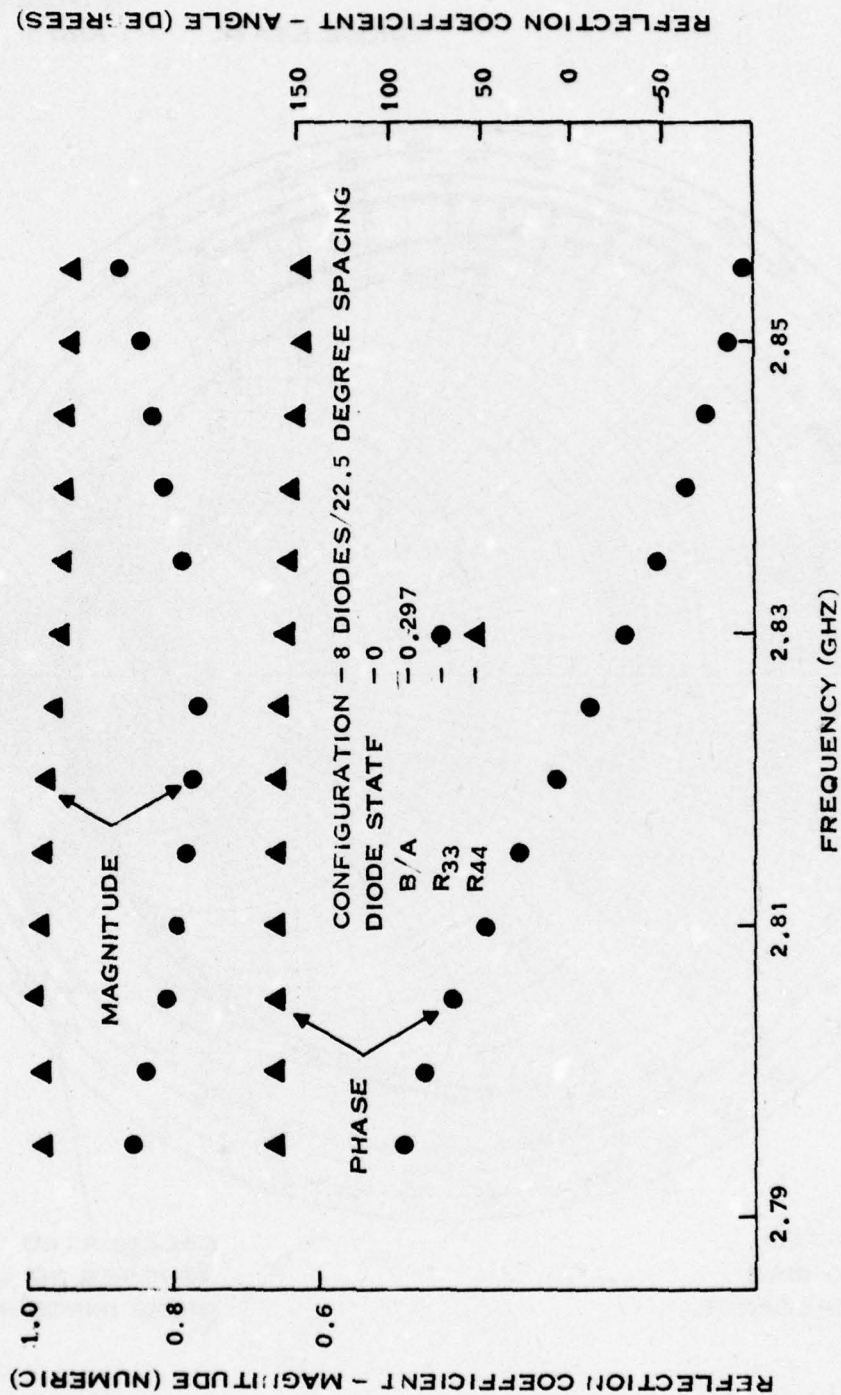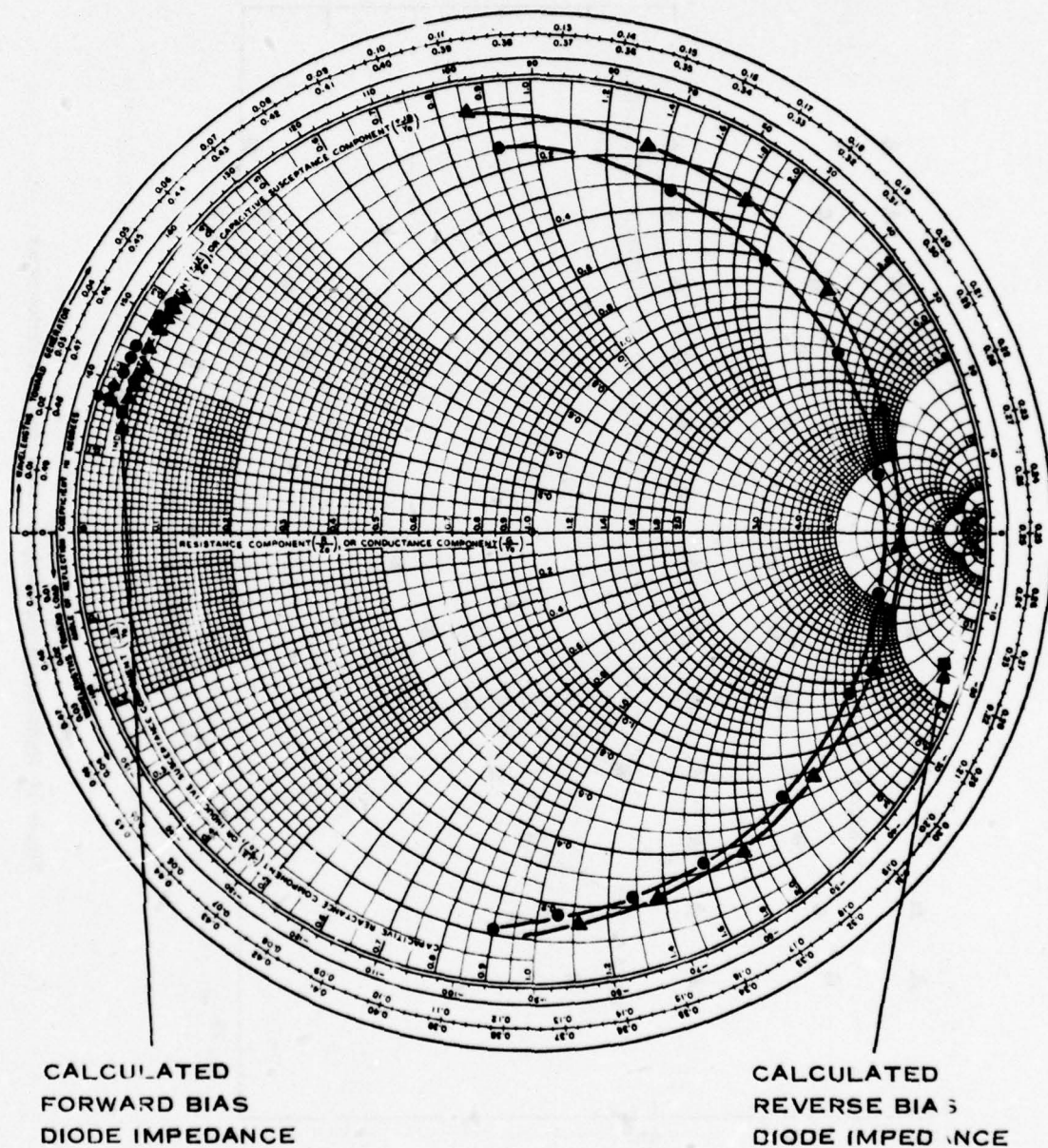Figure 40. Reflectarray Microstrip Antenna: Element Performance

208953

53

Figure 41. Reflectarray Microstrip Antenna Element Performance

CONFIGURATION – 8 DIODE/22.5 DEGREE SPACING
DIODE STATE – 0, 90 DEGREE, REVERSE BIAS
B/A – 0.297
R_{34}/R_{43}

0 DEGREE –
90 DEGREE –
ALL REVERSE BIAS –

REFLECTION COEFFICIENT – MAGNITUDE (NUMERIC)

FREQUENCY (GHz)

0.20
0.15
0.10
0.05
0

2.79
2.81
2.83
2.85

208954

54

CONFIGURATION – 8 DIODES/22.5 DEGREE SPACING

DIODE STATE	– 22.5 DEGREE
B/A	– 0.297 ●
R33	– ●
R44	– ▲
R34 = R43	– ■

FREQUENCY (GHZ)
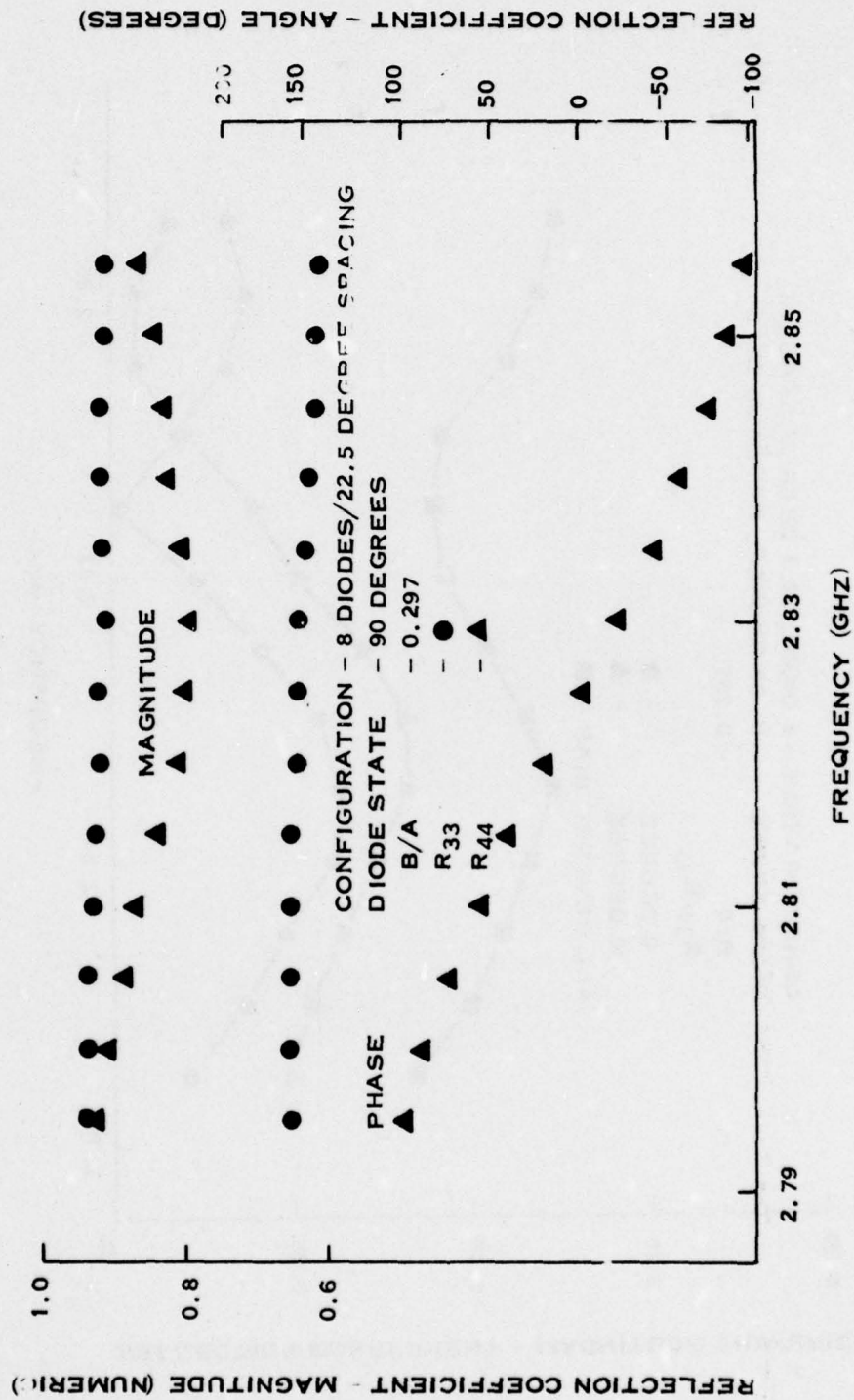
REFLECTION COEFFICIENT – MAGNITUDE (N JMERIC)

Figure 42. Reflectarray Microstrip Antenna Element Performance

208955

55
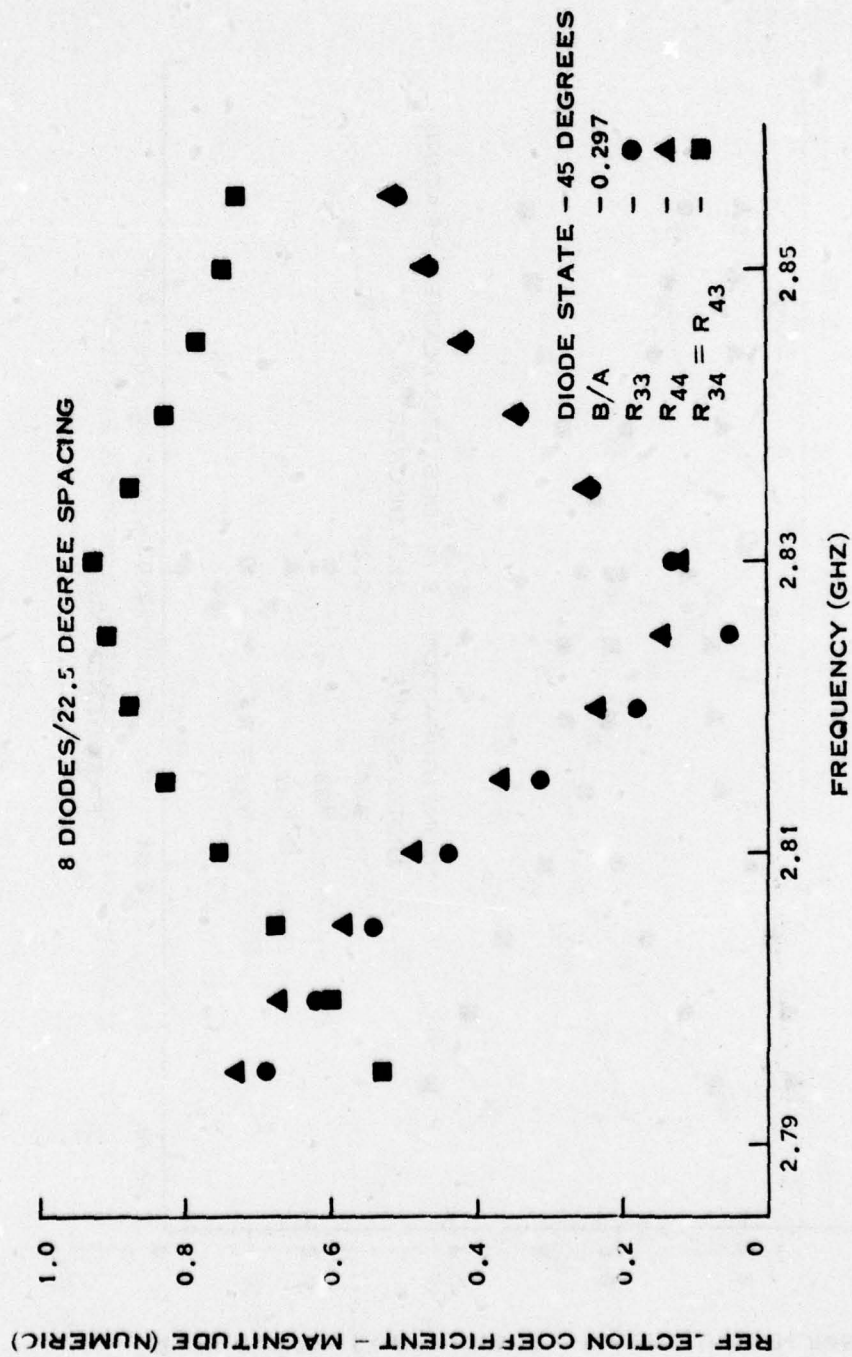
Figure 43. Reflectarray Microstrip Antenna Element Performance

208956

56

Figure 44. Reflectarray Microstrip Antenna Element Performance
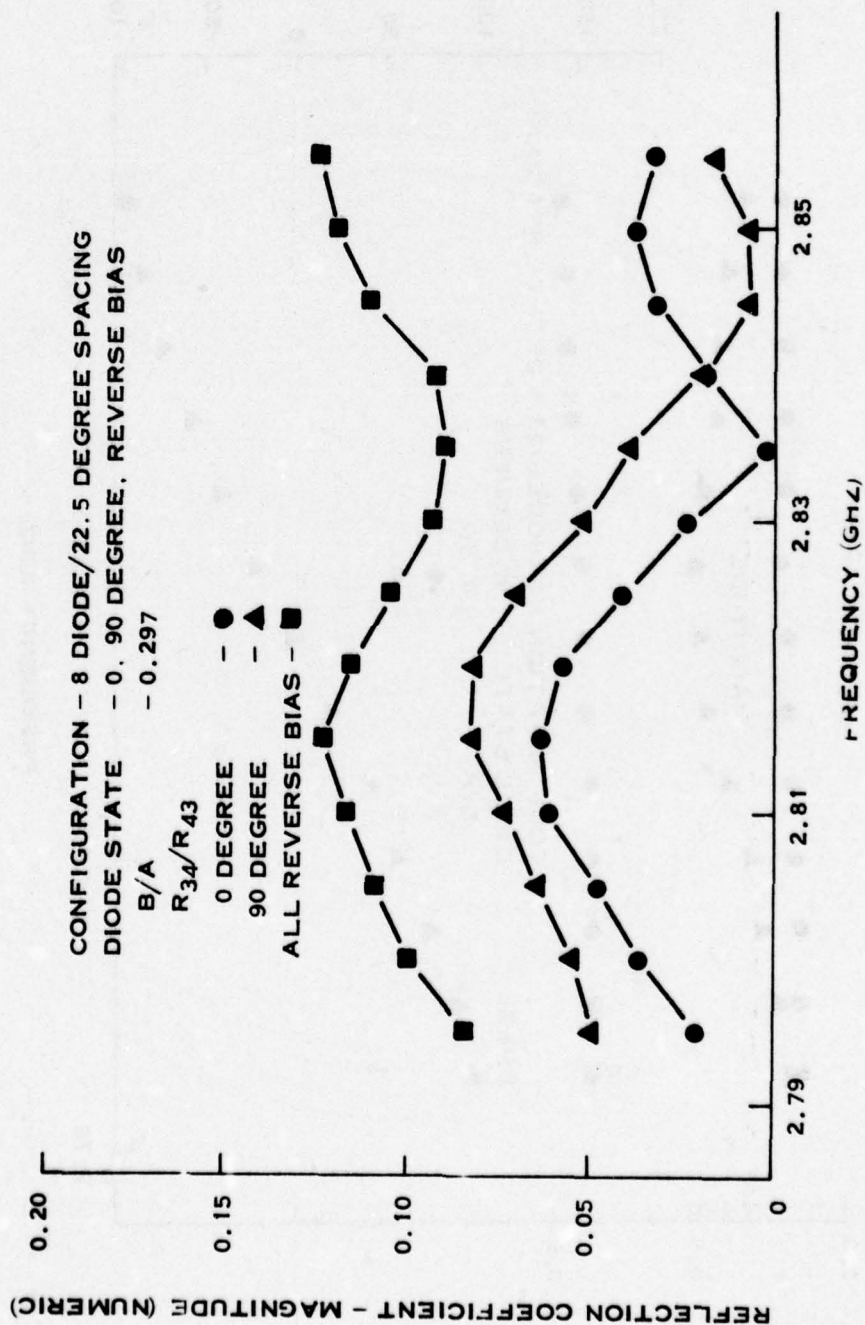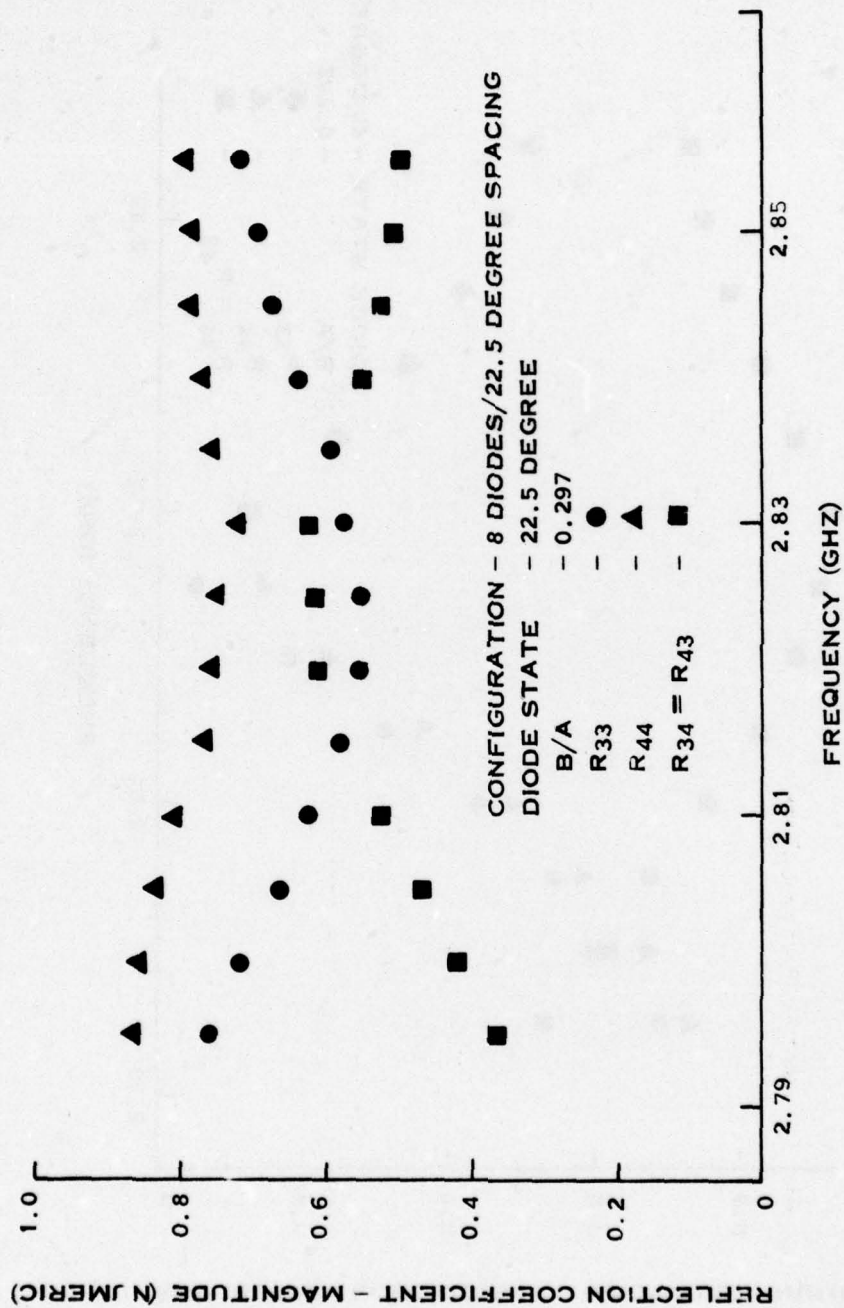
208957

57
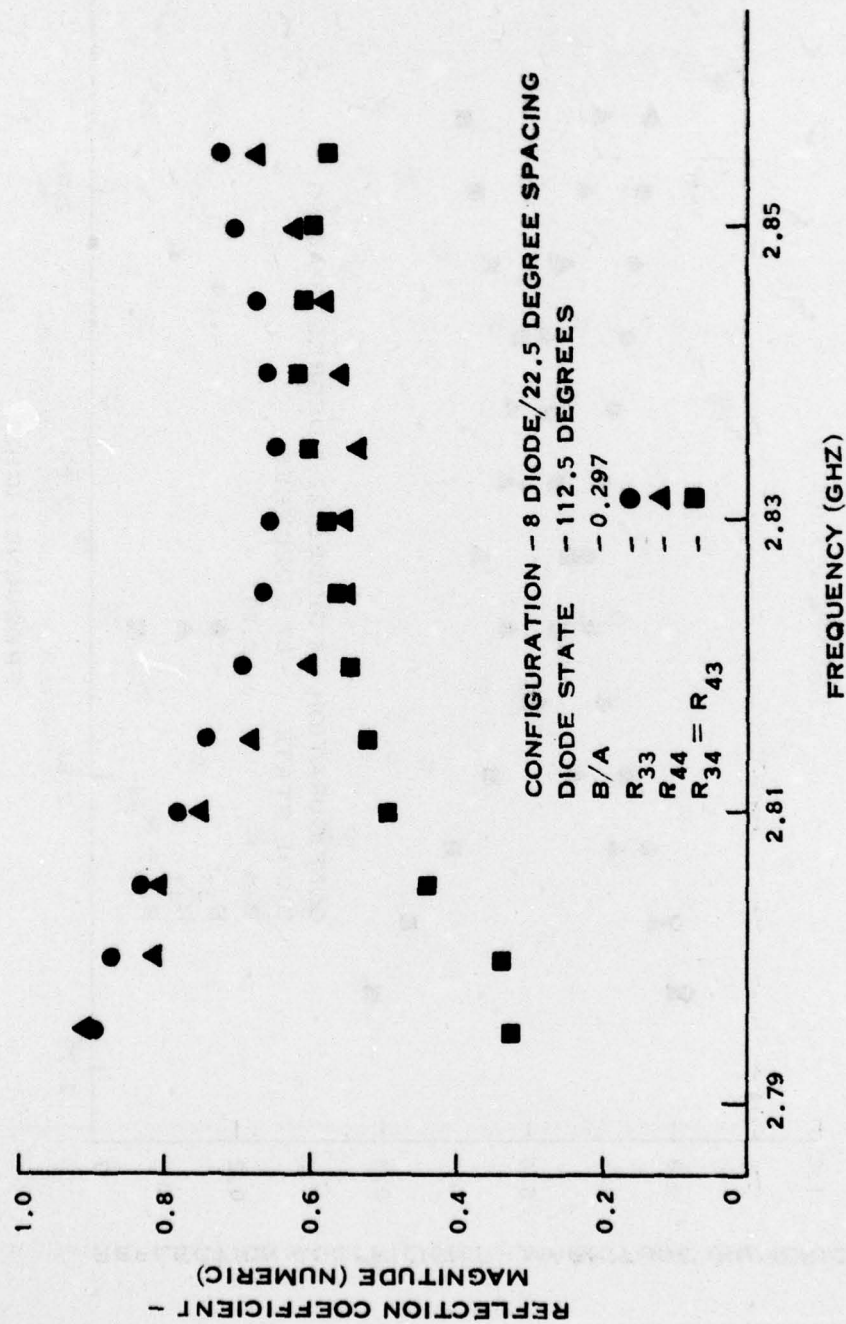
Figure 45. Reflectarray Microstrip Antenna Element Performance

208958

58

Figure 46. Reflectarray Microstrip Antenna Element Performance

59

208959
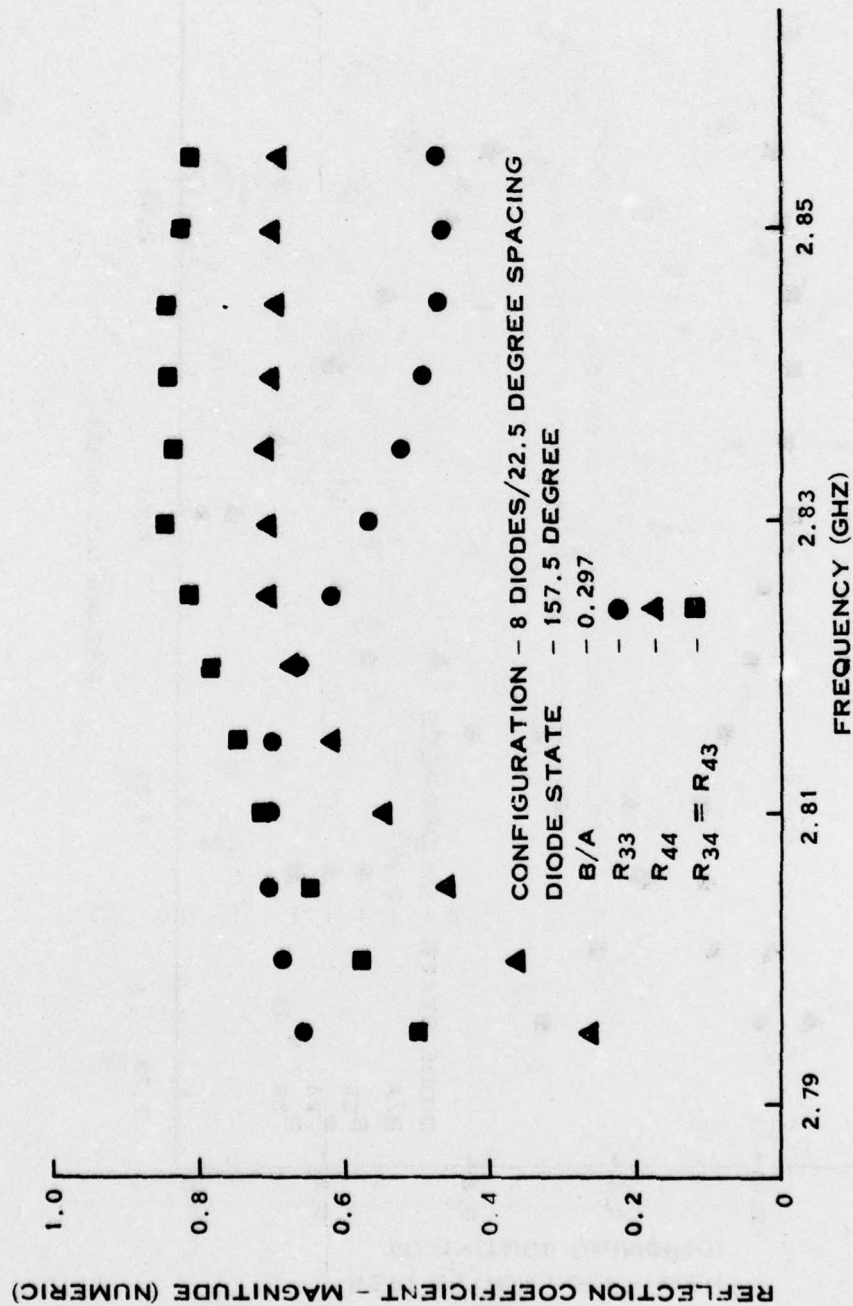
Figure 47. Reflectarray Microstrip Antenna Element Performance

208960

60
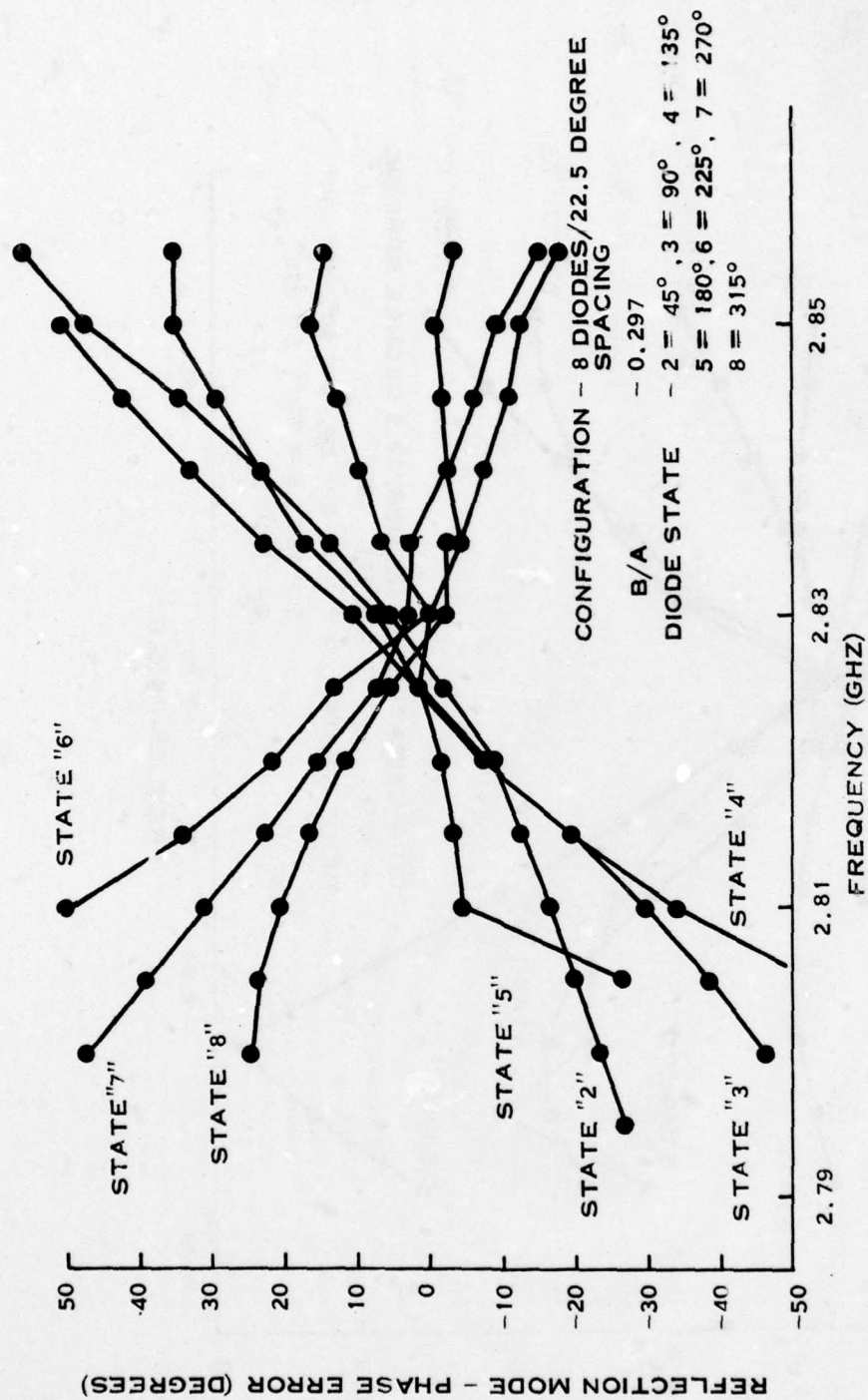
Figure 48. Reflectarray Microstrip Antenna Element Performance

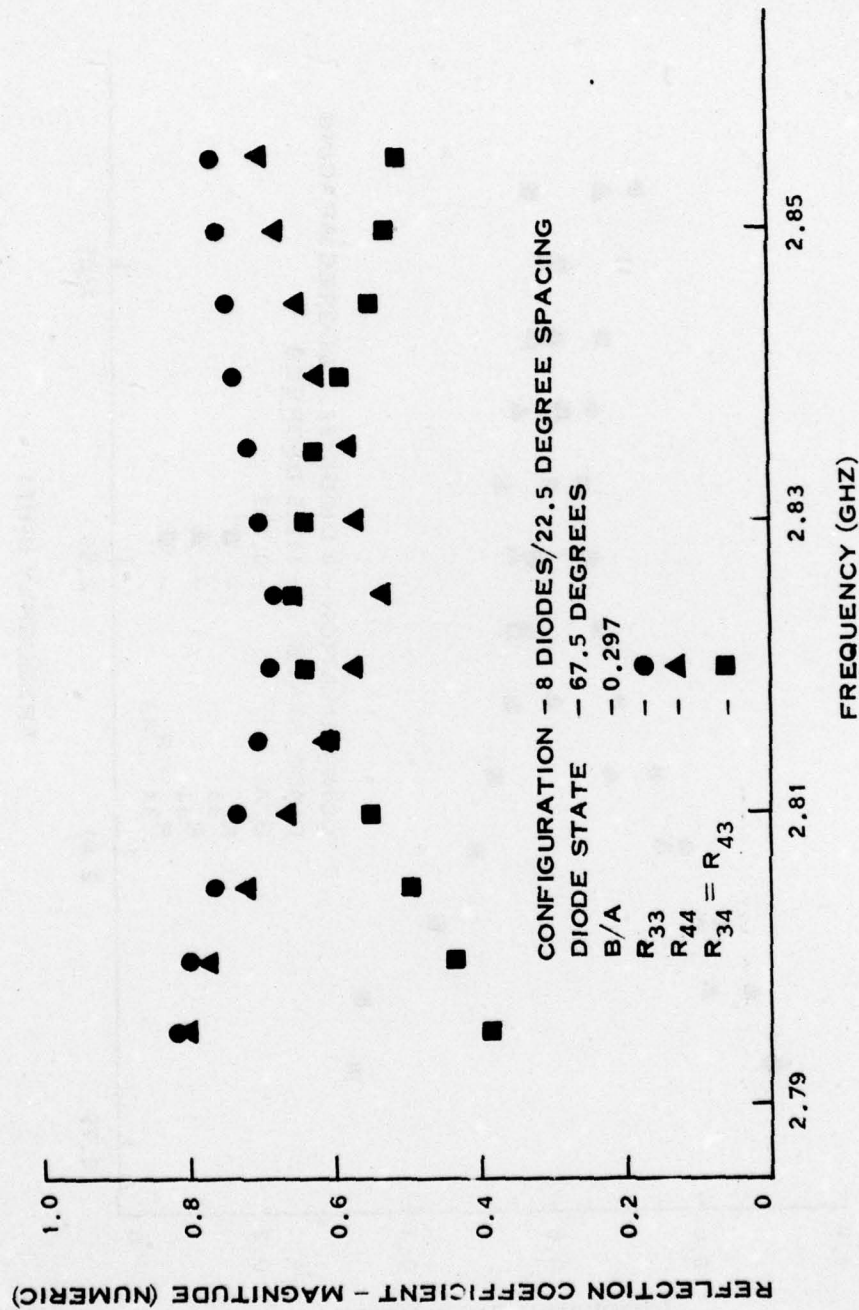208961

61
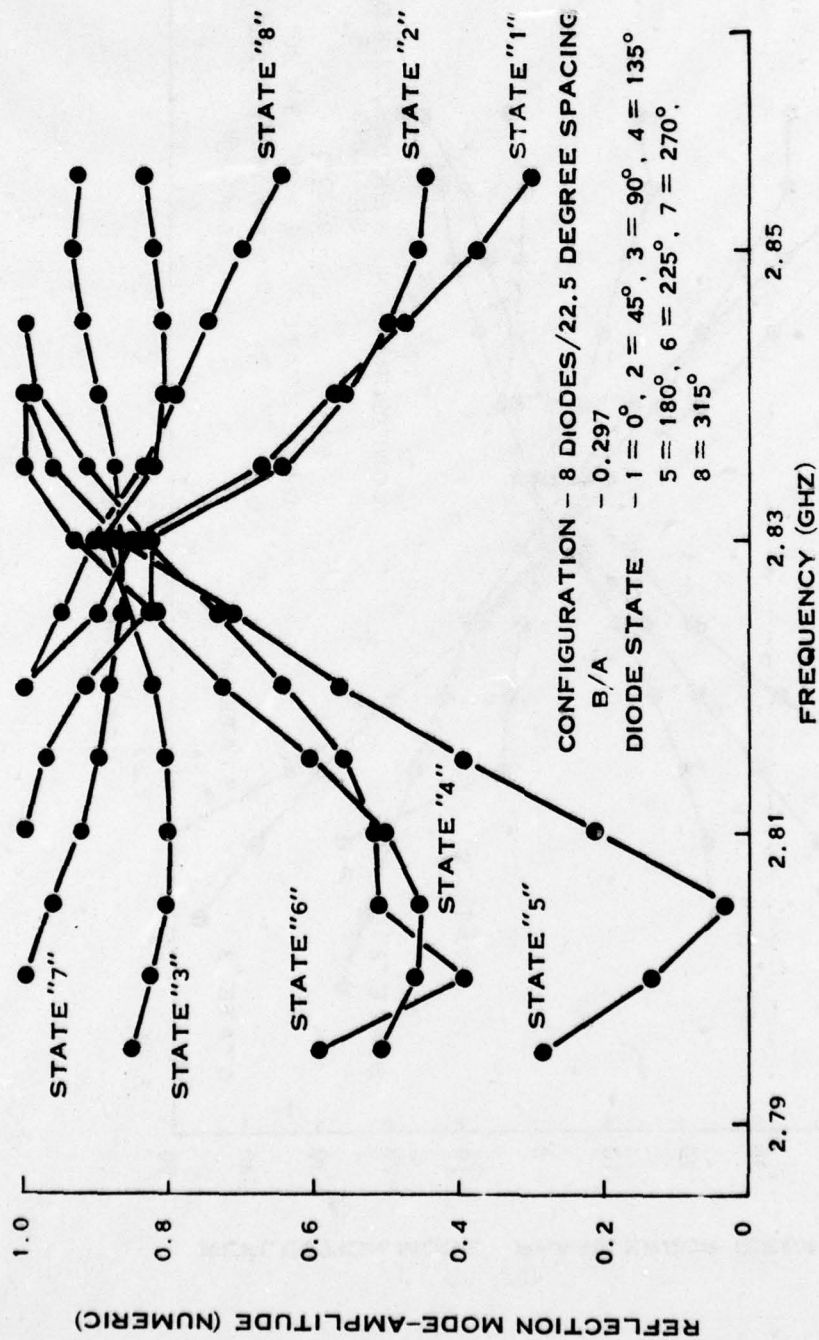
Figure 49. Reflectarray Microstrip Antenna Element Performance

CONFIGURATION – 8 DIODES/22.5 DEGREE SPACING

B/A   – 0.297

DIODE STATE – 1 = 0°, 2 = 45°, 3 = 90°, 4 = 135°
5 = 180°, 6 = 225°, 7 = 270°,
8 = 315°

FREQUENCY (GHZ)

REFLECTION MODE-AMPLITUDE (NUMERIC)

STATE "8"
STATE "2"
STATE "1"
STATE "7"
STATE "3"
STATE "6"
STATE "4"
STATE "5"

209010

62

TABLE 1. REFLECTARRAY MICROSTRIP ANTENNA PERFORMANCE
8-DIODE ELEMENT, SPACED 22.5 DEGREES
FREQUENCY = 2.83 GHz

Diode Configuration	Amplitude	Reflected E-Field Phase Absolute Degrees	Delta Degrees	Cumulative Degrees	Error Degrees
0.0	0.85	112.0	–	–	–
22.5	0.83	61.6	50.4	50.4	+5.4
45.0	0.89	11.2	50.4	100.8	+10.8
67.5	0.94	−29.9	41.1	141.9	+6.9
90.0	0.86	−68.0	38.1	180.0	–
112.5	0.82	−114.9	46.9	226.9	+1.9
135.0	0.86	−160.9	46.0	272.9	+2.9
157.5	0.90	158.9	40.2	313.1	−1.9

Figures 35 and 36 show the 4-diode element performance in phase shifter parameters. Figure 35 shows the differential phase error from the 180-degree nominal value resulting from switching the plane of the forward biased diodes 90 degrees. Curves are shown for both one and two diodes forward biased in a given plane. The most noticeable difference for these two configurations is a slight center-frequency shift. Figure 36 shows that the cross-polarization characteristic is the bandwidth limiter.

Figures 38 through 41 show the orthogonal-plane plane performance for an 8-diode loaded element. This performance is seen to be similar to the 4-diode element presented earlier. Figure 41 shows the cross-coupling terms. The third curve represents performance with all diodes reverse biased.

Figures 42 through 47 show the element performance when diodes 2, 3, 4, 6, 7 and 8 are individually forward biased while the other diodes are reverse biased. At and near band center, the performance is as predicted. Figures 38 and 39 show this element's performance by presenting the phase error from nominal and amplitude variation of the resultant E-field reflected vector. The results are similar to the 4-diode performance. That is, the bandwidth is severely limited by the cross-polarization characteristics.

Table 1 shows the element's center frequency performance. The first column, diode configuration, corresponds to individually forward biasing diodes 1 through 8 with the remaining diodes reverse biased. The amplitude column shows the magnitude of the resultant reflected E-field for each phase position. The remaining columns indicate the reflected phase performance by first showing the absolute phase; second, the incremental phase between the diode configurations; third, the cumulative incremental phase; and fourth, the phase error from nominal.

The 16-diode element performance was approximately the same as the 8-diode element. The presented data is intended to show its performance.

The diode contribution to the total element loss is approximately 0.2 to 0.4 dB. The conclusion is based on comparative measurements between elements using diodes and elements using mechanical shorting pins.

SECTION IV
ADDITIONAL CONSIDERATIONS

The element fabrication techniques used in this evaluation are applicable through X-band. Above this range, monolithic techniques must be used along with reduced dielectric thickness to minimize parasitic effects.

The integration of monolithic diode driver and logic circuitry is a straightforward process and would consist of an additional isolated metalization layer attached to the element backside.

Diodes are currently available which would allow element operation through 15 GHz.

A single-diode element (similar to that described in Proposal EG76-005 Subsection II.B.2 on page 2-23) was designed, fabricated, and tested at 15 GHz. The evaluation results were inconclusive and schedule constraints forced the effort to be terminated.

SECTION V
CONCLUSION

The primary purpose of this evaluation was to determine the feasibility and design limitations of the microstrip reflectarray antenna element. This objective was successfully reached. However, narrow operating bandwidth and relatively high loss severely limit the element's usefulness. Analysis indicates that closer array grid spacings than used in this evaluation may allow sufficient performance improvement to negate this conclusion.

Other conclusions are that a single diode or short per plane is sufficient for satisfactory element performance. The fabrication techniques developed for this evaluation represent a simple, low-parasitic, potentially low-cost approach to other similar applications.

An analysis of the scattering by an infinite array of microstrip disks has been made and is shown to be quite accurate. The analysis has been used to lend insight into the operation of a reflectarray using diodes integrated into the element to achieve phase shift for circularly polarized fields. In particular, we have shown that the loss, bandwidth, and resonant frequency are significantly affected by substrate thickness and grid spacing.

REFERENCES

1. J.Q. Howell, "Microstrip Antennas," *IEEE Trans. Antennas Propagat.* (January 1975), Vol. AP-23, pp. 90-93.

2. R.E. Munson, "Conformal Microstrip Antennas and Microstrip Phased Arrays," *IEEE Trans. Antennas Propagat.* (January 1974), Vol. AP-22, pp. 74–78.

3. H.R. Phelan, "Spiraphase—A New, Low Cost, Lightweight Phased Array," *Microwave Journal* (December 1976), Vol. 19, pp. 41–44.

4. H.R. Phelan, "L-Band Spiraphase Reflectarray," *Microwave Journal* (January 1977), Vol. 20, pp. 47-50.

5. H.R. Phelan, "Dual Polarized Spiraphase," *Microwave Journal* (March 1977), Vol. 20, pp. 37–40.

6. C.C. Chen, "Diffraction of Electromagnetic Waves by a Conducting Screen Perforated Periodically With Circular Holes," *IEEE Trans. Microwave Theory Tech.* (May 1971), Vol. MTT-19, pp. 475–481.

7. W.H. Eggimann and R.E. Collin, "Electromagnetic Diffraction by a Planar Array of Circular Disks," *IRE Trans. Microwave Theory Tech.* (November 1962), Vol. MTT-10, pp. 528–535.

8. J.P. Montgomery, "Scattering by an Infinite Periodic Array of Thin Conductors on a Dielectric Sheet," *IEEE Trans. Antennas Propagat.* (January 1975), Vol. AP-23, pp. 70-75.

9. G.V. Borgiotti, "Modal Analysis of Periodic Planar Phased Array of Apertures," *Proc. IEEE* (November 1968), Vol. 56, pp. 1881–1892.

10. N. Amitay, V. Galindo, and C.P. Wu, "Theory and Analysis of Phased Array Antennas, Wiley-Interscience (New York, 1972).

11. M.L. Kales, "Part III Elliptically Polarized Waves and Antennas," *Proc. IRE* (May 1951), Vol. 39, pp. 544-549.

12. C.C. Chen, "Transmission of Microwave Through Perforated Flat Plates of Finite Thickness," *IEEE Trans. Microwave Theory Tech.* (January 1973), Vol. MTT-21, pp. 1–6.

13. R. Mittra, T. Itoh, and T.S. Li, "Analytical and Numerical Studies of the Relative Convergence Phenomenon Arising in the Solution of an Integral Equation by the Moment Method," *IEEE Trans. Microwave Theory Tech.* (February 1972), Vol. MTT-20, pp. 96-104.

14. S.W. Lee, W.R. Jones, and J.J. Campbell, "Convergence of Numerical Solutions of Iris Type Discontinuity Problems," *IEEE Trans. Microwave Theory.* (June 1971), Vol. MTT-19, pp. 528–536.

15 P.H. Mastermann and P.J.B. Clarricoats, "Computer Field-Matching Solution of Waveguide Transverse Discontinuities," *Proc. IEEE* (January 1971), Vol. 118, pp. 51–63.

16. R. Mittra and S.W. Lee, "Analytical Techniques in the Theory of Guided Waves," MacMillan (New York, 1971).

17. C.C. Chen, "Wideband Wide-Angle Impedance Matching and Polarization Characteristics of Circular Waveguide Phased Arrays," *IEEE Trans. Antennas and Propagat.* (May 1974), Vol. AP-22, pp. 414–418.

67

18. M.V. Schneider, "Microstrip Lines for Microwave Integrated Circuits," *Bell System Tech. Journal* (May–June 1969), Vol 48, pp. 1421–1444.

19. T. Itoh and R. Mittra, "A New Method for Calculating the Capacitance of a Circular Disk for Microwave Integrated Circuits," *IEEE Trans. Microwave Theory Tech.* (June 1973), Vol. MTT-21, pp. 431–432.

20. S. Coen and G.M.L. Gladwell, "A Legendre Approximation Method for the Circular Microstrip Disc Problem," *IEEE Trans. Microwave Theory Tech.* (January 1977), Vol. MTT-25, pp. 1–6.

21. M. Sucher and M. Fox, "Handbook of Microwave Measurements," Polytechnic Press (Brooklyn, 1963), Vol. 2.

MISSION
of
Rome Air Development Center

RADC plans and conducts research, exploratory and advanced development programs in command, control, and communications (C^3) activities, and in the C^3 areas of information sciences and intelligence. The principal technical mission areas are communications, electromagnetic guidance and control, surveillance of ground and aerospace objects, intelligence data collection and handling, information system technology, ionospheric propagation, solid state sciences, microwave physics and electronic reliability, maintainability and compatibility.